

UNIVERSIDADE DE SANTIAGO DE COMPOSTELA



FACULTAD DE FÍSICA
Departamento de Física de Partículas

**Fission studies in inverse kinematics and
associated development of new time-of-flight
detectors**

Memoria presentada por:
Yassid Ayyad Limonge
como disertación para optar al
Grado de Doctor
en Ciencias Físicas
Junio 2012

UNIVERSIDADE DE SANTIAGO DE COMPOSTELA

José Benlliure Anaya, Catedrático de Física Atómica, Molecular y Nuclear de la Universidad de Santiago de Compostela y **Carlos Paradelo Dobarro**, investigador contratado de la Universidad de Santiago de Compostela,

CERTIFICAN: que la memoria titulada **Fission studies in inverse kinematics and associated development of new time-of-flight detectors** ha sido realizada por **Yassid Ayyad Limonge** en el **Departamento de Física de Partículas** de esta Universidad bajo mi dirección y constituye el trabajo de **tesis** que presenta para optar al **Doctor en Ciencias Físicas**.

Santiago de Compostela, Junio de 2012

Fdo: José Benlliure Anaya

Fdo: Carlos Paradelo Dobarro

Fdo: Yassid Ayyad Limonge

Acknowledgments

I wish to acknowledge the help provided by the people who participated in this work. First of all I would like to express my gratitude to the people who participated in the S293 and S136 experiments. Without their great experience and enthusiastic motivation this work would not have been possible.

I wish also to express my sincere gratitude to the members of the committee who evaluated and commented this thesis. Their suggestions and comments really improved the discussions and the quality of the work presented in this manuscript.

I would like to express my very great gratitude to my supervisor Prof. José Benlliure, who gave me the opportunity to work in the fascinating world of nuclear physics. Thanks to him I joined the Experimental group of Nuclei and Particles (GENP) at the University of Santiago de Compostela at 2008 where I developed this work. He always encouraged and pushed me to finish this work, and he also motivated me to dive deeper into the mysteries of the fission process. I am also indebted to my co-supervisor Dr. Carlos Paradela due to his help and support, and also due to the great time we shared during the (many) experiments we did together.

I am particularly grateful to Prof. Ignacio Durán, Prof. Dolores Cortina and Beatriz Fernández for everything I learned from them. Special thanks must be given to Manuel Caamaño due to our really fruitful and funny discussions. I really admire (and miss) his perspective about physics. I would like also to make a special mention to the help provided by Prof. Hector Álvarez-Pol, with whom I had very helpful discussions about physics and programming. Moreover, he showed me a (huge) piece of that fantastic land called Galicia. I would really like to thank you for your friendship.

And of course, I would like to thank my colleagues of the GENP group: Saúl Beceiro, Pablo Cabanelas, Martín Gascón, David González, Esther Leal,

Juan Llerena, Noelia Montes, Magdalena Mostazo, Ben Pietras (thanks for all your kind help), Diego Ramos, José Luis Rodríguez, Carme Rodríguez and Diego Tarrío. I am truly indebted to my friends Paloma Díaz, Marisol Robles (and Georgy Kornakov), Juan Ramón Pereira and Jossitt Vargas for all the great moments we shared together. I wish you all the best you in your future.

I specially thank my friend and colleague David Pérez-Loureiro for all the amazing and kind support he offered me, not only during my thesis, but still nowadays. His skills really saved me lot of times when everything seemed lost!. I wish to express my deepest gratitude to Dr. Enrique Casarejos. He took care of me when I arrived to Santiago de Compostela and I learnt a lot from him during all the time we spent together not only in Santiago but also during the endless night-shifts we shared at GSI.

I would like to express my gratitude to Dr. Alexandra Kelic-Heil and M.V. Ricciardi due to their warm welcome during my (multiple) stays at GSI (Germany) and for all the comments and remarks which really improved this work. I thank also the AsyEOS and SOFIA/ANDES experiments for the beam time provided for the characterization of RPC detectors.

Por último quisiera agradecer a mis amigos Hector Espinosa, Juanjo y María, Raúl, David F. por todo el apoyo que me habéis dado en la distancia y por los momentos inolvidables. También quiero expresar mi gratitud a Ubaldo por su apoyo y por sus discusiones sobre física. Doy infinitas gracias a mi padre y mi madre que me apoyaron de todas las maneras posibles y por supuesto aún siguen animándome. Quisiera desear mi mas profundo agradecimiento a mis hermanos Carlos y Sarah, que siempre estuvieron ahí en los momentos buenos y en los malos.

Y por último, quiero agradecer desde el fondo de mi corazón a mi mujer Iris por todo su apoyo incondicional y por todos los momentos.

Este trabajo está dedicado a la memoria de mis abuelos, Josefa y Francisco, y a la memoria de Joel Gil.

...And the raven, never flitting, still is sitting, still is sitting on the pallid bust of Pallas just above my chamber door; and his eyes have all the seeming of a demon's that is dreaming, and the lamp-light o'er him streaming throws his shadow on the floor; and my soul from out that shadow that lies floating on the floor. Shall be lifted, nevermore!

This work was partially funded by the Spanish Ministry of Education and Science under grant FPA2007-62652 and BES-2008-005553.

Contents

Introduction	1
1. Fission dynamics and experimental signatures	5
1.1. Present understanding of the fission process	5
1.1.1. Statistical approaches	6
1.1.2. Dynamical effects in fission	8
1.1.3. Transient effects induced by nuclear dissipation	9
1.1.4. Determination of the nuclear dissipation strength	10
1.2. Experimental observables probing nuclear dissipation	13
1.2.1. Fission cross sections	13
1.2.2. Direct measurements of transient effects using atomic clocks	13
1.2.3. Nuclear clocks: pre-scission neutron and γ -rays emission	14
1.2.4. Temperature at the saddle point	15
1.3. Experimental technique proposed in the present work	16
1.3.1. Spallation in inverse kinematics at high excitation en- ergies	16
1.3.2. Nuclear reaction codes	20
2. Proton-induced fission on ^{181}Ta at relativistic energies	23
2.1. Description of the experimental setup	24
2.2. Determination of the fission cross sections	27
2.2.1. Identification of the fission events	27
2.2.2. Fission yields and cross sections	30
2.2.3. Uncertainties	34
2.3. Results and discussion	36
2.4. Reaction model benchmarking	37
2.5. Conclusions	45
3. Proton- and deuteron-induced fission on ^{208}Pb at 500 A MeV	47
3.1. Description of the experimental setup	49

3.1.1.	Twin MUSIC	49
3.1.2.	Time-of-flight wall	50
3.2.	Identification of the fission fragments	51
3.2.1.	Nuclear-charge calibration	52
3.2.2.	Detection efficiency	54
3.3.	Total fission cross section	58
3.4.	Partial fission cross sections	63
3.5.	Width of the charge distribution of fission fragments	65
3.6.	Comparison with model calculations	67
3.7.	Conclusions	72
4.	New time-of-flight detectors for future fission experiments	75
4.1.	Future fission experiments at GSI	76
4.1.1.	SOFIA	76
4.1.2.	R ³ B	77
4.1.3.	FELISE	79
4.2.	Requirements of the ToF wall of the R ³ B ToF wall (iToF)	79
4.3.	ToF detectors	82
4.3.1.	Scintillation detectors	82
4.3.1.1.	Organic scintillators	83
4.3.1.2.	Performance with heavy ions	83
4.3.2.	Resistive Plate Chambers	84
4.3.2.1.	Working principles of the RPCs	85
4.3.2.2.	Avalanche RPCs	86
4.3.2.3.	Streamer RPCs	87
4.4.	Detection of relativistic heavy ions with RPCs	87
4.4.1.	Development and construction of tRPC prototypes	88
4.4.2.	Analog front-end electronics (FEE)	91
4.4.2.1.	FEE calibration	92
4.4.3.	Experimental setups	94
4.4.4.	Data acquisition systems	95
4.4.5.	Dedicated experiments	100
4.4.6.	RPC prototypes performance	102
4.4.6.1.	Time resolution	102
4.4.6.2.	Effect of the rate in the time resolution	110
4.4.6.3.	Efficiency and streamer production	113
4.4.6.4.	Effect of the gas mixture	118
4.5.	Conceptual design of the iToF tRPC modules	119
4.6.	Conclusions	121
	Conclusions	123

Resumen en castellano	127
A. Calibration of the nuclear charge distributions	139

Introduction

Soon after its discovery in 1938 by Hahn, Strassmann and Meitner [Hah39], the first description of the fission process was given by Bohr and Wheeler [Boh39] according to the transition-state theory. However, fission is an extremely complex mechanism that requires a dynamical approach to describe the evolution of the process in terms of intrinsic and collective excitation of the nuclear constituents. Transport theories [Wei80] based on Fokker-Planck have proven to be a suitable tool for the description of the collective evolution of the nuclei and they constitute the basis of many of the current theoretical models. Nevertheless, despite more than almost 75 years of intense research, fission is still far from being fully understood and the theoretical and experimental knowledge is not yet complete. The measurement with high precision and resolution of observables such as fission probabilities, masses and nuclear-charges of the final fragments, their kinetic energies, and light particles and γ -rays emitted along with this process is limited by the available technology. Results obtained with different techniques and setups currently present several inconsistencies. A substantial improvement is needed to address the existing discrepancies, validate newly developed models and extend the present limits of our understanding of the fission process.

Nuclear fission also plays a key role in the description of several nuclear properties and provides valuable information in general physics and astrophysics. Indeed, topics such as shell effects in super- and hyper-deformed nuclei [Abe94], the r-process in stellar nucleosynthesis [Rau], viscosity of nuclear matter and heat transfer between nascent fragments require a detailed knowledge of the fission process. Fission is also extremely important in the production of radioactive ion beams (RIB) to study the properties of exotic neutron-rich nuclei far from the stability [Lou11], nuclear power installations and the development of spallation neutron sources for ADS (Accelerator Driven System) technologies among others [Nif01].

In the present work we have investigated the proton-induced fission of ^{181}Ta and proton- and deuteron-induced fission of ^{208}Pb at relativistic energies. The experiments were conducted at GSI (Darmstadt), using a dedicated

setup for fission studies in inverse kinematics. This setup facilitated the counting of the projectiles and the identification of the reaction products. The unambiguous determination of both fission fragments simultaneously, with high efficiency and acceptance, allowed us to disentangle fission from other reaction channels and measure, with high precision, the total fission cross section for $^{181}\text{Ta}+\text{p}$ at 1000, 800, 500 and 300 A MeV, and, for $^{208}\text{Pb}+\text{p}$ and $^{208}\text{Pb}+\text{d}$ at 500 A MeV. Total fission cross sections are important for the characterization of spallation targets (usually constructed using materials such as Pb or Ta) used as neutron sources. We also investigated the effect of nuclear dissipation in the fission probability, especially in the $^{181}\text{Ta}+\text{p}$ reaction where a wide range in excitation energy was covered. Moreover, in the ^{208}Pb case, the charge identification of both fission fragments made it possible to reconstruct the charge of the fissioning nuclei, observable which is closely related to the excitation energy and impact parameter. The partial fission cross sections and the width of the fission fragments charge distribution as a function of the charge of the fissioning nuclei were carefully determined for the reactions $^{208}\text{Pb}+\text{p}$ and $^{208}\text{Pb}+\text{d}$. The use of two different targets allowed us to explore the effect of the excitation energy on the fissioning system. These observables were used to extract quantitative results regarding dissipative effects and dynamical times in the pre-saddle stage of the fission process. The support of state-of-the-art nuclear reaction-codes including an analytical solution of the Fokker-Plank equation (FPE) enabled a description of the dynamical evolution of the fission process.

The combination of the inverse kinematics technique and a dedicated experimental setup is a powerful tool to perform fission experiments since all fission fragments leave the target with high kinetic energies in forward (beam) direction and their properties can be determined with high accuracy. However, the isotopic identification of both fission fragments simultaneously with high precision and resolution has never been achieved and is a long-standing problem which persists in the majority of the most modern detection setups. The scientific program of the forthcoming R³B experiment at FAIR facility (Germany) will include as part of its broad scientific program, the study of fission, spallation and multi-fragmentation reactions in inverse kinematics using an improved detection scheme, similar to that of the present work, including a powerful dipole magnet. The isotopic identification of fission and spallation fragments will require state-of-the-art time-of-flight detectors with high efficiency, acceptance and time resolution below 30 ps (standard deviation). To fulfill these requirements, the possibility of building a time-of-flight wall based on RPC (Resistive Plate Chambers) detectors is under investigation. RPCs are widely-used timing detectors in high-energy physics experiments. However, the present information concerning their response when detecting

ions at relativistic energies is scarce. In this work, we have investigated the performance of RPC prototypes under relativistic heavy ion irradiation. The efficiency and time resolution of the prototypes were determined using ion beams with different atomic numbers and electron beams. The obtained results indicate the feasibility of RPC detectors for the detection of heavy ions and the construction of such a time-of-flight wall.

This manuscript is organized as follows: In chapter 1 a review on the basic ideas on the dynamics of the fission process and different experimental approaches to measure them are discussed. Chapter 2 includes the results of the experiment aiming at measuring proton-induced fission of ^{181}Ta at several relativistic energies, presenting a detailed explanation of the data reduction and the considered uncertainties. In addition, the data are compared with calculations performed with different nuclear-reaction codes and several concepts about the fission probability and dissipation are discussed. Chapter 3 includes an analog description of chapter 2 for the reactions $^{208}\text{Pb}+p$ and $^{208}\text{Pb}+d$ using an improved fission setup. A detailed discussion on transient and dissipative effects in the fission process is also included in this chapter. Finally, the objective of chapter 4 is to introduce the forthcoming experiments measuring fission via inverse kinematics and the state-of-the-art time-of-flight detectors that will be deployed in these experiments. The development of timing RPCs (tRPCs) as proposed technology for time-of-flight measurements of fission residues within the R³B framework is explained in this chapter.

Chapter 1

Fission dynamics and experimental signatures

The aim of this chapter is to compile different theoretical and experimental aspects of the dynamics to investigate the fission process. Section 1.1 is devoted to the description of the most established picture of the nuclear fission process. The concept of dissipation and its effects are introduced, as well as several theoretical approaches based on transport theories determining its magnitude. Section 1.2 provides an insight into the experimental observables used to probe dissipative effects, with a discussion concerning the validity and reliability of each signature. In section 1.3, the reaction mechanism used to induce fission in the experiment of the present work is described. The experimental technique and the measured observables are carefully explained, with an accompanying overview of state-of-the-art codes utilized in this work to infer quantitative results on dissipation.

1.1. Present understanding of the fission process

Fission is the splitting of a highly-deformed heavy nucleus into two fragments with comparable mass, as a consequence of the large-scale collective motion of nucleus constituents. The evolution of the process depends on the initial conditions of the fissioning nucleus (namely its excitation energy, fissility, angular momentum and shape) and the form of its potential energy as a function of the deformation and mass asymmetry. The process can occur spontaneously, for very heavy nuclei, or can be induced. In the latter case, part of the excitation energy transferred to the system is transformed into collective motion of most of its constituents inducing a significant defor-

mation on the nucleus. During the evolution of the fissioning system along the deformation coordinate, there exists a competition between the surface contribution to the binding energy, which opposes the deformation of the system and the decreasing Coulomb energy due to the separation of the nuclear charge, favouring the split of the system into two fragments. As a consequence, as can be seen in Fig. 1.1, the potential landscape that guides the nuclear shape evolution appears in the deformation and mass asymmetry coordinates. A threshold excitation energy is needed to promote the nuclei from the ground-state configuration above the saddle point, to the zone of the potential in which the separation of both fragments occurs. The different symmetric and asymmetric fission modes correspond to specific valleys represented in this landscape that appear due to the nuclear deformation and the mass asymmetry of the nuclei during the process.

The potential-energy landscape is often described using macroscopic-microscopic models [Möl01] or fully dynamical microscopic models based on Hartree-Fock and Hartree-Fock-Bogoliubov methods [Ber84; Gou05]. In the former, the macroscopic term corresponds to the liquid-drop model potential energy modified according to the microscopic energy term that accounts for nuclear shell-structure effects, which are responsible for the observed asymmetric mass distributions, and pairing correlations [Str67]. These effects are especially strong in low energy fission. However, the precision of these theoretical models in the prediction of some key observables such as the mass-yield curve of the fission fragments is limited due to the complexity of the many-body calculations involved. Moreover, owing to fission being a time-dependent process, static potential energy surfaces are insufficient and not all models include a dynamical treatment of the process.

Since a microscopic treatment presents severe restrictions and problems due to the complexity of the calculations, the dynamics of the fission process can be described with the help of macroscopic variables which fluctuate in a stochastic way. Using transport theories, one can describe this evolution with collective (deformation) and intrinsic (excitation energy) degrees of freedom which correspond to coordinate motion and individual state of the nucleons, respectively. Thus, fission dynamics is governed by the evolution of collective parameters.

1.1.1. Statistical approaches

According to Bohr's compound-nucleus hypothesis [Boh36], an excited compound nucleus created in the interaction between a projectile and a target nucleus reaches a statistical equilibrium with a well defined excitation energy and angular momentum and all the possible states are populated with the

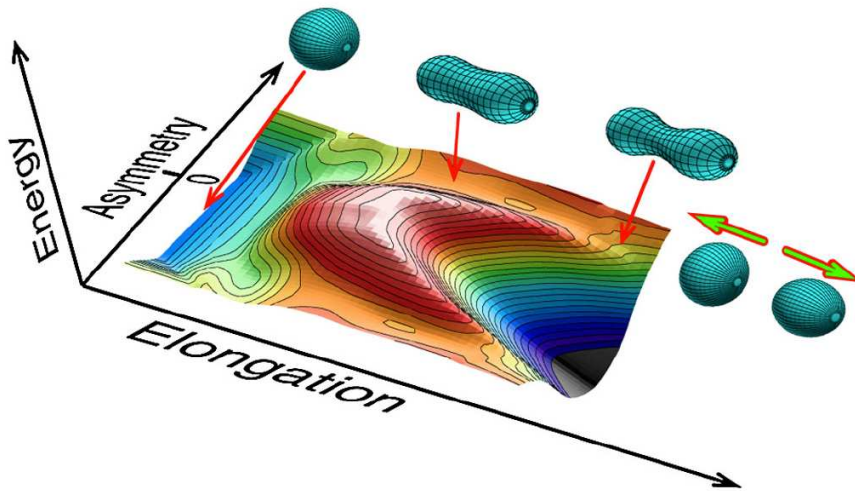


Figure 1.1: Representation of the potential landscape of ^{180}Hg as a function of the nuclear deformation or elongation and the asymmetry. Figure taken from [And10].

same probability. The de-excitation mode of the compound nucleus depends on the decay width of each channel and the process follows a sequence of evaporation steps until the ground-state is reached. Therefore, it can be explained as a competition between the different de-excitation channels.

Using Bohr's hypothesis and the principle of detailed balance, the evaporation of light particles was described by Weisskopf and Ewing using a statistical formalism [Wei37; Wei40], later improved by Hauser and Feshbach introducing a quantal treatment of the angular momentum [Hau52]. In this formulation the evaporation process is governed by the level densities of the initial and final nuclei involved in the decay and the transmission coefficient for the emitted particle. At high excitation energies, the particle decay width can be approximated as:

$$\Gamma_{\nu}(E_i) = \frac{1}{2\pi\rho(E_i)} \frac{4m_{\nu}R^2}{\hbar^2} T_f^2 \rho(E_i - S_{\nu} - B_{\nu}) \quad (1.1)$$

where E_i is the excitation energy of the nucleus and R its radius, S_{ν} is the separation energy of the particle, B_{ν} is the Coulomb barrier for particle evaporation, $\rho(E_i - S_{\nu} - B_{\nu})$ and T_f are the level density of the residual nucleus and its temperature, respectively.

Usually, the fission decay width is described by the transition-state model of Bohr-Wheeler. In contrast to the particle evaporation where the decay rate depends on the level density of the final state, in this case the decay rate mainly depends on the density of states above the fission barrier

(saddle point) and the phase space the fission fragments occupy along the deformation axis. The expression for the fission decay width was given by Moretto [Mor75] based on the Bohr-Wheeler model:

$$\Gamma_f^{BW} = \frac{1}{2\pi\rho(E_i)} T_{sad} \rho(E_i - B_f) \quad (1.2)$$

with T_{sad} being the temperature at the saddle point. The fission barriers B_f are calculated from Sierk's finite-range liquid-drop model [Sie86] including the corrections from ground-state shell structure [Möl86]. The Bohr-Wheeler model does not consider the mass asymmetry degree of freedom. To overcome this problem, Moretto proposed an expression for the fission barrier $B_f = B_0 + \alpha q$, including the mass asymmetry coordinate q . This formalism was improved by Benlliure *et al.* [Ben98] by giving a more realistic description of the mass-asymmetry dependence of the energy potential at the saddle point, based on a semi-empirical description of the shell effects described by Brosa [Bro90].

1.1.2. Dynamical effects in fission

In order to describe the evolution of the fissioning system and its collective degrees of freedom, Kramers [Kra40], in 1940, proposed an interpretation of fission as a diffusion process within the framework of transport theories. In this description, in analogy to the Brownian motion, the collective degrees of freedom move in an external field, the strength of the field affected by the heat bath of the individual nuclear constituents, which corresponds to the internal degrees of freedom of the system. Thus, the equation of motion is given by the specific Langevin equation combining a friction term and a stochastic diffusion term due to the interaction of the collective degrees of freedom with the heat bath, and a drift term due to the potential (external field force) according to the equation:

$$\frac{dv}{dt} = -\beta v - \frac{1}{m} \frac{\partial}{\partial x} U(x) + \frac{F'(t)}{m} \quad (1.3)$$

where $U(x)$ is the nuclear deformation potential and $F'(t)$ is the stochastic force. The term βv is the friction force derived from the interaction of the system with the surrounding medium, v being the velocity of the system, in this case the deformation velocity, and β a parameter that depends on the properties of that medium. Owing to the random nature of $F'(t)$, the Langevin equation should be solved for event-by-event single trajectories to describe the motion of the nucleus. However, instead of that, the Fokker-Planck equation (FPE) [Ris89] describing the evolution of the system

according to the time-dependent probability distributions $W(x, v, t)$ of finding the system with a given velocity v and time t , is used. Assuming the time the collective degrees of freedom need to make a significant change is much larger than the relaxation time of the internal degrees of freedom [Wei80], the FPE expression is:

$$\frac{dW}{dt} = \left[-\frac{\partial}{\partial x}v + \frac{\partial}{\partial v} \left(\beta v - \frac{1}{m} \frac{\partial}{\partial x} U(x) \right) + \frac{\beta kT}{m} \frac{\partial^2}{\partial v^2} \right] W \quad (1.4)$$

where k is Boltzmann's constant and T is the temperature of the heat bath. The stationary solution of the FPE found by Kramers results in a reduction of the fission width predicted by Bohr-Wheeler's model induced by the nuclear dissipation:

$$\Gamma_f^K = \Gamma_f^{BW} \left(\left[1 + \left(\frac{\beta}{2\omega_0} \right)^2 \right]^{1/2} - \frac{\beta}{2\omega_0} \right) \quad (1.5)$$

where Γ_f^{BW} is the fission decay width predicted by Bohr-Wheeler's statistical model and ω_0 is the frequency of the harmonic-oscillator of the inverted potential at the saddle point. β is the dissipation coefficient which represents the excitation energy rate exchange between collective degrees of freedom and the heat bath (intrinsic degrees of freedom).

Kramers' picture was not fully accepted until the Bohr-Wheeler model failed in reproducing the pre-scission multiplicity of neutrons and γ -rays emitted during the fission process at high excitation energies [Gav81; Gav82], which consequently led to an overestimation of the fission rate. This fact revealed that a dynamical description of the process was needed in order to explain the hindrance of the fission channel owing to the competition with particle evaporation.

1.1.3. Transient effects induced by nuclear dissipation

Motivated by the results obtained by Gavron *et al.*, Grangé and collaborators [Gra83] investigated the effects of nuclear dissipation on the temporal evolution of the fissioning system. Grangé *et al.* found a time-dependent fission decay width, $\Gamma(t)$ by numerically solving the FPE equation and considering an initial system at ground-deformation with high intrinsic excitation energy and low angular momentum. According to this solution, during the early stage of the process, $\Gamma(t)$ is completely suppressed and needs a transient time, τ_f (of the order of 10^{-21} s), to reach the 90% of its asymptotic value (see upper panel of Fig. 1.2), which corresponds to Kramers fission decay width [Bha86]. The strong competition with the evaporation of neutrons

during this time can cool down the compound nucleus preventing it from undergoing fission. Usually, the equilibration time of the internal degrees of freedom is short compared to the characteristic time of the diffusion process itself and the decay times. Transient effects only manifest at high excitation energies where the average decay time of the system is comparable to the relaxation time of its degrees of freedom. In addition, if the nucleus starts its deformation at the bottom of the potential well, transient effects are expected to be more evident and its evolution is completely governed by the diffusion. At lower excitation energies the evolution of the fissioning system is ruled by the phase space and Bohr-Wheeler's transition-state model is applied.

Transient time emerges from the idea underlying the complex description of the energy transfer rate between collective and intrinsic degrees of freedom. The former need a finite time to explore the deformation space which depends on how fast the excitation energy is transformed into deformation. While the potential forces drive the system to the ground state, diffusion enlarges the width of the probability distribution, populating the available phase space, and allowing the system to establish a quasistationary flux above the barrier. The relation between the reduced dissipation coefficient and the transient time is obtained from the numerical solutions of the FPE [Bha86]:

$$\begin{aligned}\tau_f &= \frac{1}{\beta} \ln \left(\frac{10B_f}{T} \right) & \text{for } \beta < 2\omega_{gs} \\ \tau_f &= \frac{\beta}{2\omega_{gs}^2} \ln \left(\frac{10B_f}{T} \right) & \text{for } \beta > 2\omega_{gs}\end{aligned}\tag{1.6}$$

where ω_{gs} is the oscillation frequency of the potential at the ground state, B_f the fission barrier height and T is the temperature. The value of β defines the dissipation regime (see lower panel of Fig. 1.2). For $\beta < 2\omega_{gs}$, the system follows an underdamped regime characterized by the fast energy transfer of intrinsic excitation energy into the collective degree of freedom as β increases. If $\beta > 2\omega_{gs}$, τ_f increases with increasing β . In this case, the energy is injected very fast, but the time the system needs to reach the stationary regime is increased owing to the damping of the motion of the collective degree of freedom in the deformation space. There exist a critical damping in which the compromise between the energy transfer rate and collective motion hindering leads to the shortest transient time.

1.1.4. Determination of the nuclear dissipation strength

The determination of the magnitude of the dissipation coefficient β is still under debate and several approaches provide different quantitative results. In this section, a brief summary of theories explaining nuclear dissipation are

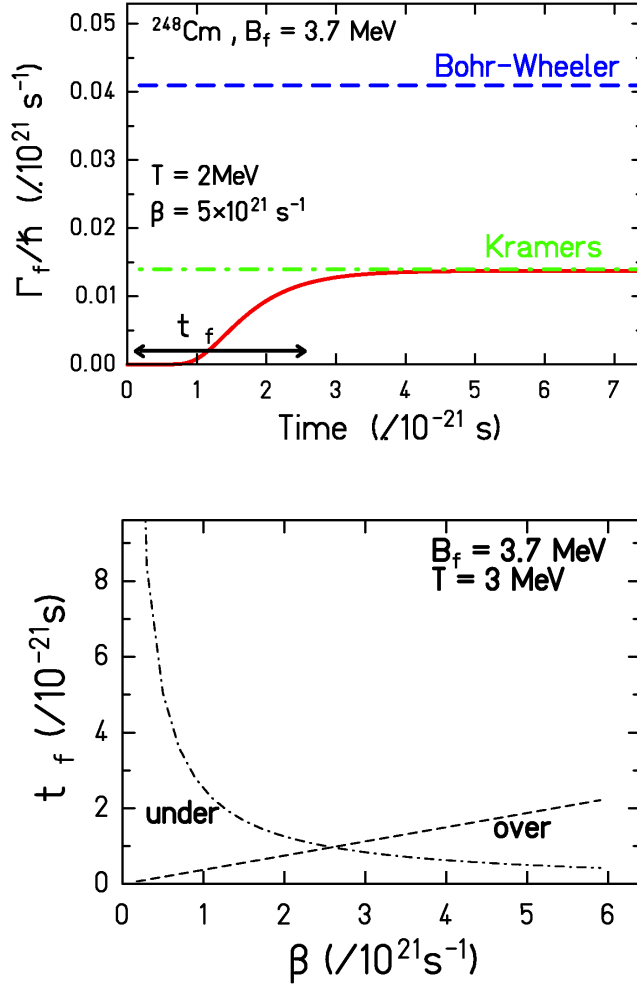


Figure 1.2: Upper panel: Fission rate as a function of time. The dashed and the dashed-dotted line corresponds to Bohr-Wheeler (Γ_f^{BW}) and Kramers fission rate (Γ_f^K), respectively. The solid line represents the numerical solution of the FPE, $\Gamma(t)$ [Bha86] for a system with $A=248$, $\beta = 5 \times 10^{21} \text{s}^{-1}$ and $T=2 \text{ MeV}$. Lower panel: Transient time as a function of the dissipation coefficient for a system with $A=248$ and $T=3 \text{ MeV}$. Figures taken from [Jur02].

presented. Hofmann and collaborators [Hof97; Hof01] extended Kramers' picture into quantal formalism. In this theory, the equation of motion of the collective degree of freedom is expressed using transport coefficients which depend on the deformation and the temperature:

$$M \frac{d^2x}{dt} + \eta \frac{dx}{dt} + Cx(t) \quad (1.7)$$

where M is the inertia coefficient, η is the friction coefficient and C is the stiffness coefficient. An expression for the dissipation coefficient $\beta = \eta/M$, which depends strongly on the temperature (T), is proposed in this work:

$$\beta(T) \approx \frac{0.6T^2}{1 + \frac{T^2}{40}} \quad (1.8)$$

Fröbich and co-workers [Frö98] introduced a deformation-dependent dissipation coefficient using a combination of a dynamical and a statistical code (combined dynamical statistical model (CDSM)). At the beginning of the process, for compact nuclear shapes, the magnitude of the dissipation coefficient is rather small ($\beta \approx 2 \times 10^{21} \text{ s}^{-1}$). During the deformation of the nuclei, the value of β increases up to $30 \times 10^{21} \text{ s}^{-1}$ at the scission point. Using this parametrization, this model explains the fission probabilities and pre-saddle neutron multiplicities, especially for systems with long saddle-to-scission path.

The nuclear dissipation can be described according to the phenomenological theory of the wall and window formula for one-body dissipation [Blo78]. Based on the Gross model [Gro75], the wall formula describes the dissipation as the interaction of the nuclear constituents with the nuclear potential, which is represented as a moving wall compressing the nucleons. The energy dissipated by this moving wall is proportional to the velocity of nucleons in a Fermi gas and their mass density. An improved wall friction formulation [Cha01] provides a result that reveal a strong suppression of the friction strength, when compared to of $\beta \approx 2 \times 10^{21} \text{ s}^{-1}$. On the other hand, the window formula is applied to the scission of the fissioning system, where two sub-systems are communicated through a small window. In this formula, the energy dissipation is proportional to the velocity of the particles moving in each sub-system and to the area of the window.

The dissipative diabatic dynamics (DDD) approach was introduced by Nörenberg [Nör83] to describe heavy-ion collisions at a few A MeV. According to this picture, based on the adiabatic theorem [Bor28], the single-particle (nucleons) motion is coherently coupled to a time-dependent mean field. The diabatic excitation of single-particles and holes produces repulsive forces on the collective motion which kinetic energy is stored as a conservative potential. An incoherent coupling introduced by residual two-body collisions (interaction between nucleons) leads to equilibrium by destroying the diabatic part of the potential and dissipating the stored energy. Therefore, the

dissipation term of the equation of motion of the collective degree of freedom includes a time retardation. In this theory, the dissipation coefficient is proportional to $1/T^2$ (T being the temperature) and an estimated value of $\beta \approx 40 \times 10^{21} \text{ s}^{-1}$ at $T = 2.5 \text{ MeV}$ [Hil92]

1.2. Experimental observables probing nuclear dissipation

In this section, the standard observables of the fission process sensitive to dissipation and transient effects and the experimental approaches are discussed. Most representative experiments exploited observables such as fission probabilities or pre-scission particle multiplicities to extract information about the time evolution of the fission process, whereas others used sophisticated clocks to indirectly measure the times involved in it [Jac09].

1.2.1. Fission cross sections

Fission probability is one of the proposed observables to investigate the effects of the nuclear dissipation during the pre-saddle phase of the fission process. If transient effects are present, the fission channel is completely suppressed at the early stage of the process. During that delay, the fissioning nucleus cools down by particle evaporation, hence, the temperature of the system at the saddle point is reduced. This effect is more prominent at higher excitation energies where the evaporation time is shorter. Moreover, as explained before, dissipation also reduces the asymptotic value of the fission width predicted by the transition-state model. These two effects significantly reduce the fission cross section. The evaporation residue cross sections were also investigated to extract more information about pre-saddle dynamics [Frö98]. However, the interpretation of dissipative effects using the fission and evaporation residues cross sections needs the support of model calculations which depend on parameters such as the initial conditions (excitation energy, angular momentum and deformation), the ratio of level density parameters at ground (for neutron evaporation) and at saddle (for fission) a_f/a_n and the magnitude of the fission barriers.

1.2.2. Direct measurements of transient effects using atomic clocks

The measurement of the times involved in the fission process is a difficult and challenging task with limited sensitivity. These kind of measurements

give access to information on the time evolution of the system up to scission. Two methods have been used: the filling of the K-shell hole created via the collision of a nuclei with the inner electrons of an atom of a given medium [Mol93] and the crystal blocking technique [Gol99].

In the former, vacancies created in the inner shells, are occupied by electrons of the outer shell emitting characteristic X-rays whose decay line-width determine the lifetime of that vacancy. The characteristic X-ray allows to distinguish whether it was emitted due to the interaction with fission fragments or before scission of the nuclei. Assuming a known probability for a vacancy creation and an exponential decay law for the processes, the scission time is determined with an X-ray emitted by a pre-scission vacancy in coincidence with the fission fragments. Owing to the precision of the method, only upper limits for the scission time of the order of 10^{-18} s have been obtained [Wil04].

In the blocking technique, fragments moving inside a single crystal along the direction of a specific axis are deflected owing to electromagnetic interactions with the atoms. Thus, the angular distribution of the emerging particles presents a characteristic dip due to the blocking or deflection. In the fission case, an excited nucleus is created inside the crystal with a recoil velocity. The depth and the shape of the dip in the angular distribution depends on where the fission fragments are emitted inside the crystal. Therefore, the shape of the dip is directly connected to the total scission time. The sensitivity of this method, which is around 10^{-19} s, is limited by the thermal vibrations of the crystal atoms.

1.2.3. Nuclear clocks: pre-scission neutron and γ -rays emission

The number of emitted light-particles before fission, namely neutrons, and γ -ray yields valuable information about fission time scales prior to scission. The number of emitted particles is linked to the time the nucleus needs to reach the scission point, thus, for longer times, the multiplicities are higher. In the case of neutron emission (neutron clock [Hil92; Hin92]), the lifetime of the pre-scission stage (τ_f) is basically the sum of the mean evaporation time of each emitted particle (τ_n), which can be calculated according to the statistical model. At high excitation energies, where the ratio of the level densities of the initial and final state is not completely known, the pre-scission time is approximated using the excitation energy at the scission point (E_{sci}^*) which is reconstructed using the post-scission neutron multiplicities: $\tau_f \approx \tau_n E_{sci}^*$. Pre- and post-scission neutrons are discriminated by their kinematics.

The γ -rays emitted during the fission process come from the de-excitation

of the Giant Dipole Resonance mode (GDR) of the nuclei. The authors of [Pau94] stressed the influence of the dissipation in the increase of the GDR γ -rays emission with respect to the predictions of the statistical model. In this case, the γ -rays emission comes either from pre-scission stage or from the fission fragments. However, contrary to the neutron clock case, pre- and post-scission GDR γ -rays contributions need the support of model calculations to be disentangled.

To extract qualitative results about early transient time using nuclear clocks, pre- and post-saddle contributions have to be disentangled. However, it is impossible to experimentally access the saddle point information and model calculations are needed [Sax94].

1.2.4. Temperature at the saddle point

The temperature at the saddle point (T_{sad}) is a key parameter for understanding the fission dynamics. As mentioned before, the modification of the excitation energy (temperature) at the saddle point during the transient time alters the fission probability. Since one cannot directly measure T_{sad} , other observables, such as the width of the mass or charge distributions of the fission fragments are needed.

According to the statistical model, the width of the mass A of the fission fragment distribution (σ_A) is related to the temperature at the saddle point [Fon69; Arm70] following the equation:

$$\sigma_A^2 = A_{fiss}^2 T_{sad} / (16d^2V/d\eta^2) \tag{1.9}$$

where $(16d^2V/d\eta^2)$ is the mass asymmetry potential stiffness, $\eta = (4/A_{fiss}/(M - A_{fiss}/2))$ is the mass asymmetry, and A_{fiss} and M are the mass of the fissioning nuclei and the mass of the fragments, respectively. Due to the high probability of neutron evaporation compared to proton emission, the width of the charge distribution of the fission fragments, σ_z , is more suitable to investigate dissipative and transient effects. The connection between mass and charge distributions is:

$$\sigma_z^2 \approx (Z_{fiss}/A_{fiss})^2 \sigma_A^2 = Z_{fiss}^2 T_{sad} / (16d^2V/d\eta^2) \tag{1.10}$$

Z_{fiss} being the charge of the fissioning nuclei. An empirical parametrization of the mass asymmetry potential stiffness at the saddle point as a function of the fissility of the nuclei, found by Rusanov and collaborators [Rus97], is used to infer the temperature at the saddle point. A deeper insight into transient effects extrapolated from T_{sad} needs the backup of model calculations, as we will see in the next section.

1.3. Experimental technique proposed in the present work

1.3.1. Spallation in inverse kinematics at high excitation energies

There exist several mechanisms to excite nuclei and induce fission. The excitation energy, angular momentum and shape of the fissioning nuclei is determined by the reaction mechanism. According to the work of Grangé and collaborators [Gra83], the ideal conditions to observe transient effects require high excitation energy, low angular momentum and the nucleus in the ground state deformation.

Fissioning systems can be created via nucleus-nucleus collisions at low energies (less than 100 A MeV). It is the so called fusion-fission reaction which is the most commonly used mechanism to probe dissipation effects. The compound nuclei or fissioning nuclei formed in these kinds of reactions have a well-defined mass and charge and a broad angular momentum distribution. The excitation energies acquired by the fissioning nuclei are less than 120 MeV. This fact complicates the manifestation of pre-saddle dynamical times since a threshold excitation energy is needed [Tho93; Mor95]. The majority of the fusion-induced fission experiments used atomic and nuclear clocks for measuring pre-scission neutrons, light-charged particles and GDR γ -ray multiplicities. Owing to the high angular momentum induced in the fissioning system, this may have a considerable deformation, the transient delay being therefore reduced. If the fission is induced by nucleon-transfer reaction the situation is similar to that of the fusion-fission reaction with even lesser excitation energies (below 80 MeV). In this case the number of highly fissile systems is even more limited.

Fragmentation induced by heavy ions and spallation reactions at relativistic energies also fulfill the ideal conditions established by Grangé for the manifestation of transient regimes [Ye12]. These reactions can be understood as two stages with different time scales [Ser47]. Initially, due to the fast interaction between the projectile and the target, a highly excited compound nucleus is well formed with a narrow shape distribution and with collective degrees in the ground state deformation. During the second stage, the thermalization and de-excitation of the system occurs through evaporation of neutrons, light-charged particles, intermediate mass fragments (IMF), γ -ray and eventually fission.

Benlliure and collaborators [Ben02] investigated dissipative effects in spallation reactions using inverse kinematics. In this experiment, performed at

the FRS (FRagment Separator [Gei92]) at GSI (Darmstadt - Germany), highly excited nuclei with an average angular momentum of $10\hbar$ [Jon97], were created in collisions of a ^{197}Au beam impinging on a proton target at relativistic energies. The use of the inverse kinematics technique allowed the measurement of the reaction products, which were emitted in forward direction with large velocities, with high precision and efficiency. Focusing on the fission channel, the reaction was reconstructed with the velocity, charge and mass of one fragment. The key observables sensitive to dissipation used in this work were the total fission cross section and the width of the charge distribution of the fission fragment (σ_Z). In Fig. 1.3, the isobaric distribution obtained in this work is compared with different calculations performed with codes describing the fission process [Gai91; Kel09]. As can be seen, calculations according to the Bohr-Wheeler model clearly overestimate the fission cross sections while calculations considering a dissipation strength of $\beta = 2 \times 10^{21} \text{ s}^{-1}$ (solid line) are in good agreement. A transient time of $(3 \pm 1) \times 10^{-21}$ was inferred from the calculations considering a step-function function to evaluate the time-dependent fission decay width $\Gamma(t)$. Moreover, from Eq. 3.6, the temperature at the saddle T_{sad} point was inferred and a mean excitation energy above the barrier of around 110 ± 20 MeV was obtained considering $E_{saddle}^* = a_f T_{saddle}^2$, where a_f is the level-density parameter at saddle deformation calculated according Ignatyuk *et al.* [Ign75]. Taking into account a contribution of the fission barrier B_f of around 18 MeV, the excitation energy of the nucleus at the saddle amounted to 128 MeV.

Based on these ideas, a new experimental approach was proposed by Jurado *et al.* [Jur04] to deduce a value of the transient time using peripheral relativistic heavy-ion collisions. An innovative experimental setup to investigate fission in inverse kinematics [Sch00] with high acceptance and efficiency, was used to make a complete reconstruction of the reaction (see Fig. 1.4 for a schematic view). Previous experiments performed at the FRS in inverse kinematics, measured the mass and charge of fission residues with high precision, in addition to the fission cross sections [Fer05; Ben02; Ber03; Enq01; Per07]. However, the transmission of the fission fragments was limited by the acceptance of the spectrometer, and only one fission fragment was measured. In this new experimental setup, owing to the kinematics of the reaction, both fission fragments were emitted in forward direction with large kinetic energies and detected in-flight simultaneously. The charge of both fission fragments allowed to reconstruct the charge of the fissioning nuclei, $Z_1 + Z_2$, and select each fission event according to the excitation energy induced in the collision and its impact parameter. For low impact parameters, more nucleons are removed along the abrasion stage due to the centrality of the collision thus the value of $Z_1 + Z_2$ decreases. As a consequence, high excitation energies

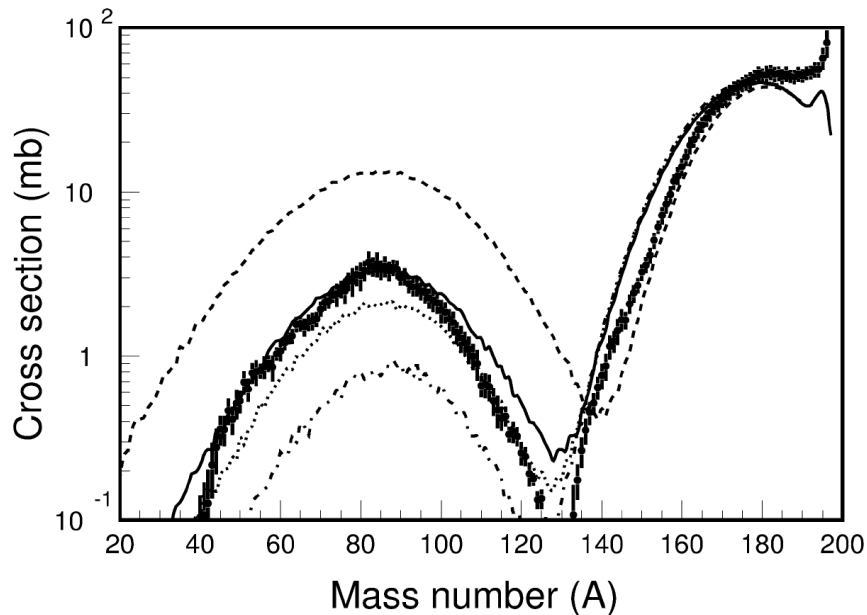


Figure 1.3: Experimental isobaric distribution of the residues produced in the reaction $^{197}\text{Au}+p$ at 800 A MeV (dots) compared to calculations performed with reaction codes. The dashed line corresponds to calculations performed according to the Bohr-Wheeler picture. The solid line refers to dynamical calculations performed considering a value of $\beta = 2 \times 10^{21}\text{ s}^{-1}$. The dotted and the dashed-dotted line correspond to a value of the nuclear dissipation of $\beta = 3 \times 10^{21}\text{ s}^{-1}$ and $\beta = 5 \times 10^{21}\text{ s}^{-1}$, respectively. Figure taken from [Ben02].

are induced in the fissioning system.

Two new signatures sensitive to transient effects were extracted. The partial fission cross sections for each fissioning system according to the charge of the fissioning nucleus $Z_1 + Z_2$ revealed a suppression of the fission channel for systems with high excitation energy (i.e. low value of $Z_1 + Z_2$) because evaporation decay times are faster than the transient time during which the fission decay is completely inhibited. This signature proved to be more sensitive to these effects than the total fission cross section since the events were selected according to its excitation energy. Another signature exploited in Jurado's work was that of the width of the charge distribution of the fission fragments σ_Z as a function of $Z_1 + Z_2$. This allowed to deduce the temperature at the saddle point which increases with the decrease of $Z_1 + Z_2$. At higher excitation energies, transient and dissipative effects lower the temperature at the saddle point because the nucleus has more time to evaporate particles, and therefore, the width of the charge distribution is reduced also.

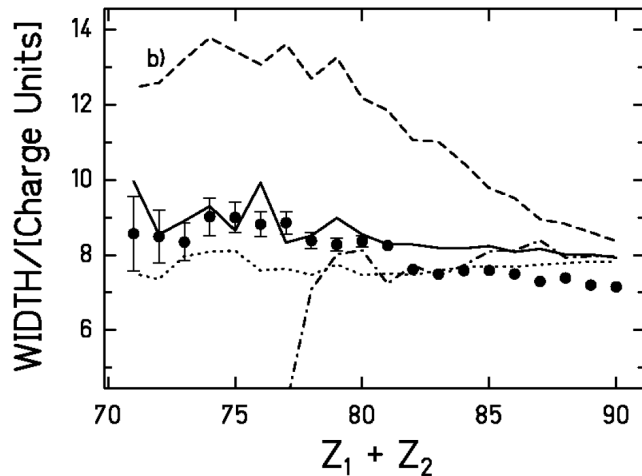


Figure 1.4: Experimental widths of the charge distribution as a function of the charge of the fissioning system $Z_1 + Z_2$ (dots). The results are compared with model calculations according to the Bohr-Wheeler model (dashed line), and dynamical calculations considering an analytical solution of the FPE and a value of the dissipation coefficient of $\beta = 2 \times 10^{21} \text{ s}^{-1}$ (solid line), $\beta = 0.5 \times 10^{21} \text{ s}^{-1}$ (dotted line) and $\beta = 5 \times 10^{21} \text{ s}^{-1}$ (dashed-dotted line). The figure was extracted from [Jur02; Jur04]

The results were compared with a modified version of the ABRABLA code including an analytical solution of the FPE [Jur03; Jur05b] in order to extract conclusions on transient effects (see Fig. 1.4). In this case, a transient time of $(1.7 \pm 0.4) \times 10^{-21}$ was calculated. These signatures were also exploited in several systems, with different fissilities, created by fragmentation of spherical radioactive heavy nuclei using a similar setup [Sch10].

In the present work, two different experimental schemes based on the experimental setup utilized in [Sch00] were used to measure the proton-induced fission of ^{181}Ta and proton- and deuteron-induced fission of ^{208}Pb . For $^{181}\text{Ta}+p$ the total fission cross section was measured at different relativistic energies (0.3, 0.5, 0.8 and 1 A GeV). This allowed to investigate the fission probability over a wide range of excitation energy. In the ^{208}Pb case, fission was induced at 500 A MeV using two different targets (proton and deuteron) to explore two different ranges of excitation energy. In addition, the nuclear charge of both fission fragments were unambiguously determined, and following the work of Jurado *et al.*, the charge of the fissioning nuclei ($Z_1 + Z_2$) is reconstructed to discriminate each event according to its excitation energy. Therefore, the excitation energy is modified either by changing the target or

varying the $Z_1 + Z_2$ range. Since ^{208}Pb is a doubly magic and spherical nuclei, its fission induced by spallation at relativistic energies represents a favorable scenario to investigate the dissipative and pre-saddle transient effects using the above-mentioned signatures. Specific details about the detectors used in the setup will be explained in the corresponding chapters.

1.3.2. Nuclear reaction codes

In this section, a short description of the codes we have used in this work to model the fission process at intermediate and high energies is presented. The use of these reactions codes to extrapolate quantitative results about pre-saddle transient times are compulsory since the direct experimental measurement is technologically impossible. Following the idea of a two-stage process, calculations are made using a code describing the first fast interaction stage coupled to a de-excitation code.

For the first stage two different INC (Intranuclear-cascade) models are used: INCL (Liège) [Cug97; Bou02] and ISABEL [Yar79]. The former is applied to reactions between light projectiles with an energy lower than few hundreds GeV (pions, light nuclei and nucleons) and heavy targets. The interaction between the projectile and the target nucleus is described as a succession of binary collisions and decays among the particles which form the system along a complete cascade event. The target is represented as a potential well whose radius depends on the momentum of the nucleons moving inside it following a degenerate Fermi gas distribution. The nucleons follow a Saxon-Woods density distribution with a maximum distance R_{max} :

$$\rho(r) = \frac{\rho_0}{1 + \exp\left(\frac{r-R_0}{a}\right)} \quad (1.11)$$

where R_0 and a are the parameters deduced from electron scattering experiments. The particles are moving along straight trajectories inside the potential well until two of them reach the minimum distance of approach, defined as the radius of a sphere with area equal to the particle-particle cross section, or they reach the border of the potential well. The evolution of every particle in the system is followed as the time evolves and the output corresponds to the velocity of all the emitted particles and the characteristics of the remnant nucleus. The inelastic collisions, as well as pion production and absorption are treated through Δ -resonances:



The NN elastic collision uses free cross sections above 400 MeV. In addition, the Pauli blocking allows only interactions where the phase-space has

not been already occupied by a particle. At the beginning of the process when the incident particle penetrates the target, the excitation energy increases rapidly achieving a maximum and then it decreases by pre-equilibrium evaporation. The cascade stops a certain time after the excitation energy loss rate is much slower and before a de-excited prefragment is produced with an excitation energy and angular momentum corresponding to the kinetic energies sum of the ejected particles in the Fermi gas and the angular momentum sum that each ejected particle carries, respectively. Then the evaporation process starts. It is also worth pointing out that INCL parameters are not adjusted, but taken from optical model phenomenology.

The ISABEL model [Yar79] describes reactions between nucleon-nucleus and nucleus-nucleus collisions within relativistic classical mechanics frame. The description of the nucleus and the projectile is similar to that of INCL, thus, in this time-like intra-nuclear cascade model, both the projectile and target particles are inside a potential well and are treated as a continuous medium or Fermi sea which is perturbed by the collisions induced by the cascade particles (particles lifted out of the Fermi sea). Interactions between the particles of the Fermi sea of the projectile and the target, or between the cascade particles and the Fermi sea of either the projectile or the target are considered. The interaction between particles inside the same Fermi sea are not considered. The nuclear density distributions are described by a step-like function divided in eight regions of constant density fitted to a Yukawa potential. The code is evaluated each step or time interval given by the velocity of the particles, and mean-free path defined by the NN free cross sections ($\lambda = \frac{1}{\sigma\rho}$). If an interaction takes place, the treatment is conceptually the same described for INCL for NN elastic collisions and for Δ and π production in inelastic scattering. The cascade particles are followed until they leave the target or projectile volume, or their energy falls below a certain cutoff energy, which corresponds to the Coulomb barrier plus two times the binding energy.

The description of the de-excitation stage is made either according to Weisskopf-Ewing or Hauser-Feshbach [Hau52] formalisms. In the ABLA code [Kel09] the de-excitation by particle emission is described according to Weisskopf-Ewing formalism as a competition between fission and other decay channels (namely emission of neutrons, γ -rays, light charged particles and intermediate mass fragments (IMF)) as described in section 1.1.1. In such code, a critical parameter is the ratio of level-density parameter at ground (neutron evaporation) and at saddle (fission), a_f/a_n , which is calculated in ABLA according to the expression found in [Ign75]:

$$a = a_v + a_s A^{2/3} B_s \quad (1.13)$$

where a_s and a_v are the surface and volume coefficients of the single-particle level densities, respectively. B_s is the ratio between the surface of the deformed nucleus and a spherical nucleus. Fission barriers dependent on the angular momentum are calculated from the finite-range liquid-drop model of Sierk [Sie86]. In ABLA, the particle-decay widths do not depend on time. However, the fission decay channel is described according to a dynamical description of the fission process based on an analytical solution of the FPE [Jur05b; Jur05a], $\Gamma(t)$, which is time-dependent due to dissipation effects. Each de-excitation step, every decay width is calculated again for the corresponding nucleus and the functional form of $\Gamma(t)$ is given by the FPE solution or by an adequate analytical solution. There exists three different approximations describing $\Gamma(t)$. A step-function following the expression:

$$\Gamma_f(t) = \begin{cases} 0, & \text{if } n t < \tau_{trans} \\ \Gamma_f^K, & \text{if } n t \geq \tau_{trans} \end{cases} \quad (1.14)$$

where Γ_f^K is the Kramers fission-decay width. Also an exponential in-growth function:

$$\Gamma_f(t) = \Gamma_f^K \{1 - \exp(-t/\tau)\} \quad (1.15)$$

with $\tau = \tau_{trans}/2.3$. Another description of $\Gamma_f(t)$ based on a realistic approximation of the FPE solution is also included in ABLA. A detailed discussion of this approach can be found in [Jur03]. Calculations with ABLA included in this work were made with a version of the code including the latter description of the fission widths.

GEMINI++ is another relevant statistical code also used to describe the de-excitation process [Cha88]. This model was originally developed to address complex-fragment emission in heavy-ion fusion experiments. Here, the decay of the compound nucleus is described as a succession of binary decays until the competition with γ -ray emission makes the particle emission improbable because of the energy of the system. The evaporation of light-charged particles is described by the Hauser-Feshbach formalism which includes a more specific angular momentum treatment, while the production of IMF and heavier fragments via binary decay is ruled by Moretto [Mor75] formalism. The main difference with ABLA lies in the treatment of the fission decay. In this case, the fission width is predicted using Bohr-Wheeler formalism and Sierk's model for the fission barriers, and therefore, GEMINI++ does not include any description about dissipative and transient effects the basic parameters requiring adjustment to reproduce the experimental data. In particular, the GEMINI++ version used in this work the ratio of level-density parameter, a_f/a_n , is adjusted to 1.036 [Man10].

Chapter 2

Proton-induced fission on ^{181}Ta at relativistic energies

Spallation reactions induced by relativistic protons on ^{181}Ta lead to excited target remnants with large fission barriers (20-25 MeV) covering a broad range in excitation energy. The investigation of the fission process under these extreme conditions is expected to provide relevant information on the dynamics of fission at high excitation energies. Additionally, tantalum and tungsten alloys are well suited for the construction of spallation neutron sources because of their properties under extreme irradiation conditions: relatively large neutron production, corrosion resistance, and a high melting point. Spallation targets are of interest in different domains. One of the technologies which relies on spallation reactions is that of accelerator-driven systems, ADS [Nif01], which are currently under study as an option for nuclear waste incineration. Recently the construction of the ESS (European Spallation Source) [Cla03] facility has been approved and different research communities are awaiting its opening to undertake a wide range of experimental programs in material science, biology and other scientific disciplines. Tantalum targets are also used for the production of exotic nuclei at ISOL-type [ISO] facilities and neutrinos [Bur96].

Fission may have a significant effect on the performance of a spallation target. Therefore, a good knowledge of the interaction of protons (commonly used as spallation-source drivers) with these materials is mandatory for their characterization. Reactions leading to fission are of interest because they contribute to the production of hazardous remnants, in particular gaseous ones, such as the isotopes of Kr and Xe. The composition of that radioactive inventory, its evolution, the influence of these changes to the target performance itself and its structural damages can be estimated with state-of-the-art models. However, only through an evaluation of numerical calculations

with accurate data is it possible to validate these models and improve their reliability for use in technical applications.

Unfortunately, presently available data related to total fission cross sections of ^{181}Ta above 700 MeV proton-beam energy are scarce and show clear discrepancies at 1000 MeV [Yur05; Boc78]. The situation does not improve at lower energies, where the available data are more abundant, but there are also significantly inconsistent results [Bar62; Kon66; Shi73; Mau65], in particular between 300 and 500 MeV. Most of these experiments were performed using passive track detectors and only few of them are based on coincident measurements of both fission fragments [Ste67]. Under such conditions it seems difficult to unambiguously identify a fission channel with a few mb cross section as is expected in this case. All previous measurements of fission reactions induced by protons on ^{181}Ta were performed using the direct kinematics technique. Therefore, the reaction products have a very low kinetic energy, preventing their escape from the target. To overcome this difficulty the detection scheme presented in section 1.3 was utilized.

This chapter is dedicated to the analysis of the fission cross section of $^{181}\text{Ta}+p$ at 300, 500, 800 and 1000 A MeV. The use of different beam energies will allow us to explore the effect of the nuclear dissipation at different excitation energies. The experimental setup and the main aspects of the detectors utilized in this work are presented. We implemented a method to recognize fission events and calculate the fission yields normalized to the number of projectiles. Then, fission cross sections and their uncertainties were determined with high accuracy. In the last part of this chapter, we compared the results with previous measurements and systematics found in the literature and with calculations based on state-of-the-art models describing the fission process.

2.1. Description of the experimental setup

In the present experiment, the ^{181}Ta nuclei were accelerated using the installation of GSI, the UNILAC linear accelerator and the SIS-18 synchrotron, up to 300, 500, 800 and 1000 A MeV with an intensity of the order of 10^4 ions/s and a spill duration of 7 s. The beams were guided to a dedicated experimental setup (shown in Fig. 2.1) where they impinged onto a liquid hydrogen target surrounded by two Multi-Sampling Ionization Chambers (MUSIC), used to identify the reactions of the beam particles with any layer of matter placed in the setup. A Multi-wire chamber (MW) and a veto scintillator were used to collimate the beam and determine its position. Due to the kinematics of the reaction, we were able to detect efficiently both

fission fragments which were emitted in forward direction with large kinetic energies. A double paddle scintillator was used for this purpose. This capability enabled the use of relatively thick targets, increasing the statistics. The beam dose was measured using a scintillator placed upstream of the first MUSIC.

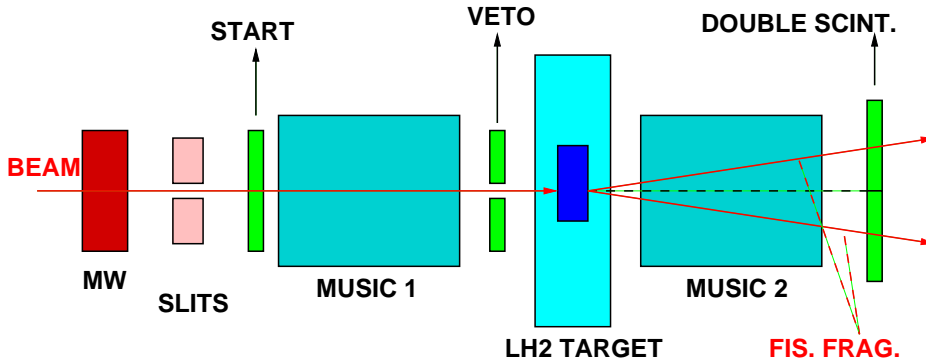


Figure 2.1: Schematic representation of the experimental setup used in the present experiment.

Multi-wire chambers A Multi-wire chamber (MW) [Ste91] and thick iron slits were used to collimate the ^{181}Ta beam at the target. The MW consists of five parallel wire planes with different voltages. The anode plane is made of tungsten wires of $20\ \mu\text{m}$ with 2 mm pitch while the cathode electrodes have $50\ \mu\text{m}$ wires separated by 1 mm. The latter define the X and Y orthogonal directions. The spacing between anode and cathode planes is 5 mm. The chamber operates with a gas mixture (Ar and CO_2) at atmospheric pressure.

Scintillators A first scintillator detector (start) placed upstream of the target, determined the beam flux. This detector consists of a BC420 3 mm thick plastic scintillator coupled to two R2083 Hamamatsu photomultiplier allowing a double lecture from both sides (left and right). With this double lecture we determined the position of the beam.

A veto scintillator with a 15 mm diameter hole placed just before the target allowed the rejection of beam-halo particles and misaligned beam trajectories. The two fission fragments were detected independently, but in temporal coincidence, by a double paddle made of two BC420 scintillators (up and down read out) placed downstream of the target (300 mm x 70 mm and 3 mm thickness each paddle separated by a 1 mm gap).

The signals coming from the photomultipliers were discriminated using constant fraction discriminators (CFD) and then sent to a time-to-amplitude

converter (TAC) whose signal was digitized by a CAEN V785 analog-to-digital converter (ADC). The signals were also sent to a CAEN V792 charge-to-digital converter (QDC) to register the charge of the pulses.

Target The proton target consisted of a liquid hydrogen cell of about 1 cm thick and 3 cm diameter (85 mg/cm^2), isolated by two windows consisting of two titanium foils of $15 \mu\text{m}$ of thickness and five layers of Al-coated mylar strips of $30 \mu\text{m}$ of thickness. This container was used to protect the beam line vacuum in case of rupture of the hydrogen cell. A cryostat for liquefying the hydrogen was used to establish a pressure and temperature of around 1 atm and 20 K, respectively.

Multi-sampling ionization chambers The target was surrounded by two Multi-Sampling Ionization Chambers (MUSIC80) having an active area of 200 mm x 80 mm and 460 mm of active length filled with CF_4 (see Fig. 2.7). The windows of the chambers were made of float glass and aluminum-coated mylar ($210 \mu\text{m}$). A voltage of 8000 V was applied between the eight anodes and the cathode, aligned in parallel, to create an uniform electric field. A Frisch-grid at 0 V was placed near the anodes to restrict the position dependence of the induced signals. The electrons, released in the ionization of the medium by an ion crossing the chamber, were forced to drift to the anodes. The induced signals were registered by charge-sensitive amplifiers that converted the charge into amplitude signals. These amplitude signals were digitized by a CAEN V785 ADC. Therefore, both chambers measured the energy loss of the tantalum beam particles and that of the products of the reaction, respectively. These ionization chambers, having almost 100 % efficiency for the detection of relativistic heavy nuclei and high rate capability (up to 200 kHz), were used to identify reactions of ^{181}Ta produced in the hydrogen target and in any other layer of matter present in the beam line.

Data acquisition The pulses were digitized using standard VME electronic modules. The control of the VME bus was done with the CES RIO3 processor. The data read out of the VME modules was managed by the multi-branch system (MBS) developed at GSI [MBS]. Data were read out and sent to an event builder for each accepted trigger. According to the setup geometry, two different triggers were used for data acquisition: The “beam” trigger was provided by the start plastic scintillator placed upstream of the target in anti-coincidence with the signal of the veto scintillator. The “reaction” trigger was produced by the coincidence between the “beam” trigger and the time-coincident signals on both paddles of the double scintillator

placed downstream the target. These two triggers provided the measurement of the beam flux together with the reaction events. The average rates for the “beam” and “reaction” triggers were around 10^4 and 700 triggers/s, respectively. We used CAEN V820a scalers to count the number of “beam” and “reaction” triggers. The “beam” trigger was downscaled by a factor of 2^8 or 2^{10} (depending on the beam energy) to reduce the data acquisition dead time.

2.2. Determination of the fission cross sections

2.2.1. Identification of the fission events

The identification of the fission events was based on the amplitude of the signals recorded by the two MUSIC chambers surrounding the target and the amplitude of the signals provided by the two paddles of the double-plastic scintillator located downstream of the target. With this information, we were able to isolate fission events from other reaction channels occurring in the hydrogen target.

In Fig. 2.2 a scatter plot of the energy losses of ions traversing the two MUSICs, before and after the target, is depicted using the “reaction” trigger. The events lying in the diagonal of this plot correspond to ions which kept their atomic number when passing through the target. These nuclei, lighter than the primary beam, have been produced in nuclear reactions induced by ^{181}Ta projectiles in the layers of matter situated upstream of the hydrogen target. The dominant ^{181}Ta spot of non-interacting beam particles is clearly visible at the top, near channel 3800 on the vertical axis. The vertical group below the beam spot corresponds to residual fragments produced in the interaction of ^{181}Ta with hydrogen. In this group, events inducing high and small energy loss signals, correspond to residual heavy nuclei and emitted light nuclei from evaporation processes.

Since the energy loss of nuclei is proportional to their atomic number squared (Z^2), fission fragments are expected to produce energy loss signals corresponding to about half of the value obtained for the primary beam ($\Delta E_{f.f.} \propto Z_1^2 + Z_2^2 = Z_{beam}^2/2$). Therefore, fission products should be located around channel 1800 on the MUSIC 2 energy loss axis. To count for the fission events, n_{fiss} , a condition in the scatter plot shown in Fig. 2.2 was applied selecting the region where the fission products are expected. Focusing on the selected region, indicated by the rectangular area in Fig. 2.2, the fission events were identified combining the amplitude (energy loss) of the signals

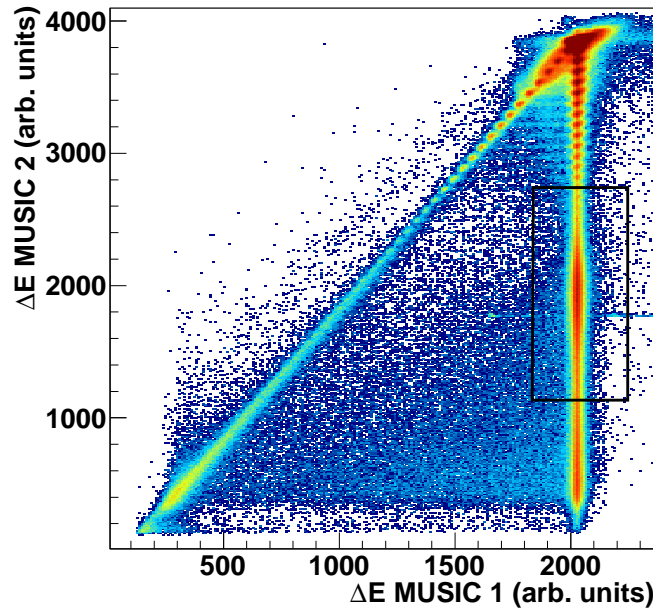


Figure 2.2: Scatter plot of the amplitudes of the signals registered with the two MUSIC detectors. Nuclei lighter than ^{181}Ta produced in reactions before MUSIC 1 appear in the diagonal region. In the vertical line the ^{181}Ta spot corresponding to non-interacting beam particles is represented, and below the events corresponding to reactions in the target. The box encloses the fission region and the color code represents counts on the logarithmic scale.

recorded by the two paddles of the double plastic scintillator.

In Fig. 2.3 the amplitudes of the signals registered by both plastic scintillators in temporal coincidence (at 1 A GeV and 300 A MeV in the left and right panels, respectively), using the “reaction” trigger, are represented in a scatter plot. Due to the charge splitting of the fission process, fission events are expected to populate the diagonal band in this figure, and are separated from other much more abundant reaction channels. This fission region only represents a small part of the plot statistics since the fission probability is rather small. For this reason, fission events could only be properly identified by a detection setup enabling the identification of different reaction channels.

In order to provide an accurate measurement of the fission cross section, we evaluated the background which remains in the fission region due to simultaneous break-up and evaporation processes. To evaluate this background we used Fig. 2.4, where the energy loss provided by the two paddles of the

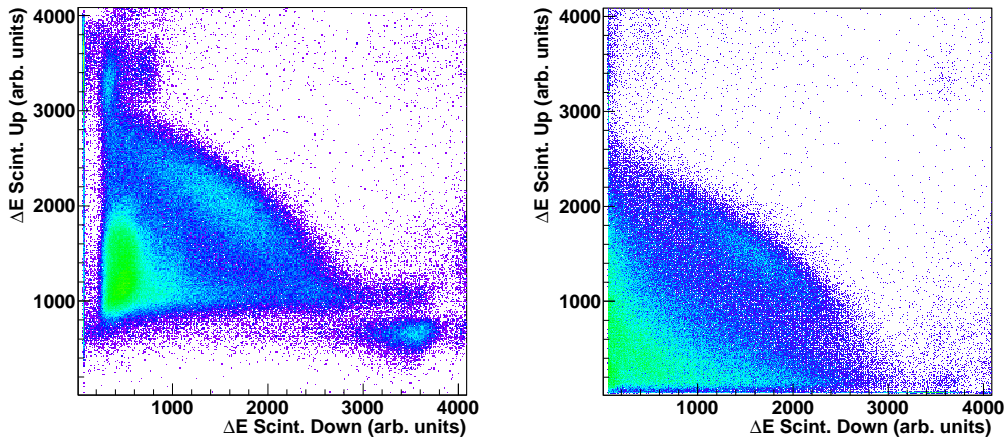


Figure 2.3: Scatter plot of the energy loss signals provided by the two paddles of the double plastic scintillator placed downstream the target with the reaction trigger (Left panel 1 A GeV Full target - Right panel 300 A MeV Full target). Both plots are normalized to the same number of counts to highlight the influence of different reaction channels. The color code represents counts on the logarithmic scale.

double plastic scintillator at 1000 A MeV is represented by selecting only events compatible with a fission signal in the MUSIC detectors (rectangular area in Fig. 2.2).

In this figure, intermediate mass fragments (IMFs) produced in simultaneous break-up reactions may populate the fission region (dotted contour in Fig. 2.4). The evaluation of this break-up background was performed by dividing the fission region into slices as shown by the thin rectangles in Fig. 2.4. Each slice was then projected along its longitudinal dimension (insets in Fig. 2.4), which clearly enhanced the profile of the contributions coming from background (left peak) and fission (right peak). Gaussian fits to each of the two contributions defined the correction for the break-up background suppression. On the other hand, evaporation residues could also populate the edges of the fission region along an axis $\Delta E_1 + \Delta E_2$ (dashed line in Fig. 2.4) defined by the sum of the signals of the two scintillators. To overcome this problem, the region profile (dotted contour in Fig. 2.4) was projected onto this $\Delta E_1 + \Delta E_2$ axis to evaluate this contribution by means of gaussian fits as shown in Fig. 2.5.

The number of measured fission events n_{fiss} corresponds then to the number of events in the fission region corrected by the overlapped simultaneous break-up and evaporation background contributions.

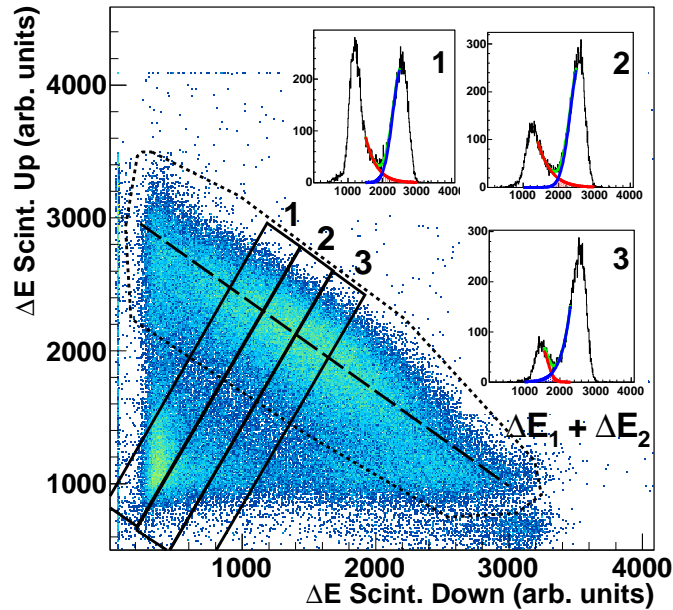


Figure 2.4: Same as the upper panel in Fig. 2.3 but conditioned by the fission selection from Fig 2.2. The different contours and insets illustrate the background suppression method used to identify fission events as explained in the text.

2.2.2. Fission yields and cross sections

Fission yields (Y_{fiss}) were obtained from fission event measurements corrected by the background (n_{fiss}) and additional effects such as the secondary reactions of the fragments in the target (f_d) and the geometrical acceptance of the experimental setup (f_{geo}), according to the following equation:

$$Y_{fiss} = n_{fiss} \cdot f_d \cdot f_{geo} \quad (2.1)$$

Secondary reactions of the fission fragments in the target were evaluated using the Karol's microscopic model [Kar75]. The number of reactions ε_d amounted to less than 2.5 % for full target and less than 0.5 % for empty target measurements at 1000 A MeV. The correction factor was determined according to $f_d = 1/(1 - \varepsilon_d)$.

Geometrical constraints were also considered to evaluate the efficiency of the detection setup. Fission products emitted close to the double paddle scintillator gap had a probability of passing through it or through the same

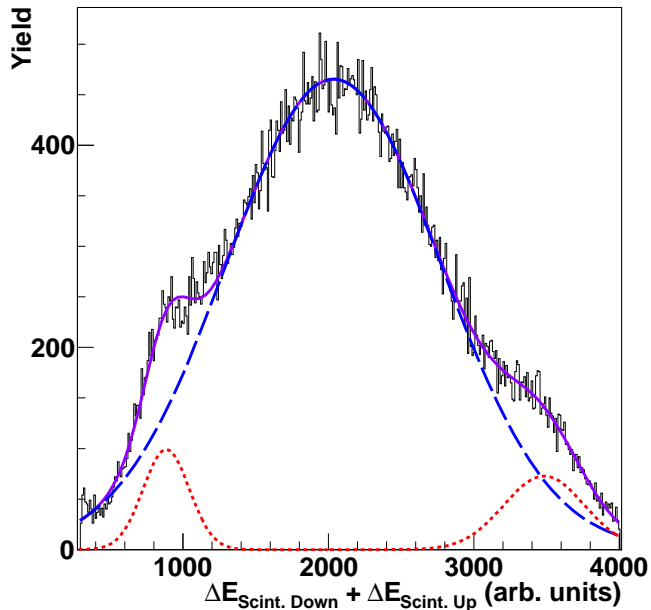


Figure 2.5: Projection of the fission region defined in Fig. 2.4 on the $\Delta E_1 + \Delta E_2$ axis represented in the same figure. The contribution of evaporation residues was evaluated by means of a gaussian fit (dotted line) and subtracted from the total contribution (dashed line).

paddle. A Monte Carlo calculation of the post-scission kinetic energy of the fission fragments [Wil76] was performed to evaluate the ratio of fission product losses due to the geometry of the setup. The kinetic energies of the fission fragments can be calculated with the following equation:

$$TKE = \frac{Z_1 Z_2 e^2}{D} \quad (2.2)$$

where Z_1 and Z_2 are the nuclear-charges of the fission fragments. D is the distance between their respective centers at the scission point which is calculated using the following expression:

$$D = r_0 A_1^{1/3} \left(1 + \frac{2}{3} \beta_1 \right) + r_0 A_2^{1/3} \left(1 + \frac{2}{3} \beta_2 \right) + d \quad (2.3)$$

A_1 and A_2 being the masses of the fission fragments, β_1 and β_2 the deformation coefficients, $r_0 = 1.16 \text{ fm}$ and $d = 2 \text{ fm}$. Using equations 2.2 and 2.3 we calculated the velocity of the fragments in the center of mass frame and

then a Lorentz boost in the beam direction was applied to transform the velocities into the laboratory frame. Taking into account the gaussian profile of the beam as measured with the Multi-wire chamber detector ($\sigma \approx 0.4$ cm), the velocities of the fragments, the alignment and distance from the centre of the hydrogen target to the double plastic scintillator, we calculated the perpendicular dimensions of the fission fragments distribution in the double plastic scintillator detection plane (see Fig. 2.6). The acceptance of these scintillators (300 mm x 140 mm and 1 mm gap) allowed us to evaluate the losses, by counting the number of fragments lost in the gap, and estimate the geometrical efficiency of the double paddle scintillator ε_{geo} having a value larger than 90 % at 1000 A MeV and decreasing with the beam energy.. Thus, the resulting yield was corrected by a geometrical factor ($f_{geo} = 1/\varepsilon_{geo}$).

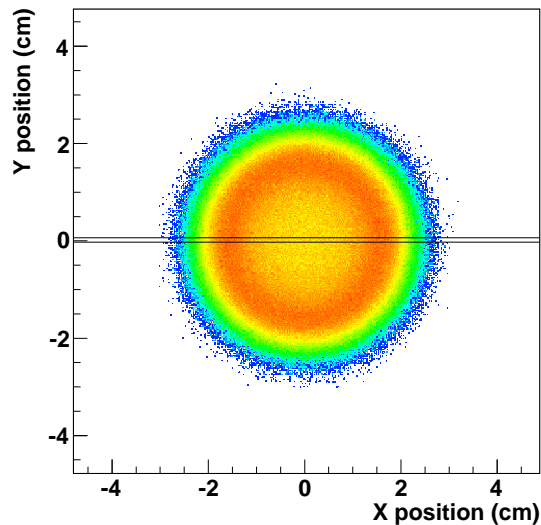


Figure 2.6: Simulated fission fragments spatial distribution in the double plastic scintillator plane for the reaction $^{181}\text{Ta}+p$ at 1 A GeV. The area between both solid lines represents the size of the gap.

To determine the number of projectiles (n_b), we used the first MUSIC to identify tantalum among other nuclei that have been created in other layers of matter placed in the beam line before the target, as shown in Fig. 2.7. The sum of the $Z = 73$ ions was identified according to this procedure using the “beam” and the “reaction” trigger corrected by the downscaling factor provided the total number of projectiles.

Due to the relatively large thickness of the target, a fraction of projectiles

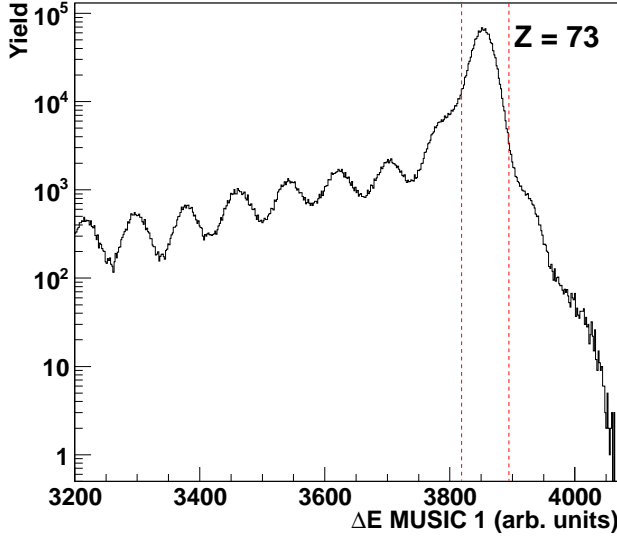


Figure 2.7: Energy loss signals provided by the MUSIC 1. The region between the dotted red lines corresponds to ^{181}Ta .

ε_a was attenuated ($< 5\%$ for full target and $< 1\%$ for empty target at 1000 A MeV). Assuming a linear decrease of the beam intensity, the mean attenuation corresponds to the value when the beam reaches half the target. Therefore the number of projectiles was corrected by a factor $f_a = 1 - \varepsilon_a$ taking into account the attenuation of the beam intensity along the target. The value of this factor was also evaluated using Karol's model. To correct for reactions taking place in the target windows (namely Ti) which surrounded the liquid hydrogen, fission yields determined with the empty target following the same analysis procedure were subtracted from the fission yield obtained with the full target.

Finally, the respective fission yields were normalized to the number of projectiles and the number of nuclei in the target per unit area (N_t) to determine the total fission cross section according to the following expression ($N_b = n_b \cdot f_a$ being the corrected number of projectiles):

$$\sigma = \left(\frac{Y_{fiss}^{full}}{N_b^{full}} - \frac{Y_{fiss}^{empty}}{N_b^{empty}} \right) \cdot \frac{1}{N_t} \quad (2.4)$$

The different correction factors and their values are listed in the table 2.1. The independent number of fission events with the empty target at 500 A

MeV could not be determined. To overcome this problem, the yields normalized to the number of projectiles at 300, 800 and 1000 A MeV for the empty target were fitted to a function based on the fission cross-section parametrization proposed by Fukahori and Pearlstein [Fuk90]:

$$\sigma(E_p) = P_1(1 - \exp[-P_3(E_p - P_2)]) \quad (2.5)$$

where E_p is the energy of the projectile, and P_1 , P_2 and P_3 are the fit parameters. We extrapolated the value and the uncertainty of the normalized yield at 500 A MeV from this fit (see Fig 2.8).

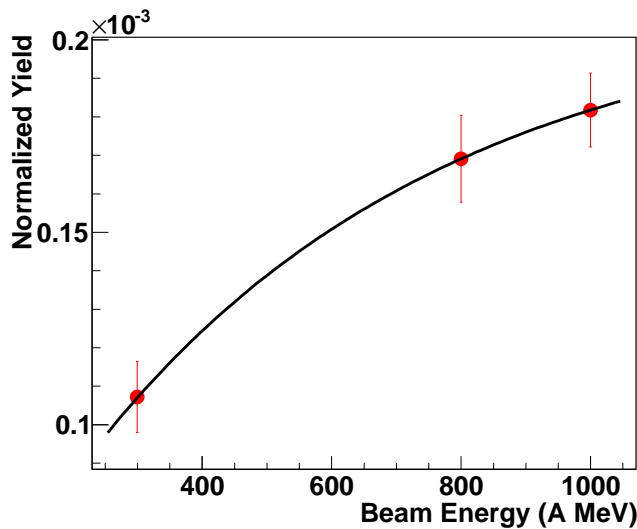


Figure 2.8: Yields normalized to the number of projectiles as a function of the beam energy. The solid line represents the fit to extract the value of the yield at 500 A MeV.

2.2.3. Uncertainties

The main sources of systematic uncertainties were the identification of fission events ranging from 2 to 10% ($\epsilon(n_{fiss})$), the beam intensity ($\approx 5\%$) and the target thickness ($\approx 4\%$). The sources of systematic uncertainty for the different correction factors were also evaluated. The systematic uncertainty of the geometrical correction factor (f_{geo}) was estimated to be smaller than 5%. The evaluation was done by changing the size of the double plastic scintillator gap and the beam profile in our simulation. The value of the systematic uncertainty of the correction factors due to the beam attenuation (f_a)

Energy	Full Target			Empty Target	
	ε_{geo}	ε_d	ε_a	ε_d	ε_a
1000 A MeV	91.1%	2.2%	4.1%	0.4%	0.5%
800 A MeV	92.2%	2.2%	4.0%	0.4%	0.5%
500 A MeV	94.1%	2.2%	3.9%	0.4%	0.5%
300 A MeV	95.35%	2.2%	3.8%	0.4%	0.5%

Table 2.1: Geometrical efficiency (ε_{geo}), beam attenuation (ε_a) and secondary reactions of the fission fragments (ε_d).

and the secondary reactions of the fission fragments (f_d) were smaller than 1 % and almost the same for all energies. Due to the relatively large number of recorded fission events the statistical uncertainties were below 1.5 %. Statistical and systematic uncertainties, other than the ones associated to the beam intensity and target thickness, for the measurements with the full and empty target are presented in Tables 2.2 and 2.3.

Energy	$\epsilon_{stat.}$	$\epsilon(n_{fiss})$	$\epsilon(f_{geo})$	$\epsilon(f_a)$	$\epsilon(f_d)$
1000 A MeV	0.38%	6.01%	4.32%	0.43%	0.22%
800 A MeV	0.39%	7.16%	3.72%	0.41%	0.22%
500 A MeV	0.45%	7.84%	2.80%	0.39%	0.22%
300 A MeV	0.33%	9.51%	2.05%	0.38%	0.22%

Table 2.2: Statistical ($\epsilon_{stat.}$) and systematic uncertainties due to the identification of fission fragments ($\epsilon(n_{fiss})$), geometrical acceptance ($\epsilon(f_{geo})$) and the attenuation ($\epsilon(f_a)$) of the beam in the target (hydrogen + container).

Energy	$\epsilon_{stat.}$	$\epsilon(n_{fiss})$	$\epsilon(f_{geo})$	$\epsilon(f_a)$	$\epsilon(f_d)$
1000 A MeV	1.45%	1.95%	4.32%	0.05%	0.04%
800 A MeV	1.05%	4.56%	3.72%	0.05%	0.04%
500 A MeV	-	-	2.80%	0.05%	0.04%
300 A MeV	0.96%	7.08%	2.05%	0.05%	0.04%

Table 2.3: Same as table 2.2 but for empty target measurements.

2.3. Results and discussion

Using the method described in the previous sections, we have measured with high precision the total fission cross section of ^{181}Ta induced by protons at 300, 500, 800 and 1000 A MeV. The results obtained for each energy are presented in Table 2.4. The magnitude of the measured cross sections is rather small and strongly decreases for the lower beam energies. The associated uncertainties are also rather small ($\approx 10\%$) but increase for the lowest energies ($\approx 18\%$) since the smaller fission cross sections complicates the identification of fission events.

In Fig. 2.9, we present the cross sections obtained in this work as solid points compared to previous measurements by different authors. In this figure, we also present predictions obtained from the systematics established by Prokofiev some years ago [Pro01] (dashed line).

From the analysis of the previously measured cross sections, one can identify some clear discrepancies. At the highest energies, one can find two rather discrepant measurements around 670 MeV by Konshin *et al.* [Kon66] (14.0 ± 1.9 mb) and by Baranovskiy *et al.* [Bar62] (8.0 ± 2.5 mb). At 800 MeV there exists a single measurement by Yurevich *et al.* [Yur05] and at 1000 MeV one finds again two discrepant values obtained by Yurevich *et al.* (15.65 ± 5.4 mb) and Bochagov *et al.* [Boc78] (27.0 ± 1.5 mb). Our results are in very good agreement with the measurement of Yurevich *et al.* at 800 MeV and within the error bars at 1000 MeV, solving the existing discrepancy in this energy range. Moreover, we also confirm the predictions estimated by the systematics of Prokofiev.

In the energy range between 300 and 600 MeV, we can also observe important discrepancies between different measurements. Around 300 MeV the

Energy (A MeV)	Fiss. cross section (mb)	Stat. uncert. (%)	Syst. uncert. (%)
1000	20.17 ± 2.19	0.46	10.85
800	13.09 ± 1.62	0.32	12.34
500	7.53 ± 1.40	0.51	18.54
300	6.55 ± 1.00	0.48	15.21

Table 2.4: Total fission cross sections determined in this work

data obtained by Yurevich *et al.* (5.2 ± 1.6 mb) and Konshin *et al.* (2.6 ± 0.4 mb) differ by a factor two. Around 400 MeV, the measurements by Yurevich *et al.* (5.79 ± 1.78 mb) and Konshin *et al.* (4.7 ± 0.7 mb) are in rather good agreement. However, the measurement by Konshin *et al.* is significantly smaller than the one obtained from the systematics of Prokofiev (7.60 mb). The measurement by Yurevich *et al.* could be compatible with the systematics owing to its large uncertainty. Finally, around 500 MeV the measurements by Konshin *et al.* (8.3 ± 1.1 mb) and Yurevich *et al.* (5.59 ± 1.72 mb) also differ by a large factor. Our measurements at 300 and 500 MeV are consistent with the estimated values from the Prokofiev formula, and, confirm the largest values of the cross sections measured in this region.

From this analysis we can conclude that our data confirm the measurements by Yurevich *et al.* and the cross sections estimated by the systematics above 700 MeV. At lower energies our measurements resolve the discrepancies existing until now. In the energy range between 300 and 600 MeV, our data favor those measurements presenting the highest cross sections. Moreover our data confirm the predictions obtained by the systematics of Prokofiev over the entire energy range covered by this work.

2.4. Reaction model benchmarking

A better insight into the fission probabilities of ^{181}Ta can be obtained using reaction codes based on models describing this process. An overview of the features and characteristics of each code utilized in this work is found in Chapter 1.

Here, we used the INCL4.6 intra-nuclear cascade code [Bou02] describing the interaction between the projectile and the target coupled to the ABLA de-excitation code [Kel09]. The comparison between the experimental data

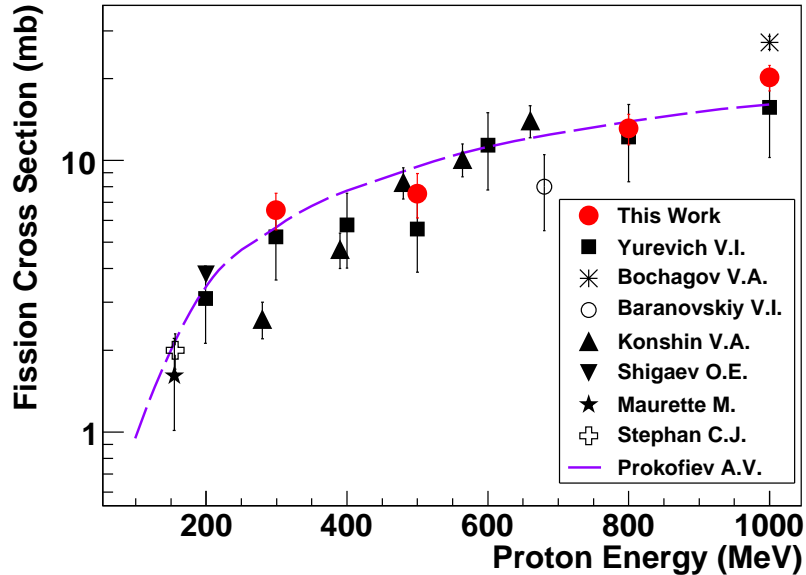


Figure 2.9: Fission cross sections measured in this work (solid circles) in comparison to previously measured data and estimates obtained from the systematics established by Prokofiev (dashed line).

and the calculations for different values of the dissipation coefficient, β , is shown in Fig. 2.10. As can be seen, calculations made according to the statistical model (Bohr-Wheeler) clearly overestimate the fission cross sections in the energy range from 500 MeV up to 1000 MeV (solid line). However, a dynamical description of the fission process with a value of β between 2 and $3 \times 10^{21} \text{ s}^{-1}$, dashed and dotted lines, respectively, provides a good description of the data in that energy range.

The experimental data were also compared with other combinations of codes based on similar formalisms describing fission reactions induced by protons. For the intra-nuclear cascade we used the ISABEL [Yar79] code and for the evaporation stage we used GEMINI++ [Cha88]. The results of the calculations performed with ISABEL+ABLA (solid line) and INCL+GEMINI++ (dashed line) and previous calculations made with INCL+ABLA (dotted line) are shown in Fig. 2.11. Both cascades coupled to ABLA predict similar total fission cross sections over the entire range and both present a good agreement with the experimental data, calculations performed with ISABEL being a little bit better. Calculations with INCL+GEMINI++ yield lower values of the fission cross section. It is worth mentioning that for the lowest

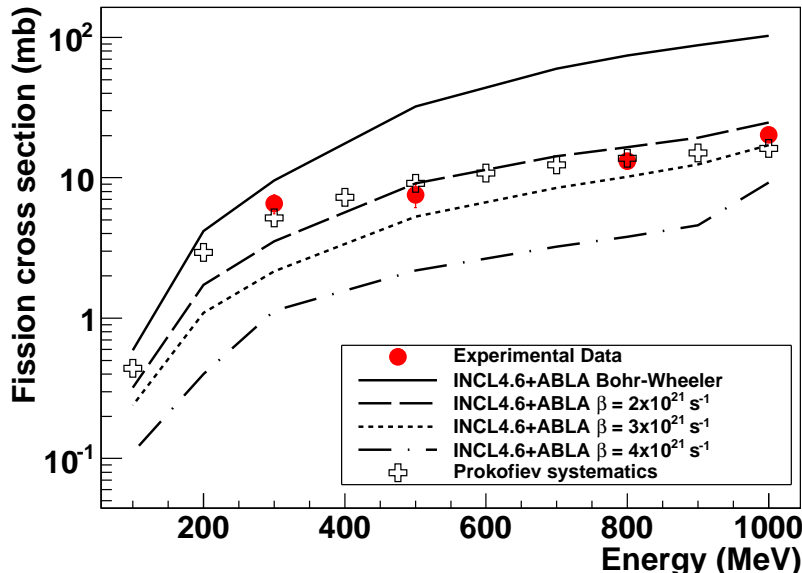


Figure 2.10: Fission cross sections measured in this work (solid circles) in comparison to model calculations using INCL4.6+ABLA for different values of the reduced dissipation coefficient. The cross sections predicted by the systematics are also included.

energies (below 300 MeV), the model predictions underestimate the experimental values measured in this work and the ones obtained according to Prokofiev systematics. Thus, dynamical effects, which do not manifest at those energies, are probably too strong in model calculations performed with ABLA.

In order to better understand the predictive power of these models, we analyzed some other observables that could not be measured in this work but are obtained from the model calculations such as the mass, charge, angular momentum and excitation energy distributions of nuclei undergoing fission. In Fig. 2.12, the thick black line and the thin red line represent the results of calculations of the properties of the prefragments as produced by the intranuclear cascade (INCL or ISABEL) and the properties of the residual nuclei reconstructed using the mass and charge of both fission fragments (A_{res} and Z_{res}), respectively. In the case of the excitation energy, the thin red line represents the distribution of the system at the saddle point. These results allow us to explain the difference in the value of the fission cross section between calculations performed with INCL+ABLA and INCL+GEMINI++.

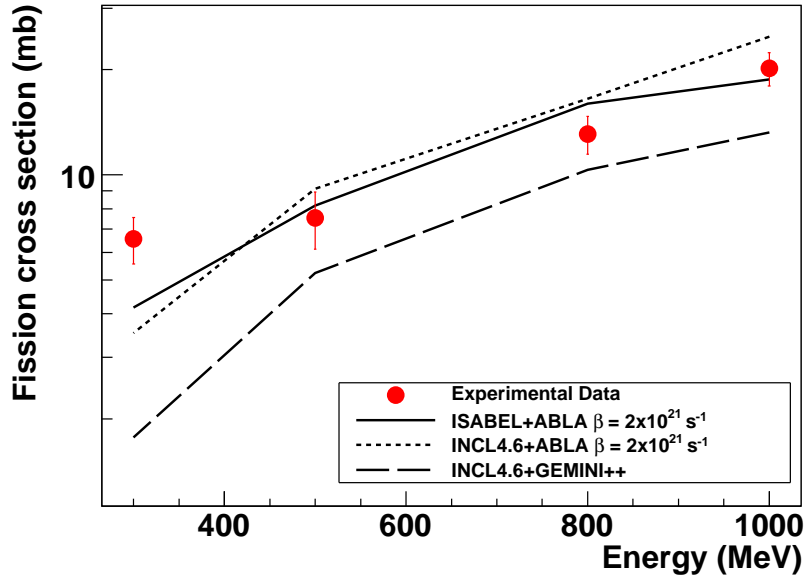


Figure 2.11: Fission cross sections measured in this work (solid circles) in comparison to model calculations using INCL4.6+ABLA and ISABEL+ABLA ($\beta = 2.0 \times 10^{21} \text{ s}^{-1}$), and INCL+GEMINI++.

The main difference between both calculations lies in how GEMINI++ and ABLA treat the decay channels. In GEMINI++ the particle evaporation is slightly enhanced allowing IMF emission reducing the fission probability with respect to ABLA. There exist other parameters such as the spin dependence of the fission barrier or the level-density parameter, that also contribute to this difference in the cross section value. Using an updated ABLA version, which also includes IMF emission, a difference of around 10% in the value of the cross section was found between calculations considering this de-excitation channel and calculations suppressing it.

For all the calculations shown in Fig. 2.12 made considering an energy of the projectile of 1 A GeV, the mean value of the excitation energy of the prefragment is similar. However, calculations performed with ABLA show a reduction of the mean value of the excitation energy at the saddle point due to the nuclear dissipation (around 150 MeV). Moreover, as can be seen, the mean value of the excitation energy at the saddle point and its RMS calculated with INCL+GEMINI++ are both around a factor two larger compared to the ones calculated with INCL+ABLA and ISABEL+ABLA, which means that in the case of GEMINI++, the fission channel opens at

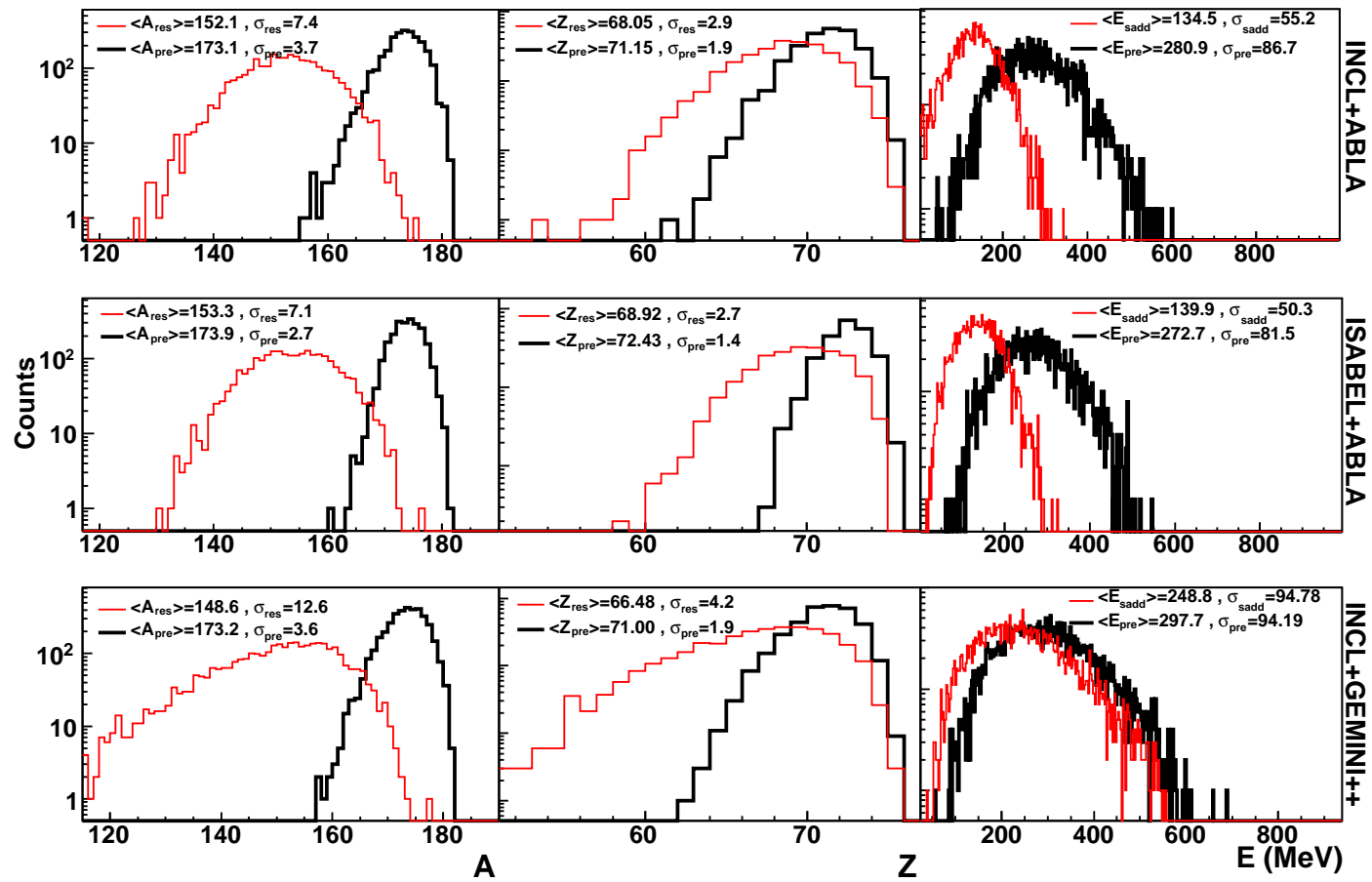


Figure 2.12: Mass, charge and excitation energy distributions of the prefragments produced in the intra-nuclear cascade (thick black line) and the residual nuclei (thin red line) for the reaction $^{181}\text{Ta}+p$ at 1 A GeV, predicted by INCL4.6+GEMINI++, and INCL4.6+ABLA and INCL4.6+ABLA considering $\beta = 2 \times 10^{21} \text{ s}^{-1}$. For the excitation energy distributions, the thin red line refers to the system at the saddle point.

higher excitation energy. According to these results, it seems natural to investigate observables sensitive to the excitation energy at the saddle point to study dynamical effects on the fission process.

Concerning the mass and atomic number of the residual nuclei reconstructed using the mass and atomic number of the final fission fragments (A_{res} and Z_{res}) determined in the evaporation stage (thin red lines), one can see that calculations with ABLA and GEMINI++ predict similar prefragment mass and charge distributions and also similar number of evaporated particles, showing that the de-excitation chain ends at the same point. However, since the energy lost by the system during the ground-to-saddle stage as calculated with GEMINI++ is around 50 MeV on average and the mass and atomic number distributions of the residual nuclei is rather similar for all the calculations, the major part of the particle evaporation is mainly produced during the saddle-to-scission stage, while in ABLA is produced during the ground-to-saddle stage due to the dissipation.

To obtain a clear comparison between the results given by the codes shown in Fig. 2.12, we plotted the mean and the RMS of the distributions as a function of the proton projectile energy in Fig. 2.13 and Fig. 2.14, respectively. This comparison gives us information about the evolution of the distributions as a function of the beam energy. As shown in these figures, the evolution of the mean value and RMS of the mass, charge and excitation energy distributions is similar for all the calculations, having a slight deviation in the case of the charge of the residual nuclei calculated with INCL+GEMINI++ that increases with increasing energy.

From the theoretical stand point, one can find several differences between the description of the fission process included in ABLA and GEMINI++. The latter does not consider the fission delay due to the transient time of the fission process included in ABLA which hinders the fission probability. Thus, in GEMINI++, an increase of the ratio of level-density parameters in the saddle point and ground-state configurations up to $a_f/a_n=1.036$ may account for this reduction [Man10]. It is worth pointing out that in this work, we used this ratio of level-density parameter in calculations done with GEMINI++, while calculations using ABLA were done using a a_f/a_n factor calculated according to the parameterization found in the Ref. [Ign75] (around 1.06 on average) and the strength of the dissipation coefficient whose value may vary in a range between 2 and $3 \times 10^{21} \text{ s}^{-1}$. Larger values of the ratio of level-density parameter lead to larger fission cross sections and therefore this fact explains the lower cross sections predicted by GEMINI++ compared to ABLA predictions.

On the other hand, a clear difference between both intra-nuclear cascades utilized can be observed. Despite calculations done with both INCL and IS-

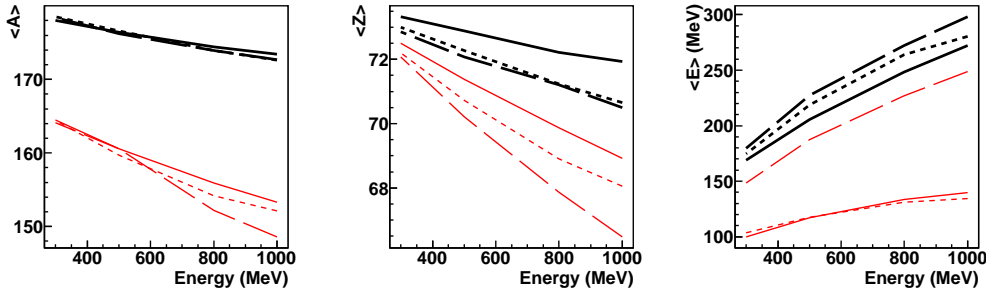


Figure 2.13: Mean value of the mass, charge and excitation energy of the prefragments (thick black lines) and the residual nuclei reconstructed using the mass and atomic number of both fission fragments, A_{res} and Z_{res} (thin red lines) for the reaction $^{181}\text{Ta}+p$ as a function of the beam energy calculated with INCL+ABLA (dotted lines) and ISABEL+ABLA (solid lines) considering $\beta = 2 \times 10^{21} \text{ s}^{-1}$, and INCL+GEMINI++ (dashed lines). For the excitation energy curves, thin red lines refer to the saddle point.

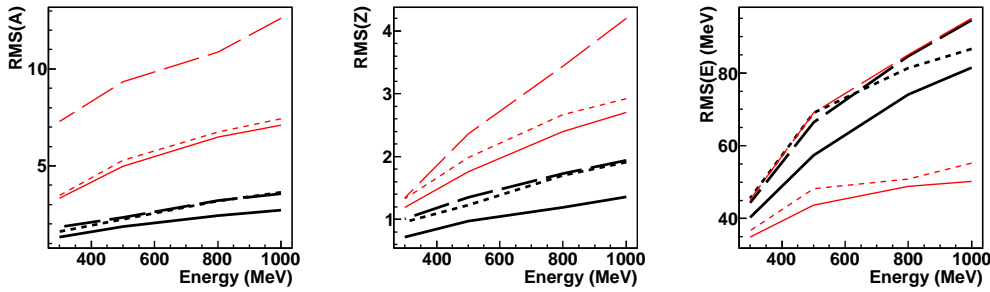


Figure 2.14: Same as fig. 2.13 but for the RMS of the distributions.

ABEL coupled to ABLA yielding consistent values of the fission cross section and similar excitation-energy distributions, there exist some differences in the mean value and RMS of charge distribution of the prefragment calculated by each code, as shown in Fig. 2.13 and Fig. 2.14 (thick lines). Predictions made using ISABEL+ABLA (solid line) show narrower distributions slightly shifted to higher mean values of Z . As shown in Fig. 2.15 angular momentum distributions calculated with INCL+ABLA and ISABEL+ABLA at 1 GeV are rather similar.

The consistency of the models used here can be checked by performing calculations concerning other systems with different fissility and ground-state deformation. A survey of the calculations for different systems is presented in Table 2.5. The predictions of the INCL code coupled to ABLA are in good

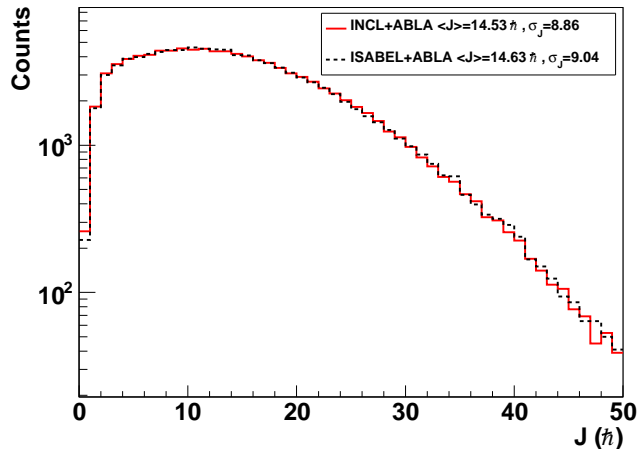


Figure 2.15: Angular momentum distribution of the prefragment calculated with INCL+ABLA (solid red line) and ISABEL+ABLA (dotted black line).

agreement with the experimental data considering a value of the dissipation coefficient of around 3 to $4 \times 10^{21} \text{ s}^{-1}$, therefore, fission cross sections can be estimated with good accuracy. Nevertheless, the sensitivity of the value of β to other parameters such as deformation or temperature, or even other decay channels not considered here, as IMF evaporation, should be further investigated

We have demonstrated before, that, despite calculations with different codes provide similar fission cross section values, other observables such as the mass, charge and excitation energy, which are more sensitive to describe the fission process and characterize the system at the saddle point, present several discrepancies to be addressed. Thus, other experimental signatures are needed in order to completely benchmark the predictive power of the codes, which will allow us to obtain valuable information for the characterization of the fissioning systems and the interpretation of the experimental data. We also conclude that each one of the codes used in this work (INCL, ISABEL, ABLA and GEMINI++) is only sensitive to one of the stages of the process. While the characteristics of the prefragment are completely defined during the cascade stage described by ISABEL or INCL, the de-excitation of the compound nucleus is completely ruled by GEMINI++ or ABLA.

Reaction	Energy	$\sigma_{fis}^{\beta=2.0}$ (mb)	$\sigma_{fis}^{\beta=3.0}$ (mb)	$\sigma_{fis}^{\beta=4.0}$ (mb)	Exp. value (mb)
$^{238}\text{U}+\text{p}$	1 A GeV	1548	1491	-	1530 ± 150 [Ber03]
$^{238}\text{U}+\text{d}$	1 A GeV	2088	2035	1965	2000 ± 420 [Per07]
$^{197}\text{Au}+\text{p}$	0.8 A GeV	-	81	43	65 ± 10 [Ben01]
$^{208}\text{Pb}+\text{p}$	1 A GeV	-	219	140	157 ± 26 [Enq01]

Table 2.5: Fission cross sections of different systems predicted by INCL4.6+ABLA for two different values of the dissipation coefficient.

2.5. Conclusions

We have investigated the proton induced fission of ^{181}Ta in inverse kinematics at 300, 500, 800 and 1000 A MeV. The combination of the inverse kinematics technique with a highly efficient detection setup made it possible to determine the total fission cross sections with high accuracy. The coincident measurement between both fission fragments and their identification from the rough determination of their atomic number allowed to clearly identify and separate the fission events from other reaction channels. This selection is shown to be extremely useful at lower energy when the fission cross section is small and complicates the identification of this reaction channel. The new data has shed light upon the energy region above 700 MeV, where only a few measurements with large uncertainties previously existed. At intermediate energies, the quality of the new data enabled to clarify previous results. Moreover, these new data are in overall good agreement with the systematics established by Prokofiev over the entire energy range.

A comprehensive comparison of the experimental data with different state-of-the-art models describing fission was made to get a better insight into the dynamics of the fission process and benchmark the codes. Both intra-nuclear cascade codes used in this work (INCL and ISABEL) coupled to ABLA de-excitation code provide a rather good description of the measured fission cross sections, taking into account a dynamical picture of fission.

On the other hand, INCL coupled to the GEMINI++ evaporation code based on a statistical description of the fission width, underestimates the experimental values obtained in this work compared to the ones obtained with INCL+ABLA and ISABEL+ABLA due to a lower level-density parameter value. In addition, we have proven that GEMINI++, the system undergoes fission at higher excitation energy in comparison to ABLA. We have also demonstrated that the evaporation of the particles in GEMINI++ is made during the saddle-to-scission stage, while in ABLA is produced during the

ground-to-saddle transition owing to the nuclear dissipation being the energy at the saddle point the most important observable.

We also stated the main discrepancies between both intra-nuclear cascade codes (INCL and ISABEL) and both de-excitation models (ABLA and GEMINI++) when calculating the mass and charge distributions of the prefragment and its excitation energy at the saddle point. We have demonstrated that calculations performed with INCL and ISABEL yield rather similar predictions concerning total fission cross sections. In conclusion, despite that fission cross sections providing valuable information to benchmark the codes, other observables are needed to fully characterize their predictive power to investigate the fission dynamics.

Chapter 3

Proton- and deuteron-induced fission on ^{208}Pb at 500 A MeV

Spallation reactions induced in heavy-mass nuclei lead to highly excited nuclei characterized by low angular momentum and near distortion free shapes. In this scenario which fulfills the conditions established by Grangé and collaborators (see section 1.1.3), one can investigate the dynamics of the fission process at high excitation energies. In this work in particular, we study transient and dissipative effects experienced by fissile systems produced by bombarding ^{208}Pb nuclei with protons and deuterons at 500 A MeV. Several signatures sensitive to these dynamical effects, such as the total and partial fission cross sections and the width of the fission fragments charge distribution are extracted from these experiments which provide valuable experimental information concerning the magnitude of the nuclear dissipation and the manifestation of a finite fission delay. Moreover, the use of protons and deuterons allows to investigate the effect of the excitation energy induced in the system following the collision.

On the other hand, since lead is a low-cost material and a good high-energy neutron emitter under proton bombardment it is also considered as a prospective material for the construction of spallation neutron targets and its performance under such conditions have to be investigated. Nevertheless, the situation is similar to that of ^{181}Ta and a great experimental effort is needed in order to address the discrepancies of previously measured data and to benchmark nuclear-reaction codes and systematics used to predict the behaviour of a large variety of target nuclei under particle irradiation over a wide range of energy.

The detection setup utilized in this experiment is an improved version of the ^{181}Ta experimental scheme detailed in chapter 2.1. Here, the previous setup was complemented with two new detectors: A double ionization cham-

ber that allowed us to identify with high resolution the nuclear-charge of both fission fragments (Z_1 and Z_2) simultaneously with an efficiency higher than 90% and a time-of-flight (ToF) wall which was used to determine the vertical position of the reaction products. These new observables will allow us to characterize the fissioning system at the saddle point which provide a more robust interpretation of the transient and dissipative effects present in the fission process, assuming no proton evaporation from ground to saddle and saddle to scission. As we have demonstrated in the previous chapter, these observables will also allow a more complete benchmark of the reaction models used to describe the fission process.

In the first part of this chapter, a brief overview of the setup and a detailed description of both new detectors is given. In the second part, we will explain the procedure to identify the fission events in order to determine the fission-fragment charge distribution, reconstruct the charge of the fissioning nuclei and calculate the total and partial fission cross sections. We will discuss the improvements with respect to the previous method explained in section 2.2. Following this, we will focus on the analysis and interpretation of the observables inferred from the measurement of the nuclear-charges of the fission residues, the partial fission cross sections and the width of the charge distributions. Finally, the observables will be compared with calculations performed with the codes to extract conclusions about dissipative and transient effects in fission.

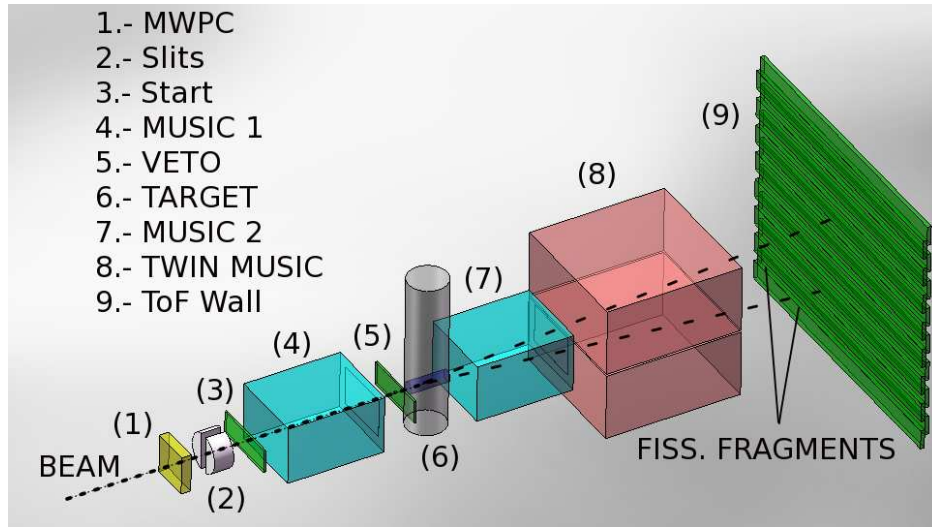


Figure 3.1: Schematic drawing of the experimental setup used in the present experiment.

3.1. Description of the experimental setup

Following the experimental procedure based on inverse kinematics, a ^{208}Pb ion beam was accelerated at the SIS-18 synchrotron. As can be seen in Fig. 3.1, the position of the beam at the entrance of the setup was measured with a Multi-wire proportional chamber (MWPC [Ste91]) and the collimation was made with iron slits. To measure the beam dose, we used the scintillator (start) placed upstream of the first ionization chamber (MUSIC) situated before the target and the veto scintillator being used to reject misaligned beam particles. The first scintillator (start) was also used to define the data acquisition trigger. The target consisted of a cell filled with liquid hydrogen (85 mg/cm^2) or deuterium (201 mg/cm^2), depending on the reaction to be studied. This target was isolated by two windows consisting of titanium foils of $15 \text{ }\mu\text{m}$ of thickness and five layers of Al-coated mylar strips of $30 \text{ }\mu\text{m}$ of thickness. The target cell was surrounded by two multi-sampling ionization chambers (MUSIC). In this experiment we used another model of the MUSIC detector with 6 anodes and filled with P10 gas (90% Ar and 10% CH_4). Only the 4 central anodes were used for the read out of the induced signals because the external anodes were used to preserve the homogeneity of the electric field. The operation principle of the chamber is the same as explained in section 2.1. The MUSICs were used to identify reactions of the beam particles with the layers of matter upstream of the hydrogen target and in the target itself. The detection of both fission fragments simultaneously was made via a double ionization chamber (Twin MUSIC) with high charge resolution, efficiency and acceptance. Due to the kinematics of the reaction both fission fragments are boosted in the forward direction and detected in both parts of the Twin MUSIC. Here, the double paddle scintillator was not installed to avoid secondary reactions of the fission fragments and only the beam trigger provided by the first scintillator was considered for the acquisition. The last detector included in this setup was a time-of-flight wall whose purpose was to measure the position and the velocity of the fission fragments as well as a rough determination of nuclear-charges. In the following we will describe the two new additional detectors used in this experimental setup, already described in chapter 2.

3.1.1. Twin MUSIC

The Twin MUSIC detector [Sch00] (see Fig 3.2) is a double ionization chamber consisting of two active volumes (800 mm long, 200 mm height and a width of 300 mm) of the same dimension filled with P10 gas and separated by a common central cathode placed horizontally, with two windows of

25 μm aluminized Kapton. The cathode was supplied with -4000 V and two groups of four anodes, placed at the top and bottom of the chamber, with 1000 V each. This creates an uniform electric field in both sections of the chamber guiding the electrons liberated due to the ion's passing to drift to the anodes where the signal is induced and read out from each side of the anode (16 signals) by the pre-amplifiers. Two Frisch-grids placed 2 cm in front of the anodes with 0 V were used to reduce the position dependence of the primary ionization. The signal is proportional to the energy loss of the ions, and therefore, to its nuclear-charge. A charge resolution of around $\Delta Z/Z = 0.55$ was achieved in the present experiment. The anodes were designed with a triangular geometry to allow the measurement of the horizontal position of the fragments. The vertical position is determined from the drift time of the electrons measured in each anode (8 signals). The position resolution achieved with this chamber is around 500 μm and 6 mm in the vertical and horizontal direction, respectively. The position of the cathode in the setup was coincident with the height of the beam in order to maximize the geometrical efficiency of the setup and avoid the recombination of the positively-charged non-fissioning projectiles with the electrons released in the ionization of the gas by the fission fragments. The pre-amplified signals are sent to a shaping amplifier to filter the lower frequencies and improve the resolution then digitized using a V785 ADC and V775 TDC, both CAEN VME modules.

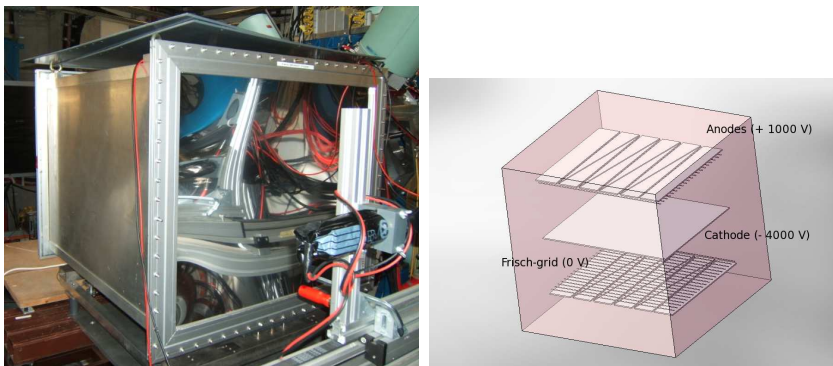


Figure 3.2: Picture of the Twin MUSIC detector and schematic representation of the two active volumes with the central cathode and the anodes.

3.1.2. Time-of-flight wall

The time-of-flight wall (ToF wall, see Fig. 3.3) consisted of 15 BC420 scintillator paddles of 1 m long, 10 cm high and 5 mm thick disposed horizontally

in two planes (front and rear) covering an area of 1 m^2 [Sch00]. Each paddle in the front (rear) plane had an overlap of 3.3 cm in the vertical direction with the adjacent paddles situated in the rear (front) plane. One additional paddle was mounted in vertical position to facilitate the time calibration of the other scintillator paddles. The paddles are coupled to HAMAMATSU H2431se1 fast photomultipliers in both extremes which enabled measuring the horizontal position. The granularity in the vertical direction (3.3 cm) allowed to determine the vertical position of both fission fragments. This detector was proposed as a solution for the measurement of the velocities of the fission residues with high resolution and determine their atomic charge. The time resolution of this ToF wall is around 170 ps (FWHM).



Figure 3.3: Picture of the ToF Wall.

3.2. Identification of the fission fragments

The selection of the fission fragments was done using the information of both MUSICs surrounding the target and the information given by the double ionization chamber and the ToF wall. In the left panel of Fig. 3.4 the energy loss of ions in both MUSICs is shown. In the diagonal of this scatter plot, ions with different atomic number that did not interact with the target are represented. These ions were produced in nuclear reactions of the lead beam with layers of matter placed upstream of the target. The vertical line represents residual heavy nuclei and emitted light fragments from evaporation processes produced in the interaction of ^{208}Pb beam particles

with the target. The energy loss of nuclei in the MUSICs is proportional to their atomic number squared (Z^2) and considering $\Delta E_{f.f.} \propto Z_1^2 + Z_2^2 = Z_{beam}^2/2$, where $\Delta E_{f.f.}$ is the energy loss of both residues in the MUSIC 2, the fission fragments are located around channel 500 on the MUSIC 2 energy loss axis. Furthermore, a selection in the MUSIC 1 was made in order to reject ions with nuclear charges lighter than ^{208}Pb and count the number of lead projectiles (see right panel of Fig. 3.4).

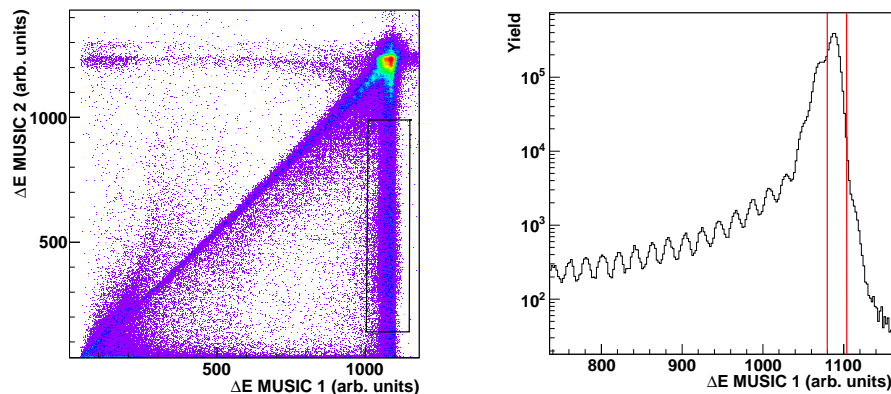


Figure 3.4: Left panel: Scatter plot of the amplitudes of the signals registered with the two MUSIC detectors. The rectangular selection represents the region where fission residues were expected. Right panel: Energy Loss signals provided by the MUSIC 1. The region between the red lines corresponds to ^{208}Pb beam particles.

Focusing on the region in the scatter plot of both MUSICs where the fission fragments are expected (rectangular selection represented in the upper panel of Fig. 3.4), fission events were easily identified combining the energy loss of each fission fragment in each part of the double ionization chamber, as shown in the two-dimensional energy-loss spectrum in Fig. 3.5. The solid line encloses the events of interest. This method used to identify and isolate fission events had higher precision compared to that used in the ^{181}Ta experiment, owing to the clear separation of the fission products from the fragmentation and evaporation backgrounds in the Twin MUSIC detector.

3.2.1. Nuclear-charge calibration

The energy loss of both fragments measured in the Twin MUSIC was transformed into atomic charge considering that $Z \propto \sqrt{\Delta E}$. The square root of the energy-loss signals of the selected fission events is represented in a

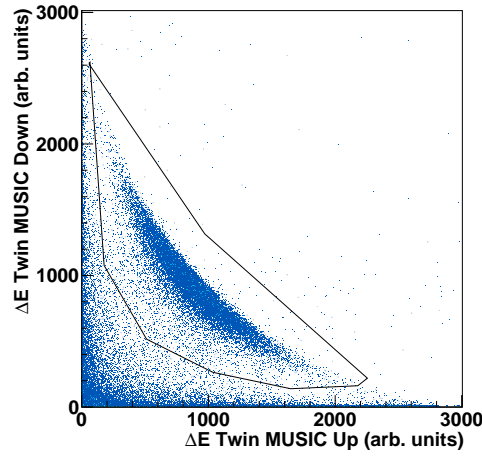


Figure 3.5: Two-dimensional spectrum of the energy-loss amplitude signals of the fission fragments recorded separately in the Twin MUSIC detector. The solid-line box encloses the fission events.

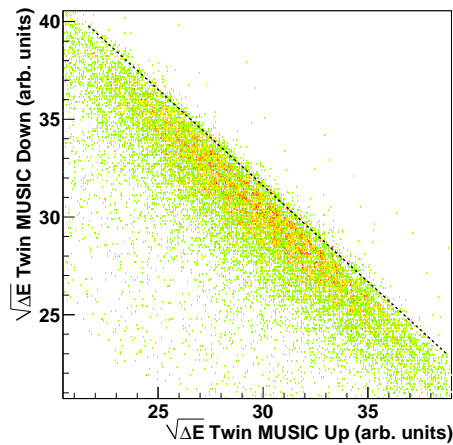


Figure 3.6: Same as Fig. 3.5 but for the square root of the energy-loss of both fragments. The dotted line represents the charge of the fissioning nucleus $Z_1 + Z_2 = 83$.

two-dimensional plot shown in Fig. 3.6. Here, the diagonal lines correspond to different charges of the fissioning nuclei ($Z_1 + Z_2$). The absolute calibration in atomic number Z was performed using the sum spectrum of the charges of both fragments $Z_1 + Z_2$ (Fig. 3.7), assuming that the peak with highest value

of Z_1+Z_2 corresponds to fission after the exchange of one proton of the target with one neutron of the projectile ($Z=83$), and the adjacent peak on the left with higher intensity corresponds to the atomic number of the projectile $Z=82$. One can also see a peak with very low intensity on the right of the $Z_1+Z_2=83$ peak, corresponding to $Z_1+Z_2=84$. The resolution of the detector was found to be $\sigma=0.55$ charge units (around 1.4%). The calibration of the nuclear charge distribution for each fission fragment is explained in Annex A.

Aside from the calibration in charge of both parts of the detector, we also determined with this procedure the charge of the fissioning nucleus for the $^{208}\text{Pb}+p$ and $^{208}\text{Pb}+d$ reactions, assuming that fission fragments do not lose protons. The distributions of $Z_{fiss}=Z_1+Z_2$ (charge of the fissioning system) are shown in Fig. 3.7. At first glance one sees that in the collision with deuteron, the excitation energy induced in the reaction is larger than the proton one since more nucleons are removed from the projectile, which allow us to produce fissile systems with lower Z_{fiss} .

3.2.2. Detection efficiency

Both fission fragments had a non-negligible probability of passing through the same part of the Twin MUSIC owing to the alignment of the chamber with the beam axis and the beam emittance. Also fragments may pass close to the cathode which also derives in an incorrect detection due to the inhomogeneity of the electrical field in that region. The overall detection efficiency was therefore reduced since the condition to recognize a fission event is that detection occurs in both parts of the Twin MUSIC. To evaluate the losses we calibrated both the position and the angle of the fragments inside the chamber. The horizontal position of the fragments was given by the triangular geometry of the anodes. The position was calculated considering that:

$$x(mm) = 300 \frac{Q^l - Q^r}{Q^l + Q^r} \quad (3.1)$$

where the factor 300 corresponds to the length of the anodes and Q^l and Q^r are the charges of the signal induced in the anodes that were read out from left and right side, respectively. Using this procedure, we calculated the position in the fourth anode of the Twin MUSIC.

The vertical position was determined using the difference of the drift times measured in the first and the fourth anode of both parts of the chamber and the vertical position on the ToF Wall where the fragments impinged. Figure 3.8 shows a sketch of the fission fragment trajectories inside of Twin MUSIC chamber and its impact point at the segmented ToF Wall. As we

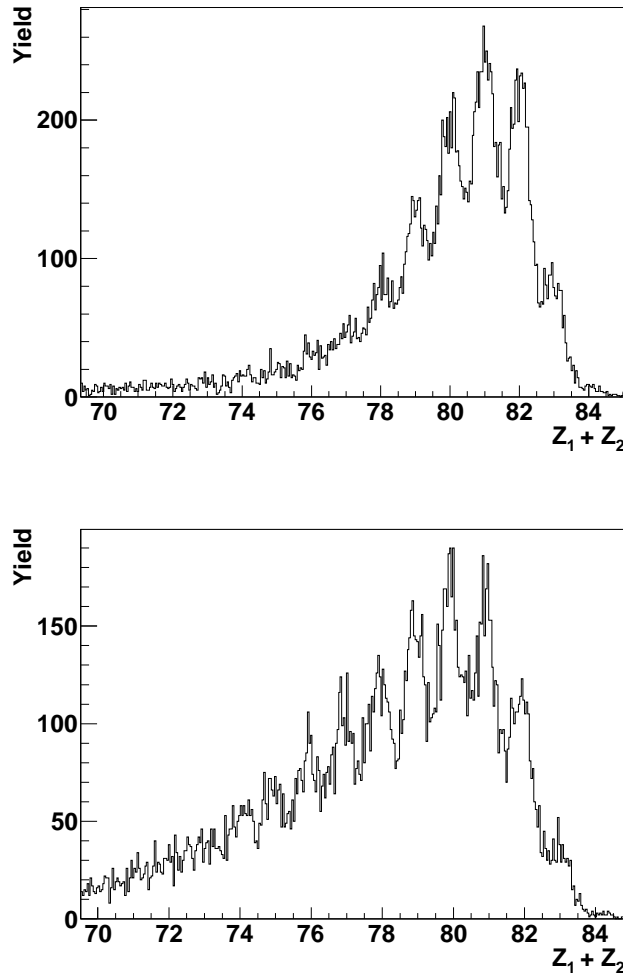


Figure 3.7: Sum spectrum of the nuclear charges of the fission fragments $Z_1 + Z_2$ obtained in the reaction $^{208}\text{Pb}+p$ (upper panel) and $^{208}\text{Pb}+d$ (lower panel).

mentioned before, each paddle in the ToF Wall had an overlap of 3.3 cm with its respective neighbours defining a detection cell. In addition, due to this configuration, a cell of 3.3 cm was defined in the centre of each paddle without any overlap. Thus, the rough position of the fission residues corresponded to the height of the cells where the fragments impinged. The position calibration was made representing the spectra of the drift time differences recorded in both parts of the Twin MUSIC in coincidence with different cells of the wall (see left panel of Fig. 3.9). In order to do this, we considered double multiplicity, which is to say, the arrival of each fragment to a different cell

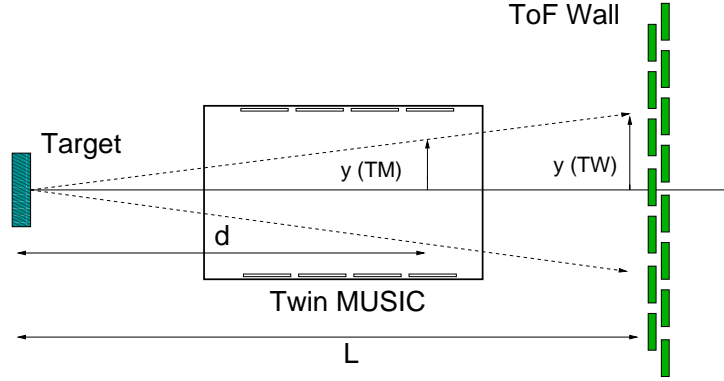


Figure 3.8: Determination of the vertical positions in the ToF Wall and in the fourth anode of the Twin MUSIC.

of the ToF Wall, one over and one below the beam line, respectively. The paddle situated in the beam line was not considered for calibration effects. As can be seen in Fig. 3.9, each drift time distribution is limited by the physical size of the different cells. Therefore, the drift times were calibrated taking into account the vertical position of each cell in the ToF Wall using the following linear correlation:

$$y^{TW} = a (T_4^d - T_1^d) + b \quad (3.2)$$

where T_4^d and T_1^d are the drift times measured in the first and fourth anode, respectively. The a and b coefficients were inferred from the linear fit of the points represented in the right panel of Fig. 3.9. The position of the fragments in the fourth anode of the Twin MUSIC (y^{TM}) were calculated considering the distances of the anode (d) and the ToF Wall (L) from the target using the geometrical relation:

$$y^{TM} = y^{TW} \frac{d}{L} \quad (3.3)$$

To determine the detection efficiency of the Twin MUSIC, the spatial two-dimensional distribution of the fragments at the position of the fourth anode of the Twin MUSIC, represented in the left panel of Fig. 3.10, was extrapolated for all detected fission events. The distribution had a dimension of around $20 \times 20 \text{ cm}^2$ and an expected symmetric ring shape due to the Coulomb repulsive force between both fragments. To evaluate the losses due to fragments passing close to the cathode of the chamber and the misalignment of the beam, the two-dimensional distribution of Fig. 3.10 (left panel) was projected into the y -coordinate axis (right panel). The depression in

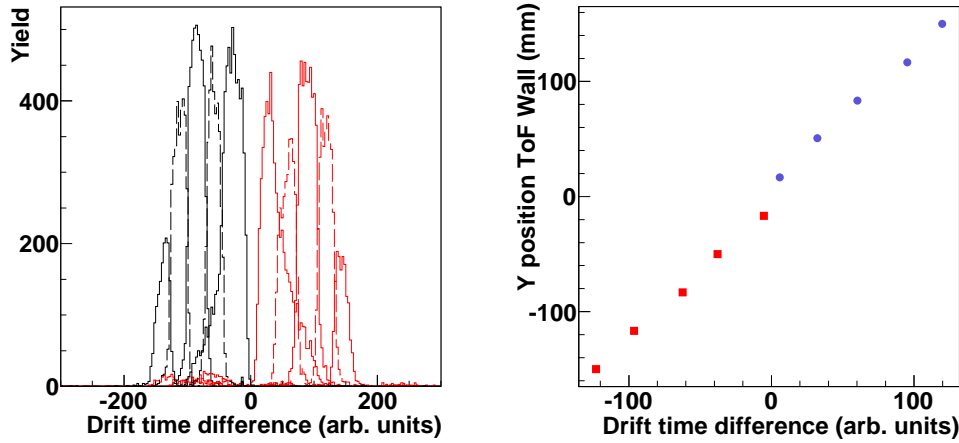


Figure 3.9: Left panel: Difference of the drift times measured in the first and fourth anode of both parts of the Twin MUSIC in coincidence with each cell. Right panel: Calibration of vertical position of the boundaries of the different cells as a function of the drift time. Red squares and blue circles refer to the lower and the upper part of the Twin MUSIC, respectively.

the centre of the spectrum was caused by fragment losses and it allowed to determine the efficiency of the chamber by fitting this spectrum using a rectangular function convoluted with a Gaussian distribution due to the different velocities caused by the mass split of the fission fragments, as represented in the right panel of Fig. 3.10. The symmetry of the experimental spectrum was distorted due to a malfunction of the upper part of the Twin MUSIC when registering fragments near the cathode. Around 4% of the total amount of fission events were registered with negative drift time differences which induced a systematic uncertainty.

A Monte Carlo simulation, already explained in section 2.2, was performed to evaluate the uncertainty in the determination of the Twin MUSIC efficiency considering the beam emittance and the distance of the fourth anode of the Twin MUSIC from the target. For the simulation, we considered a beam with a gaussian profile with $\sigma=0.4$ cm (according to the experimental value) with an angular straggling of 1 mrad due to the first plastic scintillator and the MUSIC placed before the target. The geometrical efficiency of the chamber and its uncertainty was evaluated introducing a variable-size dead zone due to the cathode thickness in the detection plane. The height of this zone with respect to the center of the beam was also slightly varied to account for the beam misalignment. Thus, in this simulation we evaluated

the number of fission fragments lost in the cathode and the number of events where both fragments traversed the same part of the Twin MUSIC. Since in this calculation we only considered geometrical limits, the simulated spectrum presented sharp edges in the dead zone as shown in Fig. 3.11, contrary to the experimental spectrum, where the position is determined by the drift time difference. With this information, the efficiency of the Twin MUSIC was estimated to be $92 \pm 5\%$ for $^{208}\text{Pb} + \text{p}$ and $^{208}\text{Pb} + \text{d}$ reactions. The nominal value of the efficiency was extracted from the experimental spectrum, whereas the uncertainty was determined by comparison with the simulation.

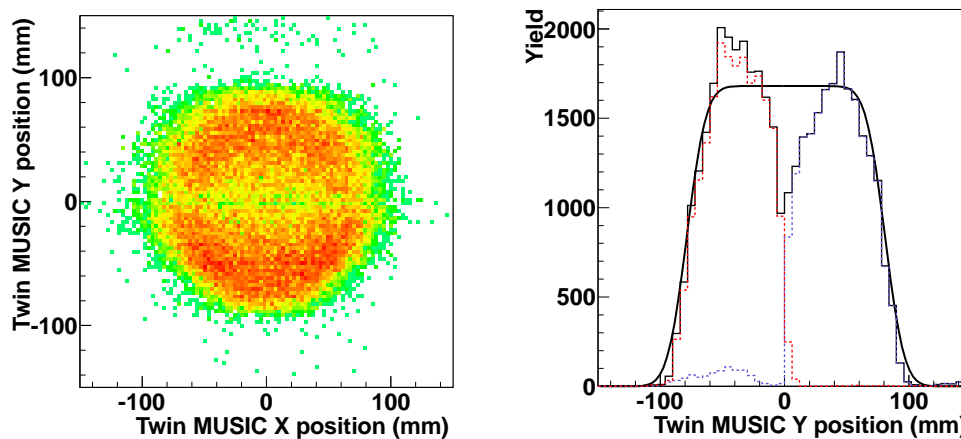


Figure 3.10: Left panel: Calibrated two-dimensional distribution of the fragments in the detection plane perpendicular to the beam direction for the reaction $^{208}\text{Pb} + \text{p}$ at 500 A MeV (see text for details). Right panel: Projection of the distribution into the y axis. The thick solid line represents a fit with a rectangular function convoluted with a Gaussian. The red dashed and blue dashed distributions correspond to fission fragments detected in the lower and upper part of the Twin MUSIC, respectively.

3.3. Total fission cross section

One of the main motivations of this experiment was the precise measurement of the total fission cross sections induced by protons and deuterons to address the existing discrepancies of previous measurements, in particular the data measured in experiments performed at the FRS (FRagment Separator at GSI [Gei92]). To determine the total fission cross sections, the fission yields Y_{fiss} were calculated with the following expression:

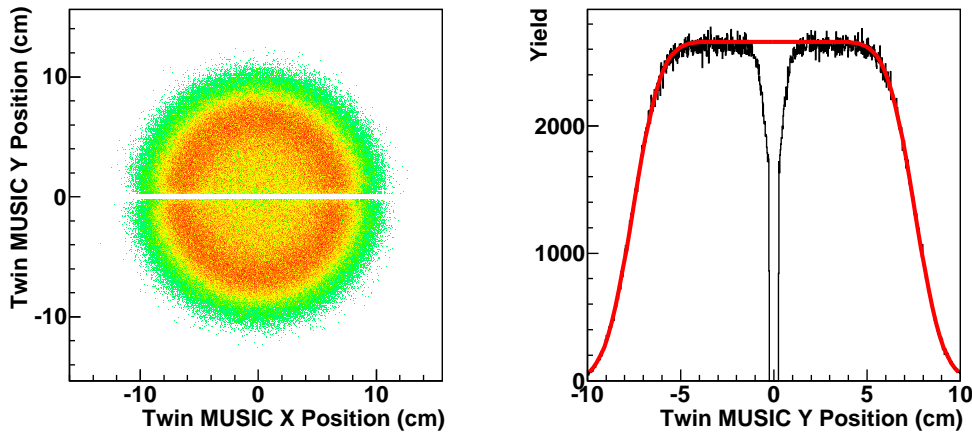


Figure 3.11: Simulation of the spectra shown in Fig. 3.10.

$$Y_{fiss} = n_{fiss} \cdot f_d \cdot f_{geo} \cdot f_b \quad (3.4)$$

where n_{fiss} is the number of measured fission events, $f_{geo} = 1/\varepsilon_{geo}$ is the geometrical correction factor and ε_{geo} the Twin chamber efficiency, f_d is the correction factor due to secondary reactions of the fission fragments in the target and f_b is the correction factor due to the fragmentation background. We counted the number of fission events n_{fiss} , which were unambiguously identified inside the polygonal selection of the Twin MUSIC energy loss plot in Fig. 3.5. Furthermore, the contamination of the fragmentation background was estimated by projecting the two-dimensional spectrum of the nuclear charges of the fission fragments registered by the Twin MUSIC onto an axis perpendicular to the $Z_1 + Z_2 = 82$ axis direction (see Fig. 3.6), and then fitting the projected spectrum with the sum of two exponential functions, drawn in Fig. 3.12. With the area of the functions, we inferred the amount of background underneath the fission region, ε_b , which amounted to less than 3% for measurements with proton, deuterium and empty target. Hence, the number of fission events was corrected by a factor $f_b = (1 - \varepsilon_b)$.

Secondary reactions of the fission residues in layers of matter placed between the target and the entrance of the Twin MUSIC were evaluated using Karol's microscopic model [Kar75]. The correction factor is $f_d = 1 / (1 - \varepsilon_d)$, where ε_d is the number of reactions which amount to less than 4% for full target and less than 0.5% for the empty target for both reactions studied in this work.

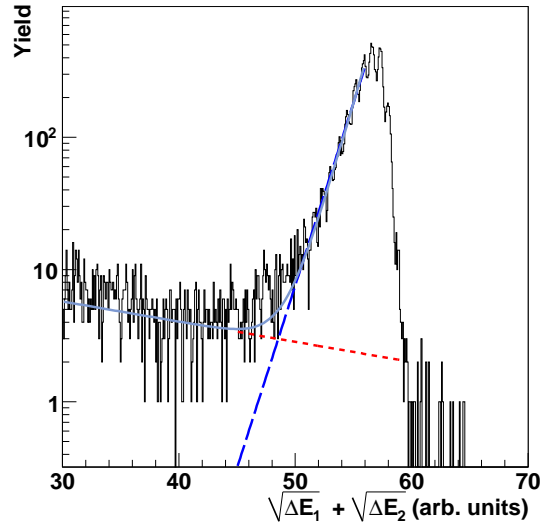


Figure 3.12: Projection of the fission region along an axis perpendicular to $Z_1 + Z_2 = 82$. ΔE_1 and ΔE_2 refer to the energy loss in the upper and lower part of the Twin MUSIC. The dashed line and the dotted line are the exponential functions fitted to the fission and background regions, respectively. The solid line represents the sum of both functions. The plot refers to the reaction $^{208}\text{Pb}+p$ at 500 A MeV.

The number of measured lead projectiles n_b was determined with the spectrum of the MUSIC 1 represented in the right panel of Fig. 3.4 and the first plastic scintillator, which also provided the only trigger for the data acquisition. We applied a correction, f_a , to the total number of projectiles due to the attenuation of the beam intensity along the target thickness. The mean attenuation of the beam, ε_a , was calculated considering a linear decrease of the beam intensity and corresponded to the value after crossing half the target. Calculations were done according to Karol's model. Thus, the number of real projectiles was evaluated following $N_b = n_b \cdot f_a$ where $f_a = (1 - \varepsilon_a)$. The values of the different correction factors are shown in Table 3.1.

Fission yields with empty target were determined in order to subtract the contribution of fission reactions taking place in any layer of matter surrounding the target cell. The total fission cross sections were obtained by normalizing the real fission yields for full (Y^{full}) and empty (Y^{empty}) target, to the number of projectiles (N_b) and the number of nuclei in the target per unit area (N_t):

Reaction	ε_a	ε_d	ε_{geo}	ε_b
$^{208}\text{Pb}+\text{p}$	4.72%	4.33%	94%	2.54%
$^{208}\text{Pb}+\text{d}$	6.05%	5.54%	94%	2.12%
$^{208}\text{Pb}+\text{empty}$	0.5%	1.35%	94%	2.87%

Table 3.1: Different correction factors: Twin MUSIC efficiency (ε_{geo}), beam attenuation (ε_a), secondary reactions of the fission fragments (ε_d) and fragmentation background ε_b for each reaction studied in this work.

$$\sigma = \left(\frac{Y_{fiss}^{full}}{N_b^{full}} - \frac{Y_{fiss}^{empty}}{N_b^{empty}} \right) \cdot \frac{1}{N_t} \quad (3.5)$$

The value of the fission cross sections are listed in Table 3.2. The associated uncertainties were determined with a precision for the total fission cross sections of around 7%. The main contributions to the systematic uncertainty were the uncertainties of the target thickness ($\approx 4\%$), beam intensity ($\approx 5\%$), determination of the fission yields (1.24%, 2.61% and 3.56% for proton, deuteron and empty target respectively) and corrections factors (less than 12%). Furthermore, we considered a systematic uncertainty of 2% due to misidentified events with negative drift time in the upper part of the Twin MUSIC. The statistical contributions amounted to less than 1% in both cases.

Reaction	Fiss. Cross Sections	Stat. uncert.	Syst. uncert.
$^{208}\text{Pb}+\text{p}$ 500 A MeV	152 ± 10 mb	0.88%	6.53%
$^{208}\text{Pb}+\text{d}$ 500 A MeV	207 ± 14 mb	0.74%	6.54%

Table 3.2: Total fission cross sections determined in this experiment.

We compared the results with previously measured data found in the literature listed in table 3.3. For the reaction $^{208}\text{Pb}+\text{p}$ at 500 A MeV, data measured at the FRS amounted to total fission cross section of 232 ± 33 mb [Fer05] having a non-negligible deviation with respect to the result obtained in this work (232 ± 33 mb) non explained by the associated uncertainties. The precision achieved in the measurement performed at the FRS was constrained

by the limited acceptance of the spectrometer requiring large correction factors. Also, at the FRS, Enqvist and collaborators [Enq01; Enq02] obtained for the reaction $^{208}\text{Pb}+p$ and $^{208}\text{Pb}+d$ at 1 A GeV a fission cross section of 157 ± 26 mb and 169 ± 31 mb, respectively.

Similar measurements were performed in direct kinematics by Vaishnene *et al.* [Vai10] measuring a value for the fission cross section of 110 ± 7 mb and 129 ± 10 mb with a proton beam of 505 and 1000 MeV, respectively. These measurements used a scintillator counter telescope to count the beam dose and PPAC detectors (Parallel Plate Avalanche Counter) to detect the fission fragments. These cross sections are smaller than the ones obtained in this work, but also at the FRS. However they confirm the almost constant value of the total fission cross section between 500 and 1000 MeV. The use of the direct kinematics technique could prevent fission fragments to escape from the target reducing the total fission cross section. Thus, this fact would explain the lower value of the fission cross section obtained by Vaishnene and collaborators with respect to the one measured in this work. Furthermore, we compared the values of the cross sections obtained in this work with the systematics established by Prokofiev. There exists a discrepancy between the predicted values (112 mb) and our data of around 20%. It is worth pointing out that the systematics were based on evaluation of cross sections measured before 2001 with a limited amount of data, especially at 500 A MeV where the information was non-existing.

Neutron-induced fission on lead at similar energies was also investigated by Tarrío and collaborators at nToF (CERN) [Tar11]. The experiment was performed bombarding a natural lead target with neutrons with energies up to 1 GeV. The fission fragments were detected in coincidence using PPAC detectors. They obtained a total fission cross section of 97 ± 7 mb at 500 MeV and 116 ± 10 at 1000 MeV measuring the ratio between the yields of ^{nat}Pb and ^{238}U , and extracting the value of the latter from an evaluated nuclear data library (JENDL). Again these measurements confirm the almost constant value of the total fission cross section between 500 and 1000 MeV. In the case of the neutron-induced fission, lower fission cross sections are expected due to the composition of the ^{nat}Pb target and the charge-exchange reaction channel. One has to consider that natural lead is composed of several lead isotopes, which also induce slight variation in the fission cross section with respect to the ^{208}Pb case. In addition, the neutron skin of lead isotopes [Kra04] inhibits the elastic charge-exchange channel for the most peripheral collisions under neutron bombarding, while in the case of the proton it is allowed. Thus, this represents another reaction channel to induce fission

It is worth explaining the evolution of the fission cross sections as a function of the energy of the projectile. One can see that this evolution for the

Reaction	This work	FRS	Other
$^{208}\text{Pb}+\text{p}$ 500 A MeV	152±10 mb	232±33 mb [Fer05]	110±7 mb [Vai10]
$^{208}\text{Pb}+\text{d}$ 500 A MeV	207±14 mb	-	-
$^{208}\text{Pb}+\text{p}$ 1 A GeV	-	157±26 mb [Enq01]	129±10 mb [Vai10]
$^{208}\text{Pb}+\text{d}$ 1 A GeV	-	169±31 mb [Enq02]	-
$\text{n}+^{nat}\text{Pb}$ 500 MeV	-	-	97±7 mb [Tar11]
$\text{n}+^{nat}\text{Pb}$ 1 GeV	-	-	116±10 mb [Tar11]

Table 3.3: Total fission cross sections measured in different experiments.

reaction $^{208}\text{Pb}+\text{p}$ obtained comparing the results achieved in this work and the ones measured by Enqvist and collaborators, is consistent with the one obtained by Vaishnene and collaborators. For the former comparison (this work and results by Enqvist), one sees that the fission cross section slightly increases (around 5 mb) with energy increasing from 500 up to 1000 MeV. This result is consistent within the error bars with the increment of around 30 mb obtained by Vaishnene and collaborators. Moreover, as can be seen in the case of $^{208}\text{Pb}+\text{d}$, the fission cross section decreases with energy increasing in the same energy range, when comparing the results obtained in this work with the ones obtained by Enqvist, being the relative variation, around 37 mb, similar to the one of the $^{208}\text{Pb}+\text{p}$ reaction within the error bars. In the case of the neutron-induced fission of ^{208}Pb , there exist also an increase of the fission cross section of around 20 mb between 500 and 1000 MeV of neutron energy, in good agreement with the proton-induced case.

According to this discussion, we can deduce that the value obtained at the FRS in the work of Ref. [Fer05] is incompatible with the relative slight variation of the fission cross sections in the energy range considered before for $^{208}\text{Pb}+\text{p}$, $^{208}\text{Pb}+\text{d}$ and $\text{n}+^{nat}\text{Pb}$ reactions, and furthermore, this value is greater than the fission cross section of the $^{208}\text{Pb}+\text{d}$ reaction at 500 A MeV (about 25 mb) which is expected to be larger than the fission induced by protons at the same energy, as we have demonstrated in this work.

3.4. Partial fission cross sections

Partial fission cross sections, for both $^{208}\text{Pb}+\text{p}$ and $^{208}\text{Pb}+\text{d}$ reactions, were obtained by determining the fission yields for full and empty target for each Z_1+Z_2 value. Similarly to the procedure we used in the previous

section to determine the total fission cross sections, we deduced each yield normalizing the number of fission counts registered for each fissioning system to the total number of ^{208}Pb projectiles. Correction factors depending on the atomic number of the fissioning system were applied to the measured yields to obtain the real yield. Then, after subtracting the empty target contribution, we normalized each real yield to the number of nuclei in the target per unit area N_t according to equation 3.5. The results are shown in the plot of Fig. 3.13 and listed in the table 3.4.

Z_1+Z_2	σ_p (mb)	σ_d (mb)
84	0.58 ± 0.11	0.48 ± 0.10
83	11.11 ± 0.82	7.14 ± 0.53
82	28.84 ± 2.00	18.60 ± 1.26
81	32.72 ± 2.26	26.55 ± 1.76
80	26.73 ± 1.86	26.12 ± 1.73
79	18.13 ± 1.29	24.38 ± 1.61
78	10.91 ± 0.81	21.03 ± 1.40
77	6.72 ± 0.53	17.76 ± 1.20
76	3.91 ± 0.35	14.00 ± 0.96
75	2.10 ± 0.24	11.45 ± 0.80
74	1.48 ± 0.20	8.54 ± 0.62
73	0.95 ± 0.17	6.58 ± 0.50

Table 3.4: Values of the partial fission cross sections for $^{208}\text{Pb}+p$ (σ_p) and $^{208}\text{Pb}+d$ (σ_d) at 500 A MeV.

The maximum value for the cross section for both reactions is found at $Z_1+Z_2=81$. The partial cross section gradually decreases with decreasing Z_1+Z_2 since the fission barriers become higher as more nucleons are removed from the fissioning nuclei. Therefore, higher excitation energies are needed to undergo fission. Since in the $^{208}\text{Pb}+d$ reaction the average excitation energy induced in the system is expected to be larger, fission cross sections

are also higher and fissile systems with lower Z_1+Z_2 values are produced when compared to the $^{208}\text{Pb}+p$ case. It is worth pointing out that for values of $Z_1+Z_2 > 80$, there exists a difference between both curves that can be explained in terms of impact parameter. In the case of very peripheral collisions where single nucleon-nucleon cross sections are highly probable, the lead projectile might interact either with the proton or the neutron of the deuteron. Owing to this reason the expected partial fission cross sections decrease since the total fission cross section induced by neutrons is lower than the one induced by protons (see section 3.3). Events with $Z_1+Z_2=83$ and 84 correspond to projectiles which underwent fission following a single or double charge-exchange reaction [Kel04], respectively. Due to these reasons, partial fission cross sections are expected to be sensitive to the intra-nuclear cascade governing the first stage of these collisions.

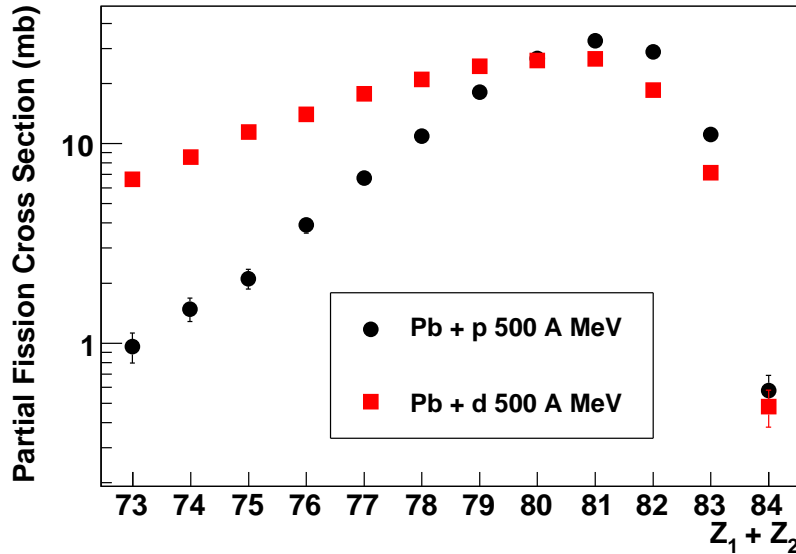


Figure 3.13: Partial fission cross sections. Solid circles and solid squares refer to $^{208}\text{Pb}+p$ and $^{208}\text{Pb}+d$ at 500 A MeV, respectively.

3.5. Width of the charge distribution of fission fragments

Another signature we exploited in this work is the widths of the fission-fragments charge distributions (σ_z) determined for each fissioning system

Z_1+Z_2 . This observable which represents a probe of transient effects in fission at high excitation energies was introduced in the work of Jurado and collaborators measuring the fission process on ^{238}U at 1 A GeV [Jur04], and it was also studied for spherical radioactive heavy nuclei in the work of Schmitt and collaborators [Sch10]. As stated in chapter 1, the temperature of the fissioning nuclei at the saddle point (T_{sad}) affects the width of the charge distribution following the equation:

$$\sigma_z^2 \approx (Z_{fiss}/A_{fiss})^2 \sigma_A^2 = Z_{fiss}^2 T_{sad} / (16d^2V/d\eta^2) \quad (3.6)$$

A_{fiss} and Z_{fiss} being the charge of the of the fissioning nuclei, respectively, and $(16d^2V/d\eta^2)$ is the mass asymmetry potential stiffness where $\eta = (4/A_{fiss}/(M - A_{fiss}/2))$ is the mass asymmetry. A value for the integral charge distribution of the fission fragments σ_z of 6.7 ± 0.7 charge units and a mean value of the nuclear charge of 39.97 ± 0.83 was measured in the present experiment for the $^{208}\text{Pb}+p$ reaction, in rather good agreement with the value of 6.3 ± 0.3 charge units of the Ref. [Fer05]. For the $^{208}\text{Pb}+d$ reaction, we have obtained in this work a value for the integral charge distribution of the fission fragments of 7.0 ± 0.5 charge units. Going a step further, the evolution of the temperature T_{sad} and therefore the excitation energy at the saddle point, was investigated by measuring σ_z for each Z_1+Z_2 value. Larger values of the width of the distribution correspond to higher temperature at the saddle point and conversely. The charge distributions are shown in Fig. 3.14 where one sees that the mean value of the distribution, as expected, decreases with decreasing Z_1+Z_2 [Sch10].

On the other hand, the width of the distribution increases for lower values of Z_1+Z_2 since the excitation energy of the fissioning nuclei is higher, as can be seen in Fig. 3.15. This figure also shows that the width of the fission fragments charge distribution has the same value and the curves follow the same evolution for both reactions within the errors bars for each Z_1+Z_2 value independently of whether a proton or deuterium target is used. This relevant fact indicates that the width of the fission fragments charge distribution does not depend on the entrance channel and only depends on the de-excitation mechanism and in particular on the temperature reached by the system at the saddle point for a given Z_1+Z_2 . These results can be validated with previous measurements where spherical heavy nuclei at 420 A MeV, with a fissility comparable to that of ^{208}Pb , yielded similar values of the width of the fission fragment charge distribution as a function of Z_1+Z_2 [Sch10]. One also sees that the width of the distribution slightly increases with Z_1+Z_2 decreasing owing to larger temperature at saddle required to fission light systems with smaller fissility.

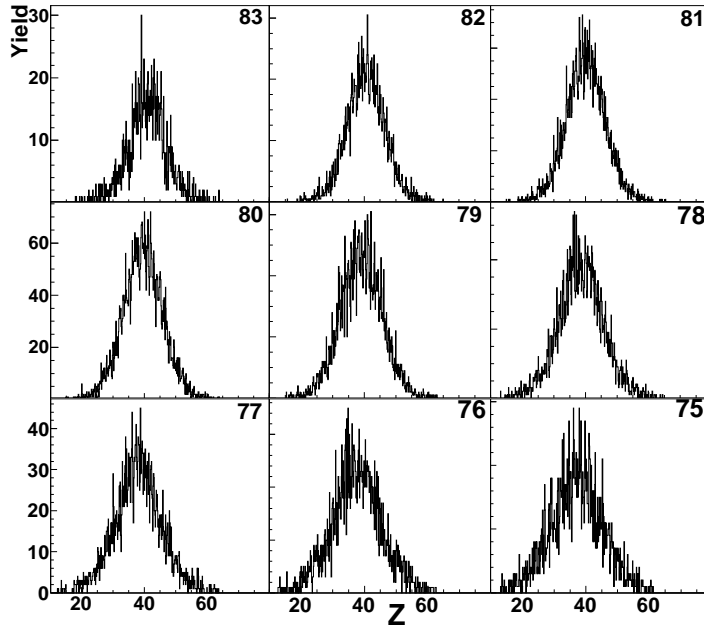


Figure 3.14: Experimental widths of the charge distribution of the fission fragments. The number in the upper right corner represents each $Z_1 + Z_2$ value.

It is worth mentioning that all the distributions were corrected due to the geometrical efficiency of the Twin MUSIC chamber. The correction process is explained in Annex A.

3.6. Comparison with model calculations

In order to infer information about the influence of nuclear dissipation in the fission of ^{208}Pb at high excitation energy, calculations with state-of-the-art codes were also performed in this case. For this purpose, we have used two different intra-nuclear cascade codes, INCL [Bou02] and ISABEL [Yar79], describing the interaction stage. These codes were coupled to the statistical de-excitation code ABLA [Kel09]. As already explained in previous chapters, it is worth pointing out that all calculations taking into account the nuclear dissipation were performed considering also a time-dependent fission width described by an analytical solution of the FPE (Fokker-Planck Equation described in chapter 1).

In Fig. 3.16 the experimental values of the partial fission cross sections for $^{208}\text{Pb}+p$ and $^{208}\text{Pb}+d$ reactions are compared to these model calculations. As can be seen, in general, calculations performed with INCL+ABLA

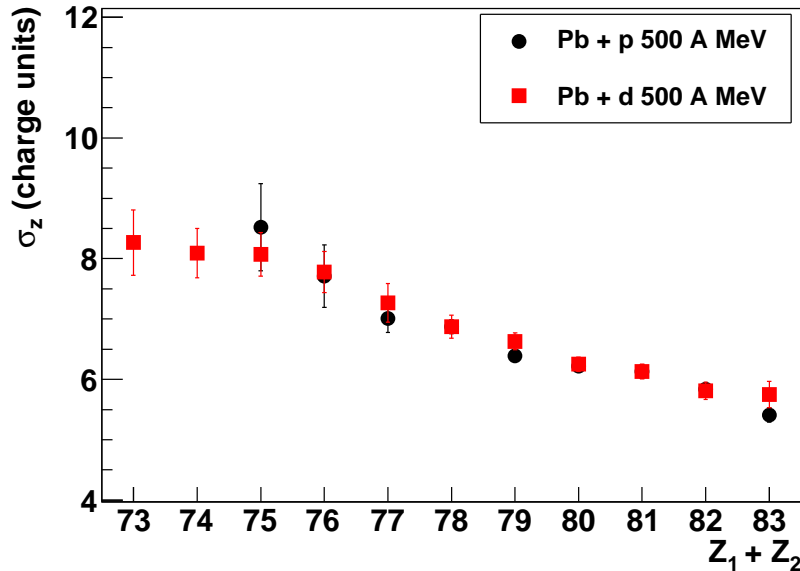


Figure 3.15: Width of the charge distribution of the fission fragments for each Z_1+Z_2 value. Solid circles and solid squares refer to $^{208}\text{Pb}+p$ and $^{208}\text{Pb}+d$ at 500 A MeV, respectively.

for the reaction $^{208}\text{Pb}+p$ at 500 A MeV considering Bohr-Wheeler statistical fission width (solid black line) overestimate the experimental values, while calculations considering fission dynamics with a value for the reduced dissipation coefficient of $\beta = 4 \times 10^{21} \text{ s}^{-1}$ (dashed black line) have a good agreement in the range from $Z_1+Z_2=80$ up to 82. However, partial fission cross sections of fissile systems with higher excitation energies ($Z_1+Z_2 < 80$) are not properly reproduced. Calculations performed with ISABEL+ABLA with the same value of the dissipation coefficient provide a poor description of the experimental data in all the range of Z_1+Z_2 .

Since the shape of the partial fission cross section is different for each intra-nuclear cascade model, this observable seems to be sensitive to the excitation energy and angular momentum induced to the system during the first stage. However, the absolute value of the partial fission cross sections seems to depend on the magnitude of the dissipative coefficient used in the de-excitation stage. Calculations made for the $^{208}\text{Pb}+d$ reaction at 500 A MeV with INCL+ABLA codes are presented together with the experimental data in Fig. 3.17. The model predictions considering $\beta = 4 \times 10^{21} \text{ s}^{-1}$ (dashed-dotted line) describe rather well the experimental data in almost

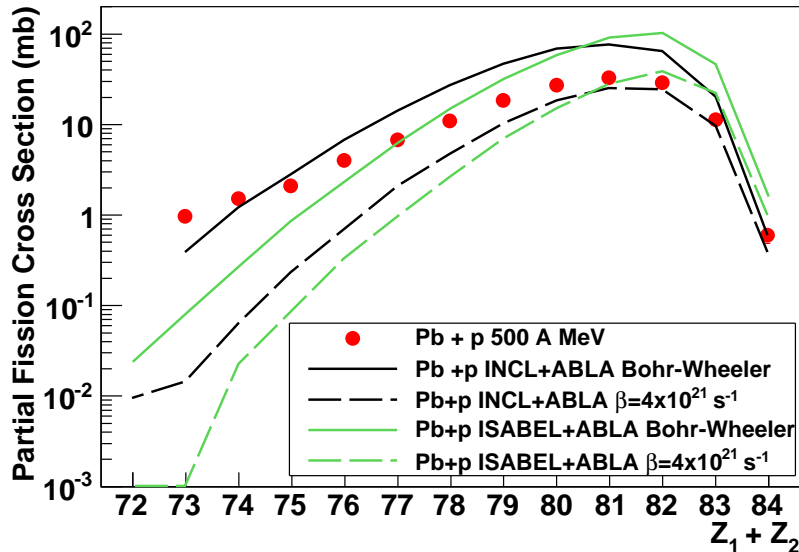


Figure 3.16: Partial fission cross section as a function of Z_1+Z_2 for the reaction $^{208}\text{Pb}+p$ at 500 A MeV compared to several calculations performed with INCL+ABLA (black) and ISABEL+ABLA (green) with $\beta = 0$ (solid line) and $\beta = 4.0 \times 10^{21} \text{ s}^{-1}$ and a time-dependent fission width (dashed line), respectively.

the entire energy range studied here. Calculations performed according to Bohr-Wheeler's statistical model overestimate the experimental values (solid line). The version of the ISABEL code used in this work cannot be used to calculate deuteron-induced reactions.

It is worth mentioning that both intra-nuclear cascade codes provide similar total fission cross sections, 96 and 114 mb for INCL and ISABEL ($\beta = 4 \times 10^{21} \text{ s}^{-1}$), respectively. This result indicates that the total fission cross section does not represent a robust observable since a deeper insight into the main properties of the fissioning systems reveals that a total characterization of the fissioning system with respect to other observables like partial fission cross sections and the width of the fission fragments charge distribution is needed in order to benchmark such codes.

We have demonstrated that INCL code provides a better description of the partial fission cross section of the reaction $^{208}\text{Pb}+p$ compared to ISABEL, but at high excitation energies ($Z_1+Z_2 < 78$) calculations with INCL underestimate the experimental values.

Contrary to the fission probability where the modification of the fission barrier and angular momentum of the fissioning system caused by the evap-

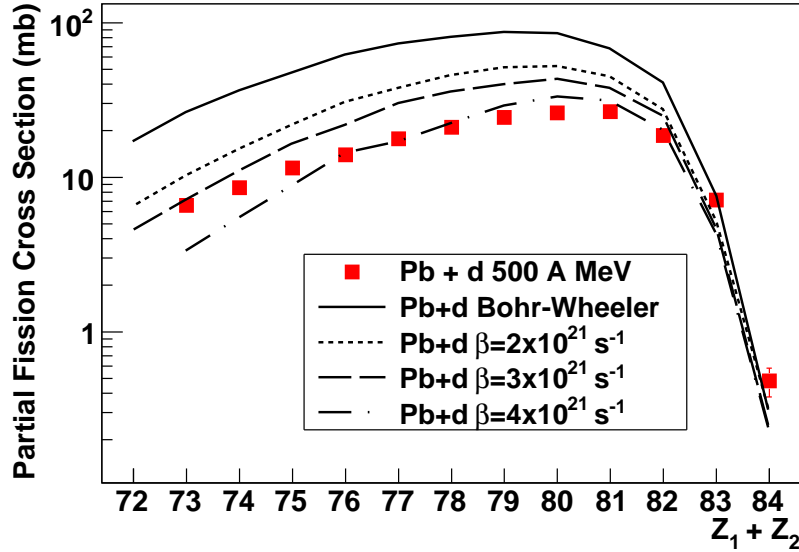


Figure 3.17: Partial fission cross sections as a function of $Z_1 + Z_2$ for the reaction $^{208}\text{Pb} + d$ at 500 A MeV compared to calculations performed with INCL+ABLA for different values of β .

oration of particles smear out transient effects, the width of the fission fragments charge distribution is expected to be sensitive to pre-saddle dynamics due to its strong connection with T_{sad} . Rich information can be extracted from the comparison of the experimental data with calculations performed with INCL+ABLA. As can be seen in Fig. 3.18, calculations for $^{208}\text{Pb} + p$ at 500 A MeV according to the Bohr-Wheeler statistical model (solid line) and Kramers picture considering the time independent fission hindrance induced by dissipation with $\beta = 4 \times 10^{21} \text{ s}^{-1}$ (dash-dotted line), overestimate the experimental values. Predictions using a value of the dissipation coefficient of $\beta = 4 \times 10^{21} \text{ s}^{-1}$ and a time-dependent fission width described by an analytical solution of the FPE, show a drastic reduction of the width of the distributions (dashed line refers to $^{208}\text{Pb} + d$ and dotted line refers to $^{208}\text{Pb} + p$ both at 500 A MeV), and thus, of T_{sad} . This reduction of the width of the distribution corresponds to a lower temperature at the saddle point, T_{sad} , caused by the fission delay that enhances the evaporation of lighter particles, mainly neutrons, cooling down the nucleus.

The value of the dissipation parameter β determined in this work is consistent with the ones obtained in other works where the same observables were studied. In the work of Benlliure and collaborators [Ben02] where the

proton-induced fission of ^{197}Au was investigated, a value for the reduced dissipation coefficient of $\beta = 2 \times 10^{21} \text{ s}^{-1}$ was obtained by comparison of the experimental value of the width of the integral charge distribution of the fission fragments with calculations performed with the same code used in this work but with a description of the fission process including a time-dependent fission width described by a step-function.

Jurado and collaborators obtained a value of the the dissipation coefficient of $\beta = 2 \times 10^{21} \text{ s}^{-1}$ investigating the fission induced in peripheral collisions of ^{238}U at relativistic energies (1 A GeV). They compared their experimental values of the width of the fission fragments charge distribution as a function of the atomic number of the fissioning system (Z_1+Z_2) with model calculations performed with ABRABLA including a time-dependent fission width, in this case described by an analytical solution of the FPE equation. From the same observable and using a similar procedure but studying the fragmentation of spherical radioactive nuclei, Schmitt *et al.* [Sch10] obtained a value of the dissipation strength of $\beta = 4.5 \times 10^{21} \text{ s}^{-1}$.

These results are consistent with the ones obtained in this work, and with the calculations performed to compare the fission cross section of the $^{181}\text{Ta}+p$ at different relativistic energies, where a value of the dissipation strength of $\beta = 2 \times 10^{21} \text{ s}^{-1}$ was inferred (see chapter 2). Moreover, we have seen there that calculations performed comparing other nuclei with very different fissility are also in very good agreement. Thus, we have demonstrated that a comparison of the experimental values with model calculations is consistent for several systems studied here considering a value of the dissipation strength ranging from $\beta = 2$ to $4 \times 10^{21} \text{ s}^{-1}$.

In conclusion, the comparison of the experimental data with several calculations performed with INCL+ABLA and ISABEL+ABLA provide valuable information about the behaviour of a fissioning system at high excitation energy. While partial fission cross sections are used to benchmark the intranuclear cascades, the width of the fission fragments charge distribution validates the performance of the evaporation code we have utilized for these calculations. Therefore, one can see that each signature is sensitive to one stage of the process. Furthermore, we have demonstrated that a dynamical picture of the fission process considering a time-dependent fission width allowed to reproduce the experimental results. These results are consistent with the ones obtained in the works of Ref. [Jur04] and Ref. [Sch10], where transient and dissipative effects on the fission process were studied using the same observable, σ_z as a function of Z_1+Z_2 .

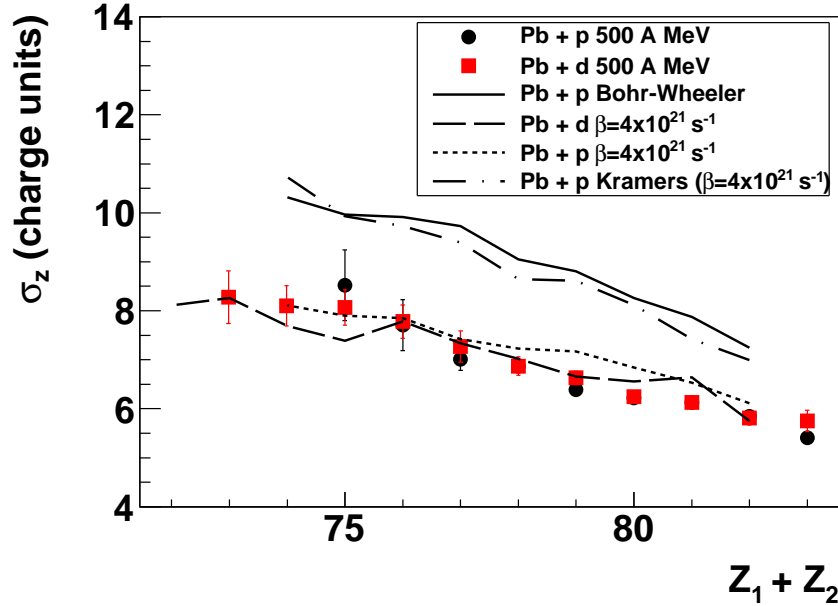


Figure 3.18: Width of the charge distribution as a function of $Z_1 + Z_2$ for both reactions studied in this work compared to calculations performed with INCL+ABLA.

3.7. Conclusions

In the present chapter we investigated proton- and deuteron-induced fission of ^{208}Pb at 500 A MeV of energy. A dedicated experimental setup adapted to the inverse kinematics technique was used to unambiguously detect both fission fragments in coincidence with high acceptance and efficiency and determine their atomic number. With this information we reconstructed the charge of the fissioning system $Z_1 + Z_2$, which allowed us to determine several observables sensitive to dissipative and transient effects in fission. We determined with high precision the total and the partial fission cross sections as a function of the atomic number of the fissioning system and the width of the fission-fragments charge distribution, for both reactions. The total fission cross sections obtained in this work were compared with fission cross sections measured in other experiments in order to address some discrepancies. Different measurements of the total fission cross section on lead induced by protons and neutrons indicate a small variation with the energy between 500 and 1000 MeV. Therefore, previous measurements of the $^{208}\text{Pb} + \text{p}$ reaction at 500 A MeV at the FRS seem to overestimate the total fission cross section [Fer05].

The dynamics of fission was studied using the partial fission cross sections and the width of the fission fragments charge distribution, since each one of these observables seems to be sensitive to each one of the stages of the fission process. Partial fission cross sections provide valuable information about the intra-nuclear cascade stage revealing that deuteron-induced fission leads to higher excited fissioning systems with respect to the reaction induced by protons at the same energy per nucleon. Concerning the width of the fission fragments charge distribution as a function of Z_1+Z_2 , since for both reactions we obtained similar values, we conclude that this observable is only sensitive to the de-excitation mechanism, in particular the temperature at the saddle point, since it does not depend on the reaction used to produce the fissioning system.

In addition, we have compared the results obtained in this work with the theoretical predictions yielded by a combination of an intra-nuclear cascade code (INCL and ISABEL) coupled to the statistical ABLA code describing the de-excitation of the compound nucleus. For the reaction $^{208}\text{Pb}+d$ at 500 A MeV, calculations made with INCL+ABLA are in good agreement with the experimental values concerning the total and the partial fission cross sections, considering $\beta = 4 \times 10^{21} \text{ s}^{-1}$ and a time-dependent fission width. Despite calculations performed with ISABEL+ABLA provided a value of the total fission cross section consistent with the one obtained with INCL+ABLA, the partial fission cross sections calculated with the former provide a poor description of the experimental data. Therefore, we proved that the characteristics of the fissioning system are well defined during the intra-nuclear cascade stage described by these codes and they provide different results according to the excitation energy and angular momentum induced to the system.

Concerning the de-excitation process which is studied with ABLA, we have demonstrated that a statistical description of the process according to Bohr-Wheeler's statistical model leads to an overestimation of the experimental widths of the fission fragment charge distribution (σ_z). However, calculations considering $\beta = 4 \times 10^{21} \text{ s}^{-1}$ and a time-dependent fission width are in rather good agreement with the experimental values of σ_z . Therefore, this comparison of the experimental results with calculations performed with ABLA de-excitation code supports the manifestation of transient and dissipative effects on the fission process at high excitation energies. These results are consistent with other works showing the influence of transient and dissipative effects on the fission process through the same observable [Jur04; Sch10].

In conclusion, fission at high excitation energies can be described as a two-step partially decoupled process where the properties of the fissioning system are defined during the first stage and the de-excitation mode, in which

74 Proton- and deuteron-induced fission on ^{208}Pb at 500 A MeV

dissipative effects and transient delay play a key role, is determined during a second stage. This was proved with experimental observables sensitive to each stage and with model calculations supporting these signatures.

Chapter 4

New time-of-flight detectors for future fission experiments

In the previous chapters we have demonstrated that a dedicated experimental setup is mandatory in order to provide accurate data on fission fragment nuclear charges. Substantial progress has been accomplished in the understanding of the fission process dynamics with the available technology utilized in these experiments. However, the measurement of other observables requires a more complex detection system, and therefore, an experimental effort is being carried out to improve the resolution, acceptance and efficiency of the current detectors for future experiments. One of the main challenges is the complete characterization of the two fission fragments in atomic and mass number that will be made by including in new experimental setups, based on the ideas presented in [Sch00], a dipole magnet and a state-of-the-art time-of-flight (ToF) and tracking detectors with unprecedented resolution. Considering a flight-path of a few metres and a mass resolution of around $\Delta A/A = 3 \times 10^{-3}$, a demanding time resolution of the order of tens of picoseconds is needed to isotopically separate fission fragments masses, therefore, the choice of a proper detection technology is critical for such a ToF wall detector.

This chapter is devoted to the R&D carried out in order to design a ToF wall based on timing Resistive Plate Chambers (tRPCs). In the first section, a brief review of three future experiments to be conducted at GSI to investigate fission (SOFIA, R³B and FELISE) will be presented. Within the framework of the R³B experiment, we will explain the main requirements and constraints of a ToF wall for the detection of relativistic ions. Accordingly, we will compare two different technologies for the design of this ToF wall: organic scintillators coupled to fast photomultipliers and Resistive Plate Chambers (RPCs). An intensive R&D was undertaken by our group

to prove the feasibility of RPCs for the detection of relativistic heavy ions, especially for those with typical fission fragments masses. We constructed several prototypes equipped with front-end electronics (FEE) developed by our group. The performance of these prototypes under heavy ion irradiation is the main contribution of this work. Finally, in the last section we will present the conceptual design of the modules that may constitute the final detector.

4.1. Future fission experiments at GSI

4.1.1. SOFIA

SOFIA (Studies On Fission In Aladin) is a new generation fission experiment in inverse kinematics that will be performed at GSI. The goal of such experiment is the accurate measurement of the fission yields of radioactive actinides with masses up to $A = 238$ ($^{219-232}Ac$, $^{220-236}Th$, $^{225-237}Pa$, $^{230-238}U$ and $^{233-238}Np$) and stable nuclei such as ^{208}Pb . These radioactive nuclei will be produced at the FRS, delivered with an energy around 600 A MeV to the ALADIN/LAND experimental area [LAN], where the fission setup based on [Sch00] will be located. An schematic view of the setup is represented in Fig. 4.1. An active target consisting of several lead and uranium layers will be used to induce the fission of the projectile either via electromagnetic excitation or nuclear reaction. A double ionization chamber will detect both fission fragments in coincidence, determining their nuclear charges after a velocity correction. The accurate isotopic identification of the fission fragments will be made using the magnetic field of the ALADIN dipole magnet following the relation:

$$\frac{A}{Z} \sim \frac{B\rho}{\beta\gamma} \quad (4.1)$$

where B is the dipole magnetic field, ρ is the curvature of the particle inside the field, and $\beta\gamma$ is the reduced momentum. The velocity of the fission fragments will be determined with a time-of-flight measurement using a plastic scintillator wall. To separate masses of the fission fragments with a flight-path of 7 m, a challenging resolution of 35 ps (standard deviation) is required [Bai10]. In order to give a precise measurement of the particle's curvature and velocity, the tracking will be made using two Multi-Wire Proportional Counters (MWPC) with excellent resolution, and using the position inside the double ionization chamber given by the segmented anodes and the drift-time of the ionized electrons. The neutron multiplicity will be

measured with the LAND neutron wall [Bla92].

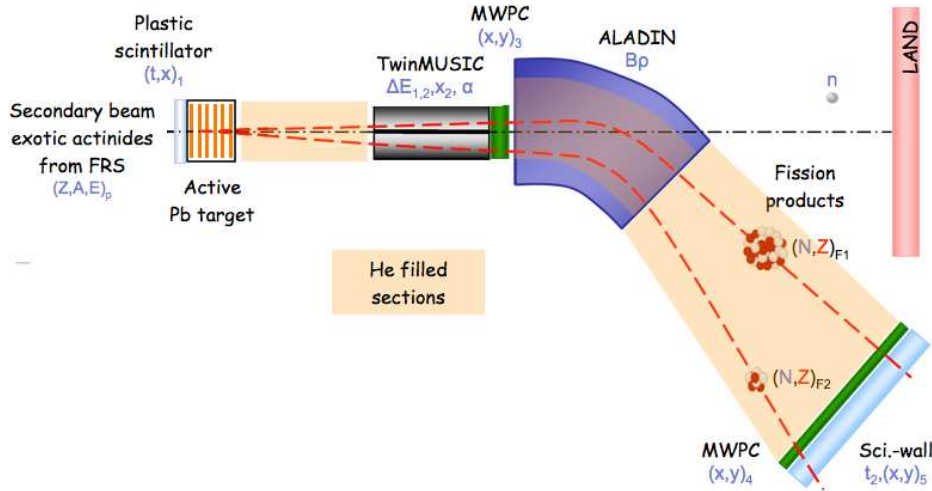


Figure 4.1: Experimental setup for SOFIA experiment. Figure taken from [Bai10].

4.1.2. R³B

The R³B (Reactions with Relativistic Radioactive Beams) [R3B] experiment will be part of the forthcoming FAIR international accelerator facility (Facility for Antiproton and Ion Research) [FAI] to be built at GSI. The experiment will cover experimental reactions with exotic nuclei far from stability providing unique experimental conditions worldwide. The current GSI installations will be utilized as pre-accelerator of the new SIS100/300 double superconducting synchrotron that will provide ions and antiproton beams with unprecedented characteristics. Intensities of the order of 10^{12} ions per second and higher than 10^5 ions per second will be achieved for primary* and rare isotope secondary beams, respectively. These secondary beams will be produced in the Super-FRS [Gei03] (Superconducting FRagment Separator) and delivered to other experimental areas. The R³B experiment, located at the focal plane of the high-energy branch of Super-FRS, is a future experimental setup aiming at the complete measurement and reconstruction of

*Elements up to uranium will be accelerated with an energy up to 1.5 A GeV.

nuclear reactions in inverse kinematics with beams, both stable and radioactive, at high energy. A wide-ranging and outstanding scientific program, investigating nuclear structure and dynamics via knockout, quasi-free scattering, charge-exchange or fission reactions among others, will be carried out using the R^3B versatile setup (see Fig. 4.2 for an schematic drawing) which is based on the present ALADIN/LAND reaction setup introducing a substantial technological improvement. Therefore, state-of-the-art detectors with high efficiency, acceptance and resolution are required.

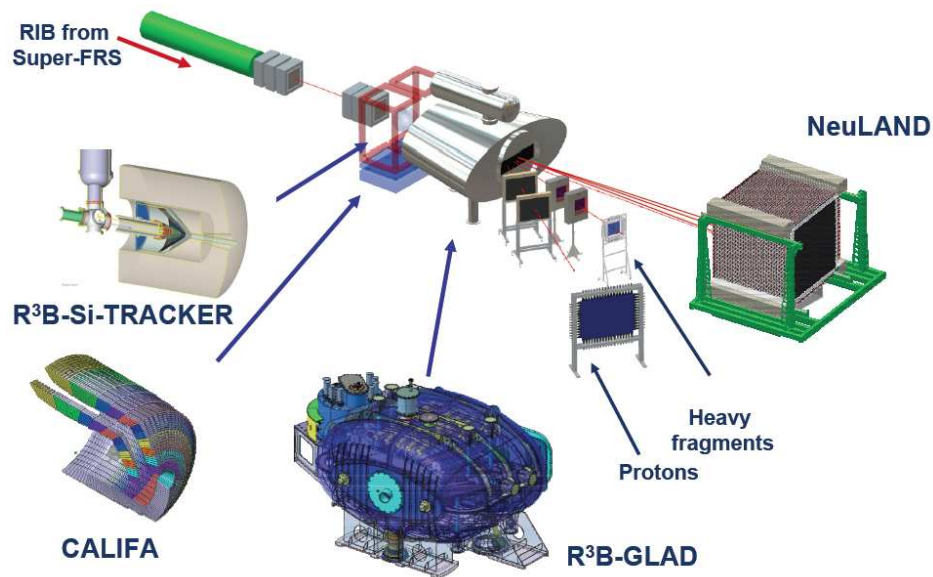


Figure 4.2: Conceptual drawing of the R^3B experimental setup. Figure taken from [R3B].

The main detector system of R^3B will consist of a large acceptance dipole (GLAD) with around 5 Tm of integral field, heavy-ion silicon tracker detectors, a large-area time-of-flight wall for fission and spallation measurements, a total γ -absorption calorimeter (CALIFA) and a high resolution neutron time-of-flight spectrometer (NeuLAND). Fission experiments will follow a configuration similar to that of the SOFIA experiment using these detectors and benefiting from the large acceptance and bending power of the GLAD dipole. The technological improvement of the R^3B setup will allow the limits of our knowledge of the dynamics of the fission process and structure effects to be greatly extended.

4.1.3. FELISE

Also within the FAIR facility, FELISE (Fission at ELection-Ion Scattering experiment) will investigate the fission process in exotic heavy ions induced by electrons. The heavy ions will be produced at the Super-FRS, similarly to R³B experiment and the electrons will be accelerated up to 500 MeV by the Electron Linear Accelerator and the Electron Antiproton Ring accelerator. Both will be injected in the New Experimental Storage Ring (NESR) where the reaction will take place.

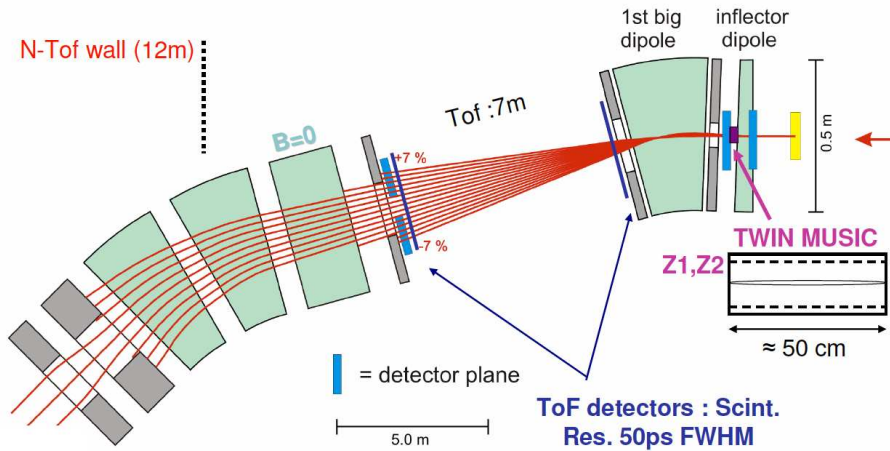


Figure 4.3: FELISE experimental setup. Figure taken from [Bai10].

The detection setup for fission experiments (see Fig. 4.3) will include a double ionization chamber to identify in charge both fission fragments, a time-of-flight wall and a big dipole to measure the mass with the $\beta\rho$ method and three tracking detectors to measure the position of the fragments. The determination of the excitation energy of the fissioning nuclei by measuring the energy of the scattered electron in an electron recoil spectrometer will constitute a substantial improvement with respect to previous experiments.

4.2. Requirements of the ToF wall of the R³B ToF wall (iToF)

Since the main purpose of the ToF wall of the R³B experiment (hereafter iToF, ion Time-of-Flight wall) is the detection and time-of-flight measurement of relativistic ions produced in fragmentation, fission and also multi-fragmentation reactions, several parameters must be fixed to establish the

conceptual design of such a detector. The mass resolution depends on the length of the flight-path, defined as the distance from the reaction vertex to the iToF. Hence, the dimensions of the detection plane are constrained by the flight-path.

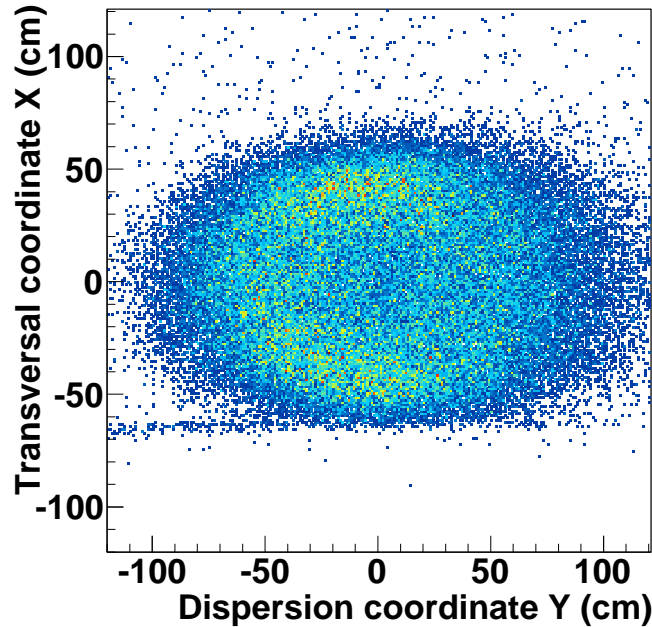


Figure 4.4: Spatial distribution of the fission residues produced in the reaction $^{208}\text{Pb} + ^{238}\text{U}$ in the iToF detection plane.

If we want to isotopically separate masses of fission fragments ($A < 150$) a time resolution of around 50 ps (standard deviation) is required for a flight-path of 15 m. In the case of fragmentation of ^{208}Pb or ^{238}U at 400 A MeV, typically used to produce very neutron-rich and neutron-deficient species far from stability, the time resolution needed for the same flight path is around 30 ps (standard deviation) for fragments with masses around $A=200$, but the angular aperture is smaller. Fission of ^{238}U or ^{208}Pb at 400 A MeV is a benchmark case, since it represents the lowest energy of interest in R^3B and also the highest angular aperture of the fragments distribution. A simulation of the experimental scheme of the R^3B setup performed with GEANT4 transport code provides the geometry and distribution of the products of the reaction. In order to do this, we considered a ^{208}Pb beam impinging onto a ^{238}U target at 400 A MeV of energy. The kinematics of the reaction products

were determined with INCL4.6+ABLA codes. Then, in GEANT4 the reaction vertex was placed before the large acceptance dipole (GLAD) and the particles of interest were transported and deflected towards the iToF taking into account their masses and energies. Considering a flight-path of 15 m, the angular aperture in the detection plane is 1 m in the vertical direction, and due to the dispersion introduced by the dipole, the aperture covers up to 2 m in the horizontal direction (see Fig. 4.4).

iToF could be adapted in each case to provide a better time resolution according to the reaction to be measured. This can be achieved either by increasing the number of detection planes, n (improving the measurement by a factor \sqrt{n}) or by increasing the flight-path. Moreover, beyond fission and fragmentation, the detector could be adapted to reactions where light nuclei and charged particles are produced. These requirements show clearly that the detector has to cover a broad range of nuclei with different nuclear charges and therefore accommodate a huge dynamic range. A flexible and modular design for the iToF is proposed to adapt the surface and the number of planes to each specific case.

The multi-hit capabilities of the detector are designed according to the particle multiplicities of the reaction mechanisms of interest. Medium-mass residues produced in fission reactions are accompanied mostly by neutrons, while heavy-mass residues are produced together with protons, neutrons, alpha particles and light-mass nuclei. Therefore, as can be seen in Fig. 4.5, each detection plane will be divided in several independent modules segmented in strips covering a surface of 1 m and 2 m in the vertical and horizontal coordinates, respectively [AP06; Cas12a]. The granularity of the detector will be improved by crossing 90° each detection plane as represented in Fig. 4.5. The foreseen reaction rates of the R³B experimental programs will be around a few hundred reactions per second in the cases of interest, at the limit. Thus, the expected rates per surface unit in the case of fission will be limited to several ions/cm² per second considering multiplicities below 10 and the surface of the detector. In addition, the detector also has to deal with the high rates of the beam particles impinging in a reduced area of few mm². With this geometry, the multi-hit capabilities of the detector will be fulfilled.

Since the angular straggling after several meters of flight is a non-negligible quantity, the impact point position has to be determined to correct the length of the flight-path, and to accurately define the velocity required for identification. Due to the relative orientation between consecutive detection planes, the position resolution in the dispersion and transversal coordinates will be given by the time difference between the signals measured in both extremes of the strip where the particle impinged.

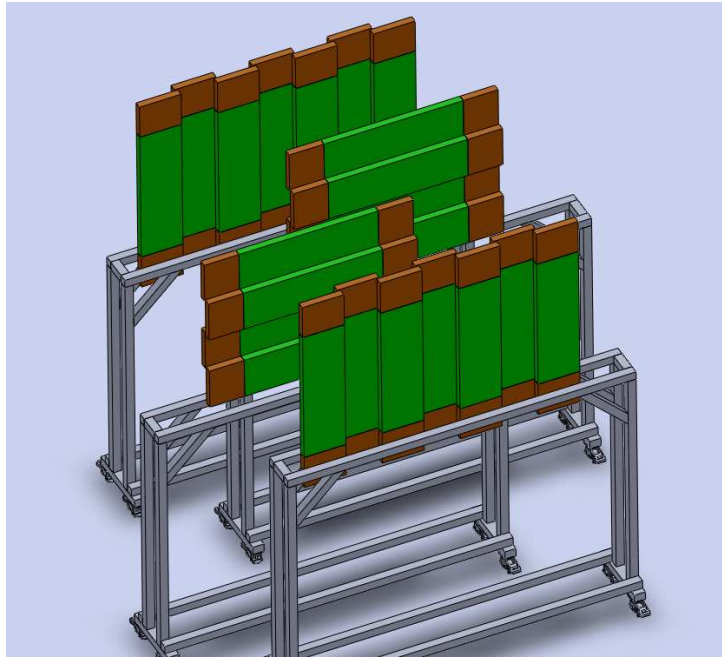


Figure 4.5: Conceptual design of the iTof.

4.3. ToF detectors

The measurement of the time-of-flight of the particles in high-energy and nuclear physics experiments is commonly performed using fast detectors capable of time resolutions better than hundreds of picoseconds. Two different technologies are discussed in this section: organic scintillators coupled to fast photomultipliers (PMTs) and RPCs. Here, we will discuss their general features and their performances for ToF measurements.

4.3.1. Scintillation detectors

There exist many types of scintillator materials with different characteristics suitable for a wide range of applications. The choice of a proper scintillator is a compromise between several parameters, such as scintillation efficiency, linearity in light conversion, decay time, optical quality, transparency to the wavelength of emission and the index of refraction. Scintillators can be classified basically in two groups: inorganic crystals and organic (plastic and liquid) scintillators. The former are excellent for γ spectroscopy due to a high density resulting in a high stopping power and excellent linearity in the conversion of deposited energy into light, although their responses and decay

times are slower. For timing measurements organic plastic scintillators coupled to fast PMTs are the most used detectors owing to their time resolution, fast recovery and the possibility to manufacture the material into large-size structures such as time-of-flight walls. There exist several large-area scintillator walls installed in high energy physics experiments such as HADES at GSI with a time resolution of about 100 ps (standard deviation) and the ToF wall of the HARP experiment with 160 ps of time resolution. Moreover, a scintillator-based ToF wall with an expected resolution of around 100 ps is proposed for the forthcoming PANDA experiment at GSI[Bus05].

4.3.1.1. Organic scintillators

A particle crossing an organic scintillator deposits part of its kinetic energy ionizing the molecules and exciting the electrons and the vibrational states near the electronic ground state. The scintillation light yielded in the transitions made by free valence electrons of the molecules has a transparent wavelength with respect to the medium due to the energy shift caused by vibrational quanta (Stokes shift). The scintillation efficiency corresponds to the fraction of the deposited energy converted into light and depends on how many light-emitting de-excitation modes are available. The scintillator is optically coupled to a fast PMT with a spectral response in the range of the wavelength of the emitted light. The light is guided to the photomultiplier and converted into photoelectrons that are accelerated and amplified in the dynodes creating a cascade of secondary electrons which is collected at the anode, forming the fast pulse signal. In most organic scintillators, the fluorescent light has a decay time τ of around a few ns and the prompt fluorescence intensity is given by:

$$I = I_0 \exp(-t/\tau) \quad (4.2)$$

This also makes the use of organic scintillators suitable for timing applications in high counting rate environments. It is also known that the time resolution strongly depends on the number of photons emitted [Nis03] according to $\sigma \propto N_p^{-0.5}$, where N_p is the number of photoelectrons. Therefore, the time resolution improves as the number of photoelectrons increase. The time resolution also depends on the efficiency propagation of the light inside the scintillator, and thus, on its size.

4.3.1.2. Performance with heavy ions

Organic scintillators provide excellent time resolutions when measuring relativistic heavy ions due to their large energy deposition and photon emis-

sion which is enhanced for thicker devices. However, there exists a compromise between the thickness of the scintillator and the induced energy straggling that should be taken into account. There have been reported resolutions below 10 ps (standard deviation) for a BICRON BC422Q scintillator of 110 ps of rise time, 50 mm length and 0.5 mm thickness coupled to Hamamatsu R4998 PMTs (0.7 ns) irradiated by a ^{40}Ar beam at 95 MeV/u [Nis03]. In this experiment, two leading-edge discriminators, Kaizu and Phillips Discriminator 630 were used to discriminate and reshape the signals. A Kaizu TDC-3781 (Time-to-Digital Converter) digitized the timing signals. The FRS at GSI is equipped with BC420 fast plastic scintillators of 20 cm length and 5 mm thickness coupled to Hamamatsu R2083 PMTs achieving 150 ps (FWHM) of resolution with fast heavy ions [P10]. The current research in fast organic scintillator technology for future nuclear physics experiments where a ToF wall is needed, such as SOFIA (see section 4.1.1), has achieved very promising time resolutions of about 35 ps (FWHM) with a 300 and 600 mm length scintillators of 1 mm thickness (EJ-232) and a rise time below 100 ps, coupled to fast Hamamatsu H6533 PMTs (0.7 ns of rise time) and irradiated by a ^{56}Fe beam of 350 A MeV [Bai10]. The signals were discriminated with an ultra-fast CFD (Constant Fraction Discriminator) developed by Phillips Scientific and the time-of-flight measurement was done with an ORTEC 566 TAC (Time-to-Amplitude Converter). Concerning larger sizes, scintillator-based ToF walls of around 1 m² of area with time resolutions well below 200 ps (standard deviation) have been already implemented in nuclear physics experiments [LAN; Sch00] to measure the charge and velocity of residues produced in reactions employing relativistic heavy-ion beams.

4.3.2. Resistive Plate Chambers

RPCs are gaseous detectors consisting of resistive parallel plates with plane electrodes defining a small gap filled with a proper gas mixture and a high electric field across it. Several large-scale high-energy physics experiments worldwide such as ATLAS [Aie04] and CMS [Abb98] at CERN utilize RPCs as muon trigger with about 1 ns of time resolution and high detection efficiency. Versions of RPC with hundred of μm gas gaps are also used as fast timing detectors (tRPCs) with resolutions better than 100 ps standard deviation in experiments such as HARP [Amm07] and ALICE [Aki09] at CERN, FOPI [Kis11] and HADES [Bla09] at GSI and STAR [Wan10] at BNL. All these experiments use RPCs developed to detect minimum ionizing particles (MIPs) and after years of intense R&D, the proper working parameters regarding gas mixture, field intensity and irradiation rates have been well established.

4.3.2.1. Working principles of the RPCs

The first RPCs were designed by R. Santonico and R. Cardarelli in 1981 [San81; Car88]. RPCs consist of two parallel plate electrodes defining a gap between them, with at least one of the electrodes made of a high resistivity material of around $10^{12} \Omega m$ (see Fig. 4.6). The gap, whose size may range from hundreds of μm up to a few mm, is filled with a highly quenching gas mixture consisting of sulfur hexafluoride (SF_6), used as dielectric gas to control the formation of the avalanche, isobutane (iso- C_4H_{10}) for quenching the UV photons released in the non-ionizing excitation of the molecules, and tetrafluoroethane ($C_2H_2F_4$) as a self-quenching ionization medium. The working principle is that of a gas ionization chamber operated with a high uniform electric field across the gap with typical values of 100 kV/cm for 300 μm gap. The charge carriers released in the ionization of a particle crossing the detector are drifted towards the cathode and the anode. Electrons which are accelerated due to the high electric field of the RPC acquiring a large kinetic energy, can ionize the gas molecules producing secondary electrons which are propagated and multiplied forming a Townsend avalanche where the number of total electrons n created along a mean path x is given by the following expression:

$$n = n_0 \exp(\alpha x) \quad (4.3)$$

α being the first Townsend coefficient and n_0 the initial number of electrons. The signal induced by the avalanche is read out from strips placed in the electrodes. The resistivity of the layers is a key parameter that determines the time response of the detector. The charge collected in the resistive electrode exponentially decays according to:

$$Q(t) = Q_0 e^{-t/\tau} \quad (4.4)$$

with $\tau = \rho \varepsilon_0 \varepsilon_r$, where ρ is the resistivity of the material, ε_0 is the dielectric constant and ε_r is the permittivity of the material. Therefore, low values of the resistivity lead to shorter relaxation times τ . A glass resistivity of $\rho = 10^{12} \Omega m$ lead to a relaxation time τ of around 1 s [Lip03]. For a resistivity of the order of $\rho = 10^{10} \Omega m$, a relaxation time of the order of μs is obtained. Owing to the charge carriers in the resistive electrode, the electric field is locally reduced and thus the detector is inhibited during a time of the order of τ , around the spatial point where the avalanche was formed. The electric field is also affected during the progress of the avalanche that creates a space charge effect. If the voltage is increased, photons may contribute to the avalanche formation increasing it, and, may lead to the creation of

pulses with much higher charge called streamers. For even higher voltages, a conductive channel may be created between both resistive electrodes leading to a local discharge with the possibility of spark formation. According to this, RPCs can operate in either two different regimes, avalanche or streamer modes.

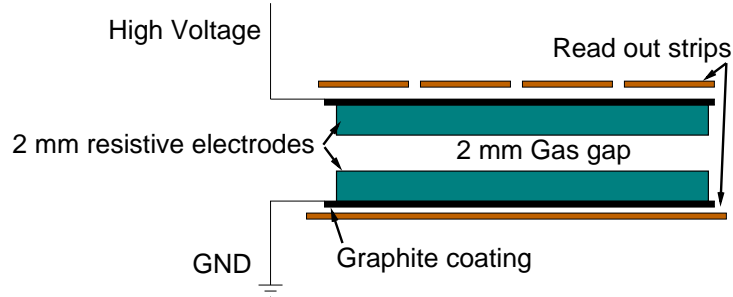


Figure 4.6: Schematic drawing of a 2 mm gap RPC. Conceptual design taken from [San81; Car88].

4.3.2.2. Avalanche RPCs

The avalanche working mode is preferred for timing purposes. The average charge of an avalanche pulse is smaller than that of a streamer pulse, thus its counting rate capability is improved (1 KHz/cm² for MIPs) because the detector needs less time to recover. Furthermore, the presence of streamer pulses may deteriorate the time resolution due to the precursor pulse that often accompanies it. Besides the resistivity of the electrode material, there exist other factors to take into account in order to control the streamer production. The usual gas mixture, containing a small amount of SF₆ which is an excellent electronic quencher, and the applied high voltage are critical parameters concerning the streamer production.

While RPCs deployed in large-area experiments to trigger MIPs, usually consist of one gas-gap of around 2 mm of thickness with electric fields of the order of 50 kV/cm and time resolutions of around 1 ns, narrow gap RPCs (tRPC) are assembled in narrow multi-gap (200-300 μm) structures [Zeb96; Fon00], as shown in Fig 4.7, improving its individual detection efficiency according to $\epsilon = 1 - (1 - \epsilon_g)^n$, where n and ϵ_g are the number of gaps and its efficiency, respectively. Efficiencies of 90%-94% have been attained with these tRPCs (4 gaps) measuring MIPs [Fon02]. Considering independent measurements in each gap, the time resolution is improved following:

$$\sigma = \frac{\sigma_n}{\sqrt{n}} \quad (4.5)$$

tRPCs operated at about 100 kV/cm of electric field yield time resolutions around 45 ps (standard deviation) for MIPs for a 6 gap tRPC [Amm10]. Due to the low average charge of avalanche pulses, the use of low-noise high-frequency front-end electronics is compulsory to preserve the timing properties of the tRPCs. This is also necessary in order to discriminate the avalanche precursor of the streamer pulses. In the present work we will focus on the study of tRPCs for the detection of fast ions.

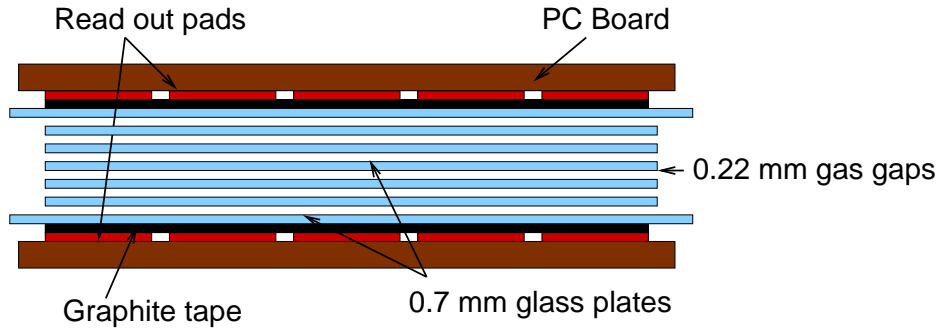


Figure 4.7: Schematic drawing of a multi-gap tRPC.

4.3.2.3. Streamer RPCs

In applications and experiments where the counting rate and timing capabilities do not represent a limiting factor, the use of the streamer mode really simplifies the read out of the pulse and therefore preamplifiers are not needed. These RPCs are commonly used as trigger system of large experiments or with counting purposes. With high electric fields of around 40 kV/cm, streamer mode bakelite RPCs reach around 99% of efficiency with MIPs but with relatively low counting rate capability (few hundreds Hz/cm²). Experiments such as BABAR at SLAC [Zal00], OPERA at LNGS [Dus01] or ARGO at YangBaJing [Bac00] use detection systems based on streamer mode RPCs.

4.4. Detection of relativistic heavy ions with RPCs

Owing to their excellent timing properties, it has been recently proposed the use of RPCs as an option for the construction of the ion time-of-flight wall (iToF) for the R³B experiment (see section 4.1.2). The use of RPCs for the detection of relativistic heavy ions, and the information concerning

the performance under such conditions is scarce [Cas12b; Cab09]. The much larger energy deposition of relativistic highly charged ions with respect to MIPs and the rate capabilities are key parameters that must be investigated in order to find a proper working point to preserve the outstanding properties of the tRPCs. Thus, we started few years ago a dedicated R&D program in order to construct and characterize tRPC prototypes designed to detect heavy ions.

The aim of this section is to study the performance of these prototypes under relativistic ion irradiation. We will describe the construction of the tRPCs and the different analog front-end electronics developed for these prototypes. This section is also dedicated to describing the performance of tRPC prototypes studied in several detector tests with heavy-ion and electron beams: detection efficiency and time resolution varying different parameters such as gap voltage or gas mixture. The degradation of the time resolution with the irradiation rate is also another key point that will be studied further in this chapter. For this purpose we used a dedicated data acquisition system of which the features and characteristics are also explained in this section.

4.4.1. Development and construction of tRPC prototypes

The prototypes constructed and tested in this work were designed to the detection of heavy ions at relativistic energies. One of the most relevant issues when detecting heavy ions is the energy loss of the particles in any layer of matter that may cause ions to be stopped before passing through the detector. Taking into account the range of ^{238}U or ^{208}Pb ions at 400 A MeV in soda-lime glass is about 15 mm **, every detector was designed with the minimum amount of matter possible in its active detection area. For this reason, the prototypes were built using glass plates of 1 mm thickness. Moreover, taking into account a possible configuration of the iToF in several detection planes, one has to consider the energy and angular straggling induced by the layers of matter. In time resolution terms, this straggling induces a broadening of the time distribution, and therefore it degrades the measurement. For instance, the angular straggling induced to a ^{238}U ion at 400 A MeV after crossing 2 mm of soda-lime glass is around 0.5 mrad.

The first small prototype (hereafter RPC-11) was designed as a symmetric double gas-gap structure using four soda-lime glass plates of $6 \pm 2 \times 10^{12} \Omega\text{m}$ of resistivity, and, 15 cm \times 7 cm of area (see upper panel of Fig. 4.8). Nylon

**The composition of the soda-lime glass is 74% of SiO_2 , 13% of Na_2O , 10.5% of CaO and 1.3% Al_2O_3 .

fishing line of $300\ \mu\text{m}$ was used as a spacer to create the gas-gap. This gap size is the same for all prototypes studied in this work. Two strips, made of self-adhesive copper tape of 150 mm length, 20 mm width and 2 mm pitch, were situated in each one of the three planes defined by the glass stack assembly acting as electrodes and signal pick-up. The stack was placed in between two G10 plates of 2 mm thickness to pack the plates and provide the assembly an additional rigidity. The high voltage was supplied via the middle electrode while the external ones acted as the ground reference. The signal was read from both edges of the external electrodes, previously decoupled from the high voltage. During the measurements only one of the strips was active and the prototypes were placed inside an aluminum box to ensure the gas tightness keeping a gas flow of $100\ \text{cm}^3/\text{min}$ (around 5 l/h). We also constructed a single gas-gap version of the RPC-11 prototype (RPC-22).

A more optimized small prototype for timing measurements (RPC-25) was constructed by using two one-strip aligned RPC modules with same characteristics as RPC-11, separated by a few cm as shown in the lower panel of Fig. 4.8. The construction of each individual assembly was identical to the previous prototypes, however here the G10 plates were removed and the glass plates were glued to pack the glass plates and two thin Kapton windows were placed in the gas-tight aluminum box to reduce the amount of layers of matter the energy losses and the energy and angular straggling.

Going a step further in the design, a large-area prototype (RPC-30) was constructed with only one gap defined by a self-tight soda-lime glass structure (see Fig. 4.9). This self-contained multi-strip tRPC of $40\ \text{cm} \times 20\ \text{cm}$ was assembled with two soda-lime glass plates, glued around the edges to seal the gas-gap and ensure its tightness. Only two regions of a few mm were kept unsealed to allow the gas flow. The 5 strips of 20 mm width that define the active detection area were made of self-adhesive copper tape, glued to the external side of each plate. The induced signals were read out from both ends of each strip. The HV was distributed to the copper strips in one of the plates of the module while the other plate was the ground reference. This one-gap structure represents an ideal option for the construction of the real-size iToF modules owing to the compromise between thickness (1 mm) and robustness of the glass plates. Furthermore, the total gas volume per module is drastically reduced corresponding to the active detection volume (about $100\ \text{cm}^3$). Two single-gap self-contained structures were stacked and placed in an aluminum structure making the strips coincide to perform time measurements between them (see Fig. 4.10). In addition, a single-strip version of this prototype was constructed (RPC-40) with two one-gap structures of $40\ \text{cm} \times 7\ \text{cm}$ constructed with soda-lime glass plates. In both structures, the two RPCs were separated by 5 cm.

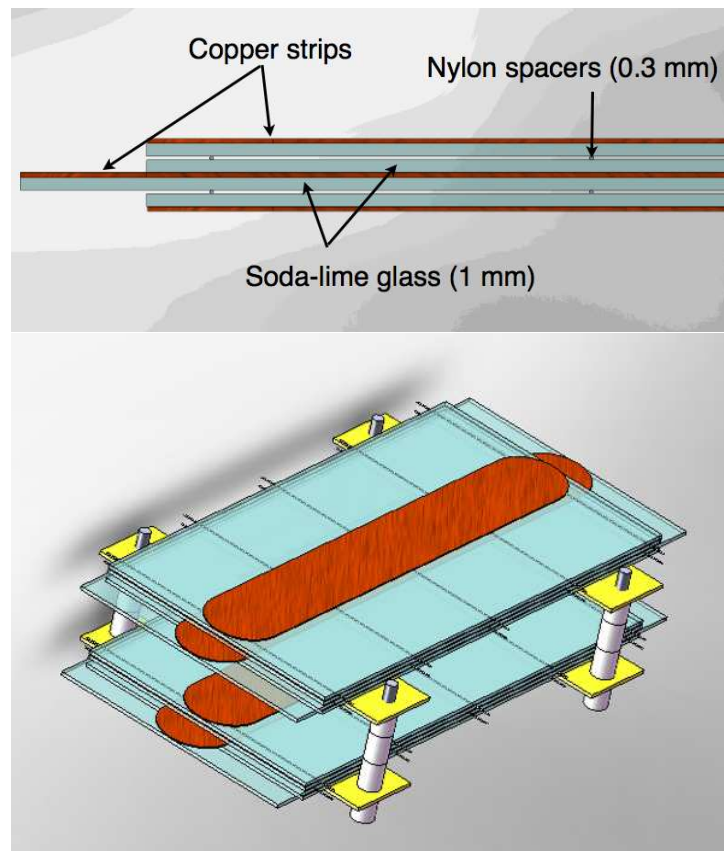


Figure 4.8: Upper panel: Lateral view of the schematic representation of a small double gas-gap prototype. Lower panel: Top view of two double gas-gap prototypes with a single strip (RPC-11).

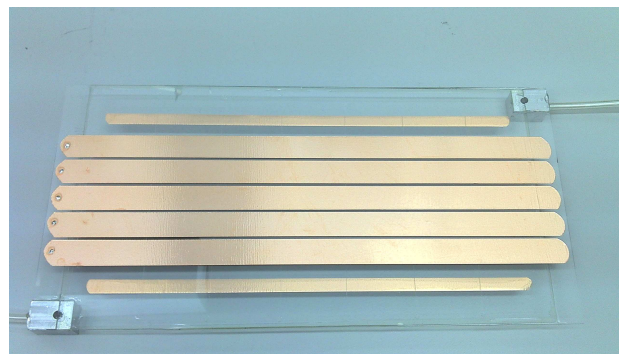


Figure 4.9: Single-gap self-contained multi-strip tRPC (RPC-30). The gas mixture is supplied via both rectangular aluminum pieces.

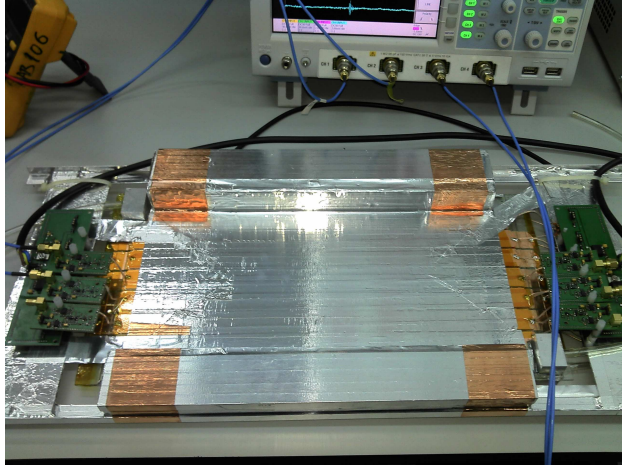


Figure 4.10: Two identical RPC structures shown in Fig. 4.9 assembled in an aluminum support (RPC-30).

4.4.2. Analog front-end electronics (FEE)

The development of an appropriate amplification stage capable of dealing with the high-frequency bandwidth signals produced by the tRPCs (GHz) is a key parameter in order to obtain high-quality timing measurements. Also, the gain has to be adapted to the relatively low charge of the avalanche pulses and the wide nuclear charge range of the ions we want to detect. The quality and behaviour of the electronic components and its complex impedance in the bandwidth range of interest is also another critical issue that complicates the design of the front-end electronics (FEE).

The signal induced in the strip is decoupled from the HV and fed the FEE board. A RCL filter is implemented in order to dump the highest frequencies down to hundreds of MHz to accommodate the signal to the amplifying stage (around 1 GHz) and match the impedance between the latter and the strip. For the amplifying stage we implemented different solutions that we tested with the different prototypes. For the double-strip double-gap prototypes (RPC-11 and RPC-22) we used two commercial trans-impedance amplifiers in cascade: GALI-S66 and MAXIM-4223 having a bandwidth up to 1 GHz. The rise time of the amplified output signals was about 12 ns and the noise level was below 20 mV. Since the RPC-25 prototype was optimized for time resolution measurements, the amplifier stage was designed in order to reduce the rise time of the signal and adapt it to our specific data acquisition system for timing purposes. For this prototype we used a commercial wide-band transistor BFR92A (5 GHz) and MAXIM-4224 current amplifier. The signals amplified by this FEE had a rise time of around 4 ns and a noise level below

10 mV. In all these prototypes, the output signals were transmitted using LEMO-00 coaxial cables having 50Ω of impedance.

The RPC-30 and RPC-40 prototypes were equipped with a slightly different FEE card. To improve the signal-to-noise ratio the MAXIM-4224 chip was replaced by the OPA657 trans-impedance amplifier with 1.6 GHz bandwidth and a gain up to 44 dB. The output signal, reaching a noise level below 5 mV and a rise time of 4 ns, was transmitted using a specific semi-rigid coaxial cable with SMA (SubMiniature version A) connectors featuring up to 3 GHz of bandwidth and 50Ω of impedance. The selection of an electronic system (including the cable type) was proposed to preserve the quality of the signal and its timing properties as well as to adapt its amplitude and width to our acquisition system input; to be explained in section 4.4.3.

4.4.2.1. FEE calibration

The charge output of the FEE is a key parameter that is commonly used to correct the time-walk (slewing) effect on time-of-flight measurements. Time-walk arises from the variation in the height of the pulses and it is especially critical for small charge signals. Therefore, a charge calibration is mandatory in order to establish the response and limits of our FEE. The charge and amplitude calibration was done feeding the card with a fast pulse (generated by an Agilent 81110A pulse generator) of variable amplitude (from 10 up to 300 mV) and width (from 4 up to 13 ns) and a rise time of around 2.5 ns (400 MHz). These fast signals were constructed using a passive differentiator circuit connected at the output of a square-pulse generator. An oscilloscope (Yokogawa DLM6000) with a bandwidth of 1 GHz and a sampling speed of 5 Gs/s was used to digitize the full pulse (see Fig. 4.11).

The amplitude and charge calibration curves of the RPC-30 prototype FEE consisting of a BFR92A+OPA657 are shown in Figs. 4.12 and 4.13, respectively. One can see that the FEE input and output amplitudes show a linear correlation from 10 up to 60 mV with a gain factor of about 5.5 (slope). The FEE starts to saturate at around 100 mV of input amplitude and the gain factor is progressively reduced down to 2.2 at 650 mV. Concerning the charge calibration, a linear correlation was found in the range from 0 to 16 pC of input charge with a gain factor of around 4. However, the entire range (from 0 to 150 pC) could be fitted to a second order polynomial function.

Similarly, we also calibrated the FEE installed in the RPC-25 prototype (BFR92A+MAXIM-4224) using the same procedure as explained before. The amplitude calibration curve of this FEE represented in Fig. 4.14 shows a correlation between the input and output amplitudes with a gain factor of around 20. Compared to the BFR92A+OPA657 FEE, the satura-

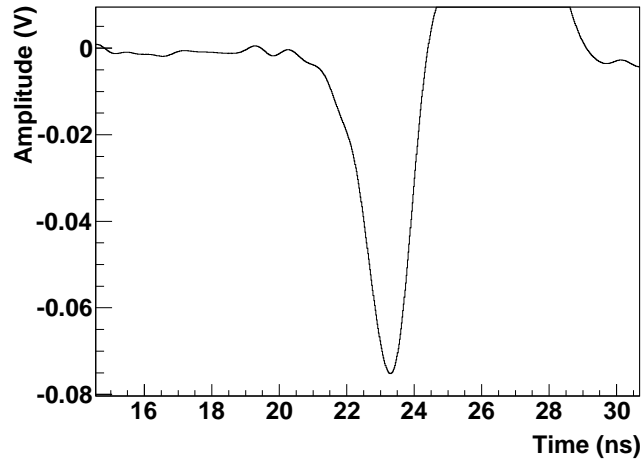


Figure 4.11: FEE calibration pulse digitized in the oscilloscope.

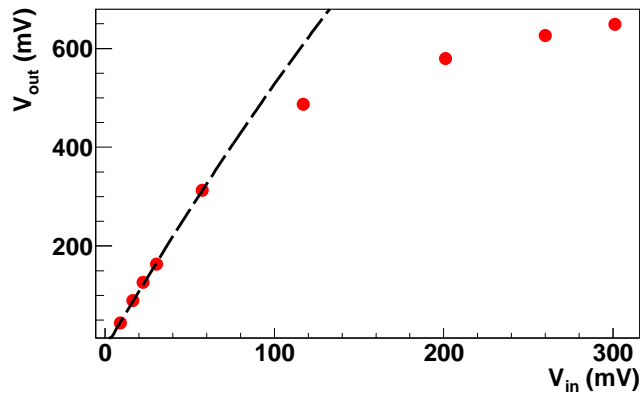


Figure 4.12: BFR92A+OPA657 FEE amplitude calibration curve (See text for details).

tion effect seems to be smoother and the curve could be fitted to a second order function over the entire range. The slight change in the slope of the amplitude curve around $V_{in} = 40 \text{ mV}$ is an artifact caused by the change of the voltage range of the pulse generator. On the other hand, a linear correlation with a gain factor of about 22 was found between the charge of the same input signals and the output signal (see Fig. 4.15).

In conclusion, this characterization of the response of the FEE will allow us to extract quantitative results of the measurements and compare prototypes with different FEE boards. The quality of each FEE has to be deter-

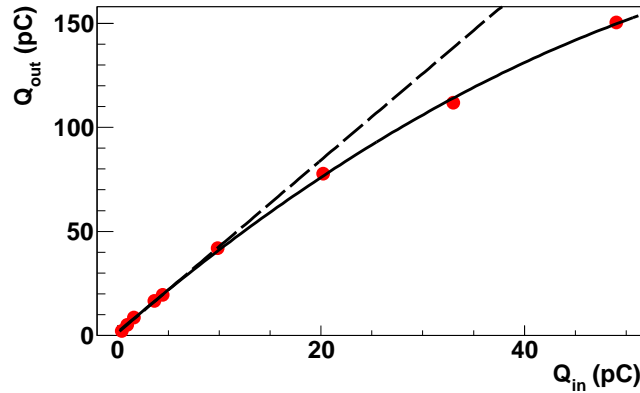


Figure 4.13: Same as Fig. 4.12 but for charge.

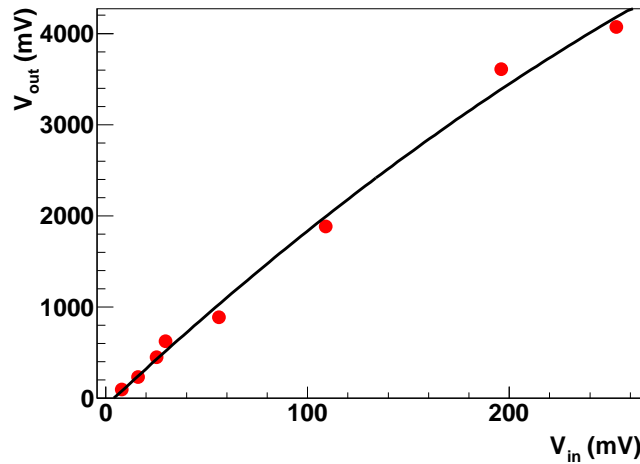


Figure 4.14: BFR92A+MAXIM-4224FEE amplitude calibration curve (See text for details).

mined by testing its performance under the detection of relativistic heavy ions.

4.4.3. Experimental setups

Since the experimental tests were done bombarding the prototypes with heavy ions at relativistic energies, the determination of the performance of the tRPCs and its characterization requires a capable trigger system with high efficiency for the detection of heavy ions to unambiguously identify

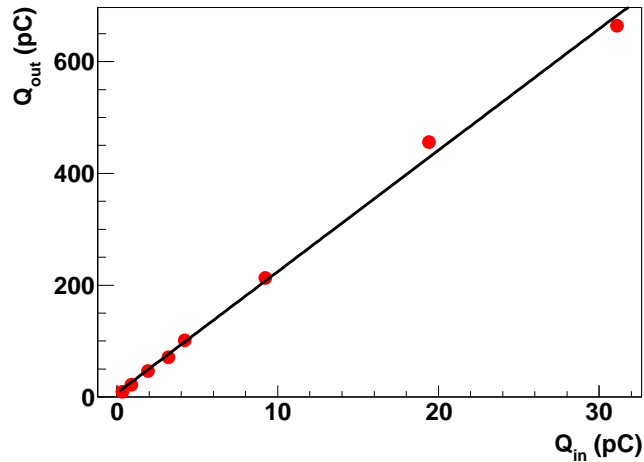


Figure 4.15: Same as Fig. 4.14 but for charge.

particles traversing the detector. First we used BICRON BC420 plastic scintillators of $120 \text{ mm} \times 20 \text{ mm}$ and 10 mm thickness, later replaced by EJ-232 (Eljen Technology) scintillators, these had better timing properties, having a rise time well below 100 ps and dimensions of $140 \text{ mm} \times 30 \text{ mm}$ and 1 mm thickness. These scintillators were used for an external trigger system to determine the intrinsic detection efficiency and time resolution of the tRPCs prototypes. The scintillator paddles were coupled to two fast Hamamatsu H6533 PMTs, with 0.7 ns of rise time, providing signals from both ends of the paddles. The trigger system scheme and the layout of the scintillators and the tRPC are shown in the upper and lower panels of Fig. 4.16. During the tests, the tRPC prototypes were placed in the beam line together with one or two plastic scintillator detectors and the trigger was given by the signals of the four photomultipliers in temporal coincidence after being discriminated. Therefore, a beam particle traversing the scintillators and the tRPC was identified and clearly separated from the noise signals. To reduce systematic uncertainties associated to the setup geometry, the transversal dimension of the trigger detector was aligned to the active strip of the prototypes (20 mm).

4.4.4. Data acquisition systems

The data acquisition systems we have used to digitize and analyze the signal pulses of the tRPCs were based on the standard VME bus. The hardware control was made by means of a CES RIO3 processor and a TRIVA module used to control the dead-time of the acquisition. The triggers given by the

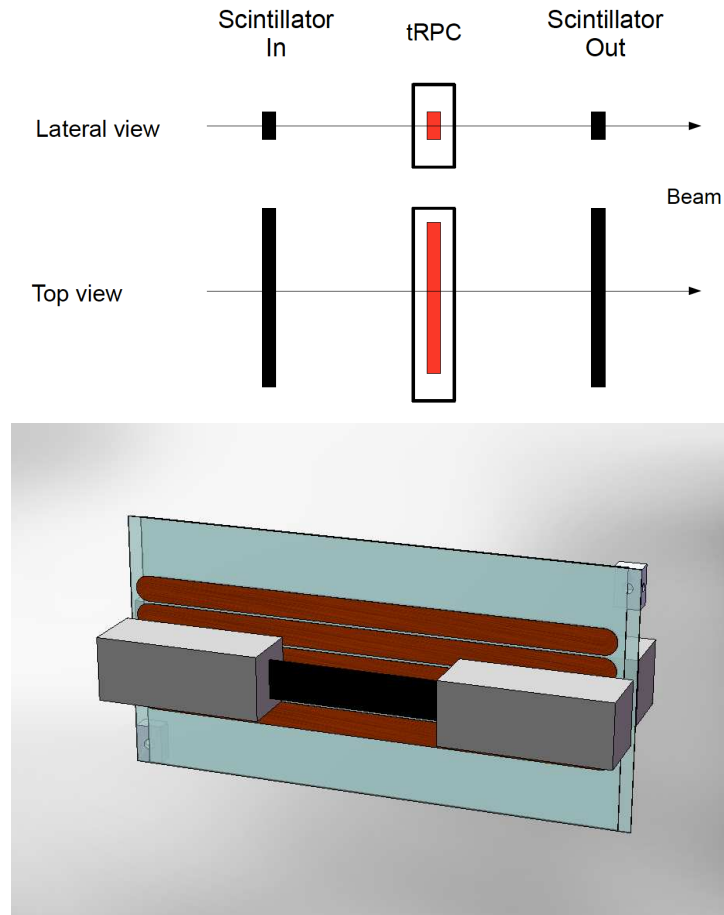


Figure 4.16: Upper panel: Scheme of the scintillator-based external trigger for efficiency and timing measurements. Lower panel: Layout of the tRPC placed in between two scintillation detectors.

coincidence of the four signals of the PMTs, were obtained using standard NIM electronic modules (Fan-In Fan-Out, leading-edge discriminator, octal gate generator and coincidence module). A trigger is accepted if the system is not blocked by the dead time. These triggers are provided to the TRIVA module, allowing read out of the data, controlled by the MBS (Multi-Branch System) software. To fully digitize the signals coming from the PMTs and the FEE of the tRPCs we used VME flash-ADC (fADC) boards based on the MATAcq32 chip with 2 GS of sampling speed and 300 MHz of bandwidth developed by M2J [M2J]. The digitization of the pulse allowed us to investigate the signal formation in the tRPC and study its characteristics. The efficiency and streamer production was determined by means of a com-

prehensive pulse shape analysis. However, the time resolution of this system is limited to 500 ps by the sampling speed of the flash-ADC modules and the acquisition rate is restricted to a few tens of Hz. A scheme of this system is presented in Fig. 4.17 and the shape of a pulse of the BFR92A+OPA FEE registered by the fADC is shown in Fig. 4.18.

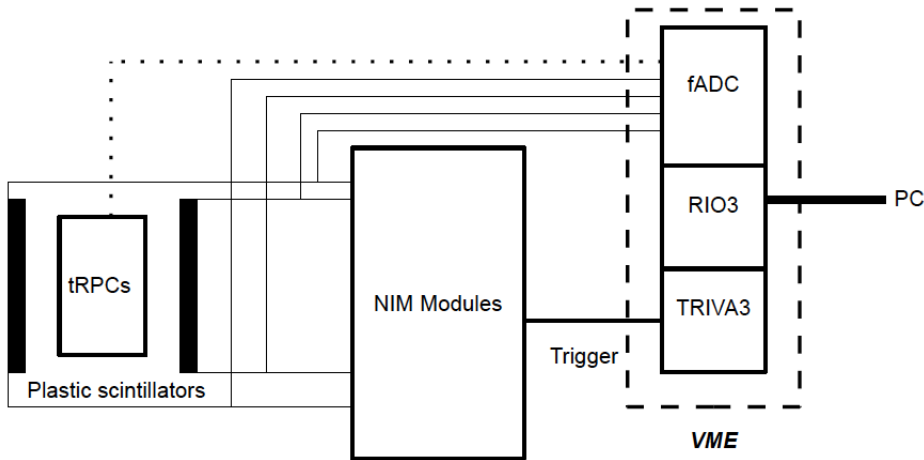


Figure 4.17: Scheme of the fADC-based data acquisition system.

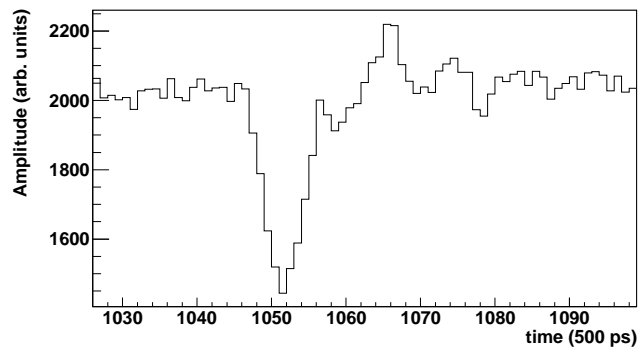


Figure 4.18: Typical pulse registered with fADC data acquisition system. The pulse corresponds to a ^{136}Xe ion detected in the RPC-30 prototype. Each channel in the y and x axis corresponds to 0.5 mV and 500 ps, respectively.

To overcome this problem, a specific and more advanced data acquisition system was implemented for timing measurements. For this purpose,

we used a compact TACQUILA board, with a dedicated FEE coupled to it (STAR), developed at GSI for timing measurements with tRPCs for the FOPI experiment [Koc05]. This board consists of 16 channels with differential inputs of $50\ \Omega$ of impedance and a TAC ASIC (Time-to-Amplitude Converter) integrated chip for timing measurements in each one of them. A common threshold value for each channel can be set in order to discriminate the signals according to their amplitude. Additionally, the charge of the pulses can be digitized with a QDC piggy-back board. The bandwidth of the complete system is around 1 GHz and its intrinsic time resolution about 25 ps [Sch04].

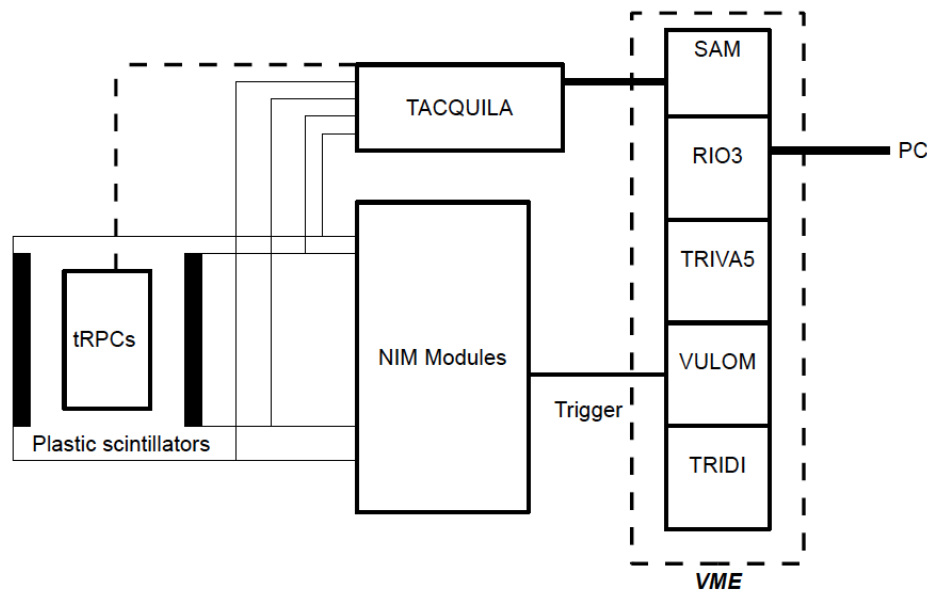


Figure 4.19: Same as Fig. 4.17 but for TACQUILA system.

The signals of the detectors and an internal 40 MHz clock provided the *start* and *stop* signals for each TAC, respectively. Therefore all signals must fit within a 25 ns time window. This will be improved in the future in an advanced TACQUILA design, which includes an extra channel to synchronize the timing of the channels, beyond the natural 40 MHz clock of the original design. This is important in order to fit all the physics cases in the appropriate time window. The time signal provided by the TAC is digitized in a 12-bit ADC (4096 channels) and, simultaneously, the 10-bit QDC (1024 channels) continuously integrates the charge of the signal pulse. The QDC value decays to zero through a capacitor. When a trigger is accepted, the data is registered and monitored by the acquisition. Each TACQUILA chan-

nel was calibrated in time and charge and the QDC pedestals were evaluated and subtracted in the measurements. The time calibration was done by dividing the number of channels spanned by each ADC spectrum by 25 ns. Concerning the charge calibration (see the plot in Fig. 4.20), we fed TACQUILA with the same pulses we used for the calibration of the FEE boards (see detailed description at Sec. 4.4.2), which allowed us to determine the correlation between input pulse charge, Q_{in} , and QDC channel, Q_{TAC} .

Concerning the data acquisition, the hardware and dead time control were made in this case with the RIO3 and TRIVA boards but the triggers were managed by a VULOM module instead of the NIM logic trigger used for the flash-ADC and distributed by means of a TRIDI module. The data read out (MBS) was made with a SAM board, specifically designed for these kinds of systems, sending the data through a differential bus (GTB) to a computer running the LynxOS operating system (see Fig. 4.19).

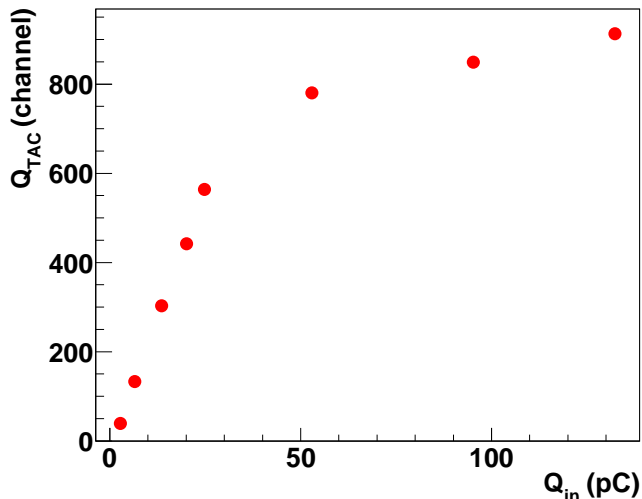


Figure 4.20: TACQUILA charge calibration curve. See text for details.

In addition, the intrinsic time resolution of the FEE (BFR92A+OPA657) + TACQUILA system was also determined to evaluate its contribution to the time-of-flight measurements. In order to do this, we used two different FEE boards fed with the same reference signal with their output directly connected to TACQUILA channels. The resolution was determined by fitting the time difference of both calibrated channels yielding a value of $\sigma_{elec} = 48/\sqrt{2} = 34$ ps (see Fig. 4.21). According to the time resolution of the TACQUILA system (25 ps) we obtain a time resolution for the BFR92A+OPA657 FEE

of around 23 ps.

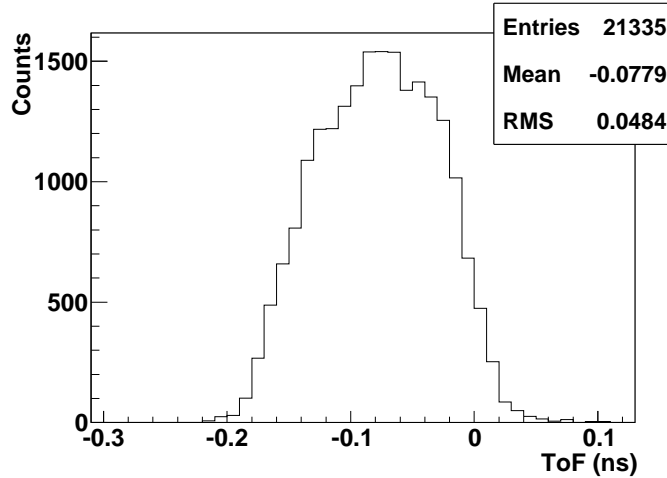


Figure 4.21: Distribution of the time difference between two TACQUILA channels fed with the same pulse amplified by two different FEE boards.

4.4.5. Dedicated experiments

In order to investigate the performance of the tRPCs in a proper scenario we conducted several experiments with relativistic ions with different nuclear charges at GSI (Germany), and with electrons at ELSA (CEA-DAM, France) and ELBE (HZDR-Rossendorf, Germany) facilities. We will explain in this section the different experiments carried out to characterize different tRPC prototypes in efficiency and time resolution terms and determine their optimum working point. A survey of the different experiments with their main features is presented in Table 4.1.

In experiments conducted at GSI the RPC-11 and RPC-12 prototypes were irradiated with ^{12}C and ^{64}Ni beams at 700 and 500 A MeV of energy, respectively, with a repetition rate of few tens of Hz/cm² [Cas12b]. Furthermore, another experiment was conducted where RPC-11 prototype was bombarded with medium-mass fragments produced in the fragmentation of ^{238}U ions at 750 A MeV [Ayy12]. In these experiments, we used an external trigger with full efficiency in the detection of heavy ions, composed of two BC420 plastic scintillators (10 mm thickness) coupled to two Hamamatsu H6533 PMTs. The RPCs were supplied with a gas mixture composed of 90% of $\text{C}_2\text{H}_2\text{F}_4$ and 10% of SF_6 . The signals from the tRPCs

Beam	Energy	Prototype	Rate	Trigger system
^{12}C	700 A MeV	RPC-11	tens of Hz/cm ²	2 BC420+H6533
^{64}Ni	500 A MeV	RPC-11/RPC-12	tens of Hz/cm ²	2 BC420+H6533
^{238}U frag.	750 A MeV	RPC-11	tens of Hz/cm ²	2 BC420+H6533
^{136}Xe	560 A MeV	RPC-30	3-10 Hz/cm ²	2 EJ-232+H6533
^{238}U	1 A GeV	RPC-25	5 Hz/cm ²	self-trigger
e^- bunches	10 MeV	RPC-25	5 Hz	1 EJ-232+H6533
Single e^-	40 MeV	RPC-40	up to 13 MHz	self-trigger

Table 4.1: Experiments performed with different tRPC prototypes.

(GALI-S66+MAXIM4223 FEE) and the PMTs were fully digitized in our flash-ADC-based acquisition.

The performance of the RPC-30 prototype, composed by two single-gap multi-strip modules, was measured also at GSI by bombarding the prototype with a ^{136}Xe beam at 560 A MeV with a repetition rate below 30 Hz and a spill of 5 s of duration. The signal time and charge distributions were digitized using a TACQUILA board. Because of the synchrotron operation mode being at such a low rate, this was largely fluctuating from 4 up to 50 Hz between different spills. A 1 Hz calibration trigger implemented in the TACQUILA acquisition system was used to monitor the beam rate at each second, and moreover, allowed us to determine two different rate per unit area intervals considering a cross section for the gaussian beam with a standard deviation of $\sigma \approx 0.42$ cm, as measured by a multi-wire proportional chamber placed behind our setup. Therefore, the profile of the beam where almost all the events are located has around 0.6 cm² of cross section.

Both modules of the prototype were surrounded by an external trigger made of two EJ-232 plastic scintillators of 1 mm thickness coupled to two PMTs as explained in the section 4.4.1. The trigger system was aligned with the central strips of both modules defining the active detection zone. We used a gas mixture composed of 90% of $\text{C}_2\text{H}_2\text{F}_4$ and 10% of SF_6 , without iso- C_4H_{10} . The prototype was operated in a high voltage (HV) plateau ranging from 2700 up to 3400 V.

Another different beam test was done irradiating the RPC-25 prototype with a beam of ^{238}U at 1000 A MeV with a rate of around 5 Hz/cm². In this experiment the coincidence of the four signals given by FEE channels of both modules of the RPC-25 prototype provided the trigger for the TAC-

QUILA acquisition system. Because of the short duration of the test, data of interest was obtained for 2800 V using the same gas mixture of the previous experiments.

The same prototype was also tested using an electron beam at ELSA facility [Par]. 10 MeV mono-energetic electrons were delivered in bunches (about 10^4) of a few ps length. According to the features of such a beam, we simulate the large energy lost by the heavy ions in the RPC by means of many electron losses in a small spot (2 mm). In such a short time, each bunch induces a unique signal in each tRPC module whose charge is correlated with the number of electrons of the bunch. The beam intensity can be modulated using a polarizer, allowing us to vary the beam intensity in two orders of magnitude. A low repetition rate of 5 Hz was considered throughout experiment. In this case, the detection trigger was constructed using the temporal coincidence of the four signals provided by both modules of the RPC-25 (two signals per module) and the signals of a thin plastic scintillator (similar to the one used in the ^{136}Xe experiment) placed upstream of the tRPCs. The signals were digitized using the TACQUILA board. The gas mixture we used in this experiment was composed of 90% of $\text{C}_2\text{H}_2\text{F}_4$ and 10% of SF_6 and the tRPCs were operated at different voltages and beam intensities during the measurements.

At the ELBE facility, the RPC-40 was irradiated with a single electron beam of 40 MeV and up to 13 MHz of repetition rate. We used three different gas mixtures completely free of iso-butane, just varying the proportion of SF_6 . The chamber was operated at 3200 V.

4.4.6. RPC prototypes performance

In this section we present the results of the tests performed with the different prototypes. The main working parameters of the tRPCs, efficiency and time resolution, are discussed and compared to extract conclusions about its performance under such conditions.

4.4.6.1. Time resolution

The time resolution of the RPC-30 prototype (two medium-size single-gap modules with BFR92A+OPA657 FEE) under ^{136}Xe irradiation was obtained from the ToF measurement between the central strip of both tRPCs of the prototype. Considering the resolution of the time-of-flight as:

$$\sigma_{\text{ToF}}^2 = \sigma_{\text{RPC1}}^2 + \sigma_{\text{RPC2}}^2 \quad (4.6)$$

where σ_{RPC1}^2 and σ_{RPC2}^2 are the time resolutions of the first and the second tRPC modules of the RPC-30 prototype. Assuming both tRPCs with the same time resolution ($\sigma_{RPC1}^2 = \sigma_{RPC2}^2 = \sigma_{RPC}^2$), we obtain:

$$\sigma_{tRPC} = \frac{\sigma_{ToF}}{\sqrt{2}} \quad (4.7)$$

The plastic scintillator placed upstream of the prototype was used to determine the position of the beam and reject possible contaminants. The position, shown in Fig. 4.22, was defined as the time difference between the signals read-out from both PMTs of this scintillator, T_L^1 and T_R^1 . Only the beam particles between the dashed lines were considered, being rejected the contribution of a second charge state of the ^{136}Xe beam (peak on the left). The relative angle of incidence, defined from the difference between the position measured in both scintillators, was also determined to consider those particles aligned with the beam direction (see Fig. 4.23).

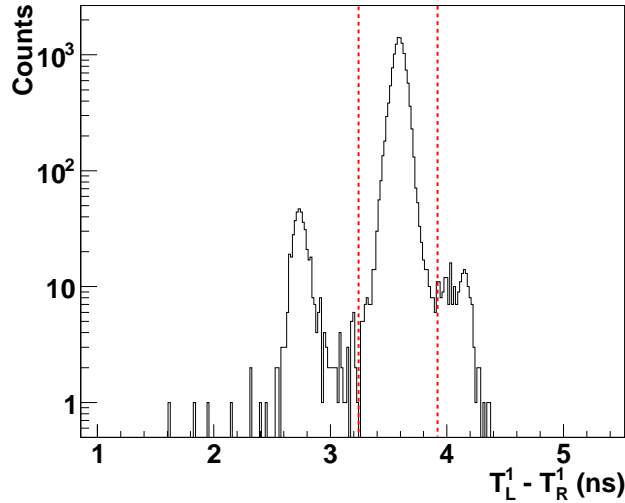


Figure 4.22: Position of the ^{136}Xe beam in the first scintillator.

Considering these conditions, we calculated the time-of-flight between both tRPCs, and therefore, the time resolution of each module was given by:

$$\sigma_{tRPC} = \frac{T_L^{RPC1} - T_L^{RPC2}}{\sqrt{2}} \quad (4.8)$$

where T_L^{RPC1} and T_L^{RPC2} are the times of the left channels of the central strips of the first and the second tRPC digitized in TACQUILA. At 2900 V,

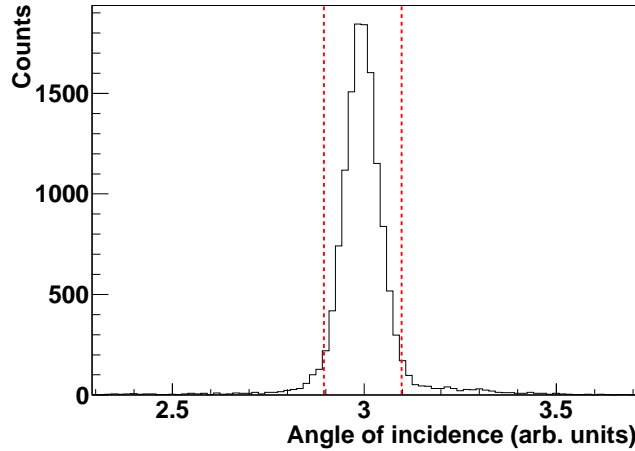


Figure 4.23: Relative angle of incidence of the ^{136}Xe ions measured by the plastic scintillators. The narrow shape of the distribution indicates the good collimation of the beam.

a time resolution of $\frac{68 \text{ ps}}{\sqrt{2}} = 48 \text{ ps}$ ($1.5\text{-}\sigma$ ^{***}) was achieved with an irradiation rate of around $3\text{-}10 \text{ Hz/cm}^2$ (see Fig. 4.24). This resolution was slightly improved by correcting the time-walk effect due to the different height of the pulses, reaching a time resolution of around $\frac{65 \text{ ps}}{\sqrt{2}} = 46 \text{ ps}$ ($1.5\text{-}\sigma$). To do this, we represented the time of flight as a function of the charge of the pulse of the left channel of the second RPC (Q_L^{RPC2}). In the upper right panel of Fig. 4.24 one can see the slight correlation due to low amplitude signals that was corrected using a second order polynomial function. A second time walk effect correction using the charge distribution does not improved the resolution. It is worth pointing out that the tails at $3\text{-}\sigma$ amounted to 20% due to an artifact by an incorrect operation of the detector, either related with the FEE amplification or the setup of the TACQUILA acquisition. The events of the tail at the right side of the distribution increases with the applied voltage and the rate, having a value of 35% at 3400 V and $15\text{-}25 \text{ Hz/cm}^2$, respectively. Nevertheless, in the two dimensional plots of the right panels of Fig. 4.24 one can see that these artifact events can be clearly distinguished (around 0.5 ns in the y axis of the plot of the lower panel) from the physical events of the ToF distribution. These events only affect the determination of the time resolution beyond $1.5\text{-}\sigma$ and to the time-walk effect correction with respect to the charge of the pulse measured in the left channel of the

^{***}the Gaussian distribution was fitted in a range of $1.5\text{-}\sigma$ around the mean value

first RPC (Q_L^{RPC1}). A dedicated investigation is being carried out in order to identify and solve such problems.

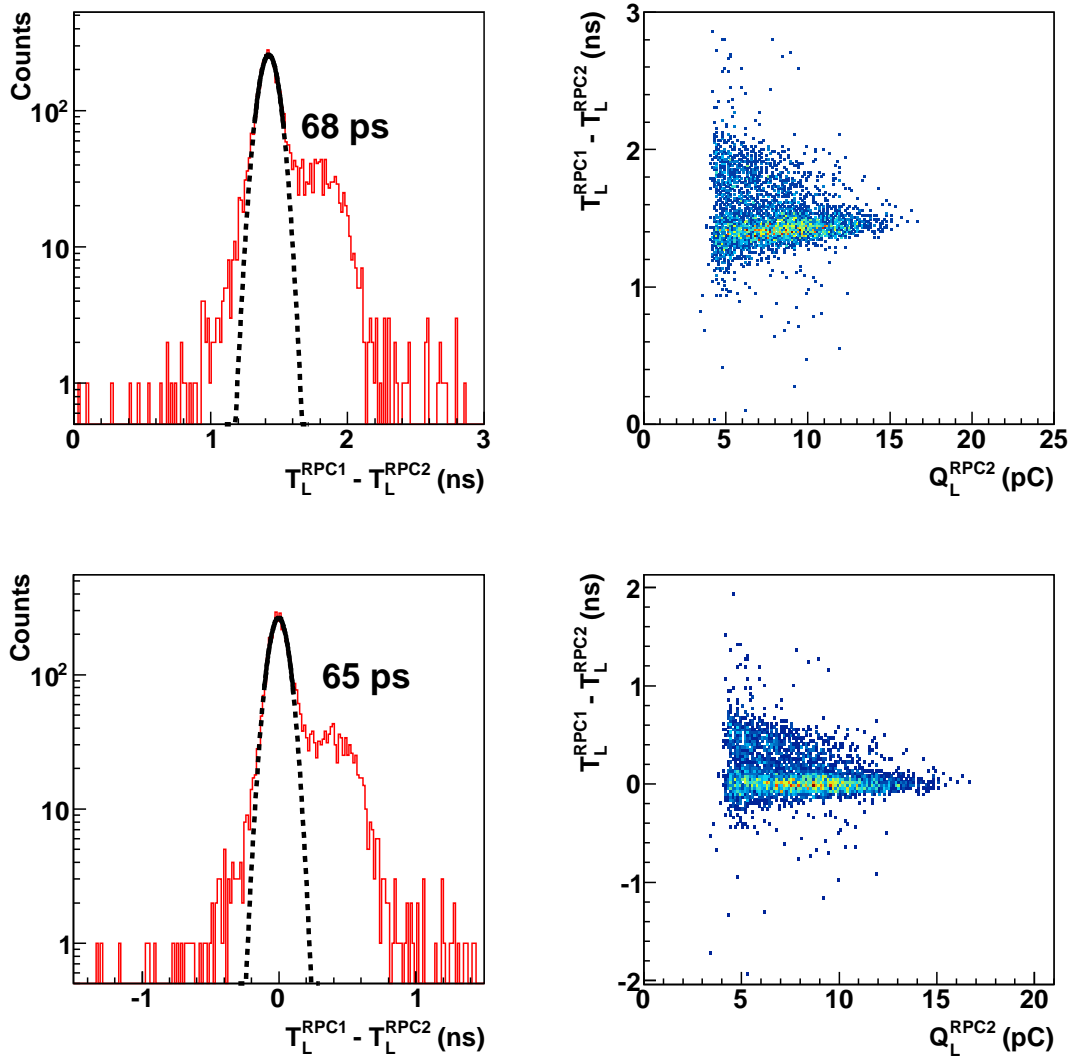


Figure 4.24: Left panels: Time of flight distribution of ^{136}Xe ions measured between both modules of the RPC-30 prototype operated at 2900 V and a rate of 3-10 Hz/cm² before (upper panel) and after (lower panel) the slewing correction. Right panels: Time of flight measured in the RPC-30 prototype as a function of Q_L^{RPC2} before (upper panel) and after (lower panel) slewing correction.

We investigated also the effect of the high voltage in the time resolution under a constant irradiation rate. As can be seen in Fig. 4.25, the time

resolution (σ_{tRPC}) strongly depends on the applied high voltage. There exist a minimum value at 2900 V of 46 ps and the resolution degrades as the voltage is increased, reaching a value of 56 ps ($1.5\text{-}\sigma$) at 3200 V. For lower voltage values, the time resolution is compatible within the error bars, having around 49 ps ($1.5\text{-}\sigma$) at 2700 V. These time resolution values were determined after each respective time slewing corrections.

We also present in Fig. 4.26 the linear correlation between the applied voltage and the mean value of the signal charge distribution. Plotted data with their uncertainty corresponds to the mean value and the root mean square (RMS) of the charge distribution. It can be seen that the best time resolution at 2900 V corresponds to an averaged signal charge of 9.6 pC. There exists a compromise between the amplification of the signal by increasing the high voltage and the time resolution. Unfortunately, due to the particular performance of TACQUILA FEE and QDC described previously, the avalanche pulses with large amplitude induced by ^{136}Xe ions are near the saturation regime and could not be separated from streamers. Therefore, we assumed that an increasing contribution of the latter led to a degradation of the time resolution. In conclusion, a high voltage plateau was found between 2700 and 3100 V where the tRPC can be safely operated reducing the streamers contribution.

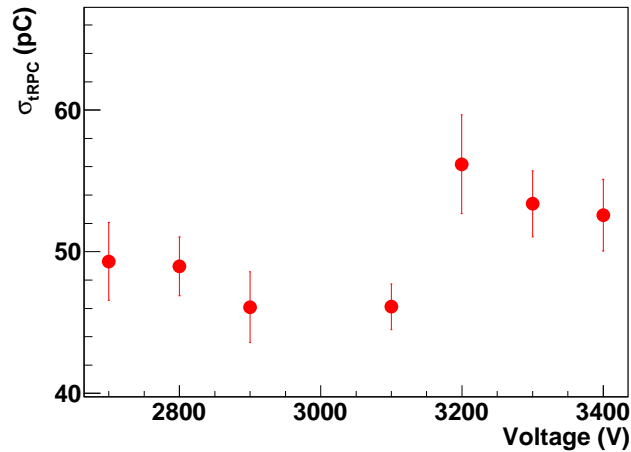


Figure 4.25: Time resolution ($1.5\text{-}\sigma$) of the RPC-30 prototype as a function of the applied voltage for ^{136}Xe at 560 A MeV and 3-10 Hz/cm² of irradiation rate.

Time resolution was measured also in the experiment conducted at the FRagment Separator (GSI) where the RPC-25 prototype (small-size double-gap prototype with BFR92A+MAXIM FEE) was irradiated ^{238}U beam at

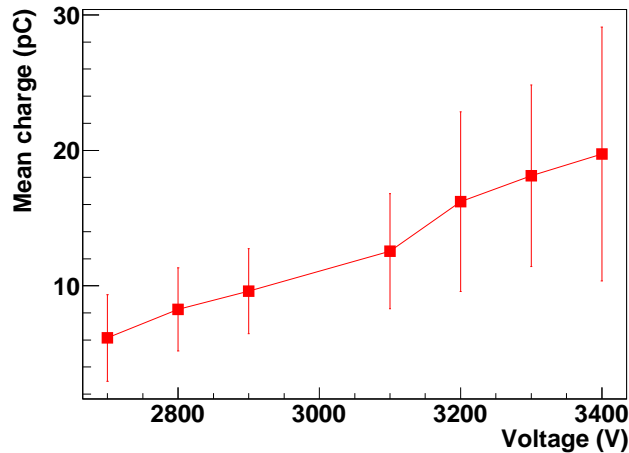


Figure 4.26: Mean value of the signal charge distribution as a function of the applied voltage for ^{136}Xe at 560 A MeV.

1000 A MeV with a rate of about 5 Hz/cm². To reduce to the minimum the rate per area unit, the beam was defocused using the FRS spectrometer and only ^{238}U particles impinging in the center of the strips of both modules of this prototype were considered (see Fig. 4.27). The position was calculated with the time difference between the signal measured at both ends of the strip of each module (RPC1 and RPC2).

We followed the same procedure previously outlined to determine the time of flight between both modules of this prototype. According to the equation 4.8, a time resolution of $\frac{97}{\sqrt{2}} = 69$ ps ($1.5\text{-}\sigma$) was obtained after slewing correction, with a mean value for the signal charge distribution of 8.6 pC at 2800 V. Figure 4.28 shows the time of flight distributions measured between the left FEE channel of both modules of the RPC-25 prototype and its correlation with the charge of the signal, Q_L^{RPC1} . The tails at $3 - \sigma$ amounted to 10%.

The time resolution of the RPC-25 prototype was also measured with electrons bunches trying to reproduce the energy deposition of an ion with a given atomic number. We measured the time difference between the two tRPC modules and each of the modules with respect to the plastic scintillator to determine the time resolution of each individual detector. Fig. 4.29 show the time resolution of the best performing tRPC (RPC2) as a function of the beam intensity at 2800 (triangles) and 3000 V (open circles). As can be seen, the time resolution of this tRPC presents a strong dependence with respect to the beam intensity reaching a value of 30 ps ($1.5\text{-}\sigma$) for an

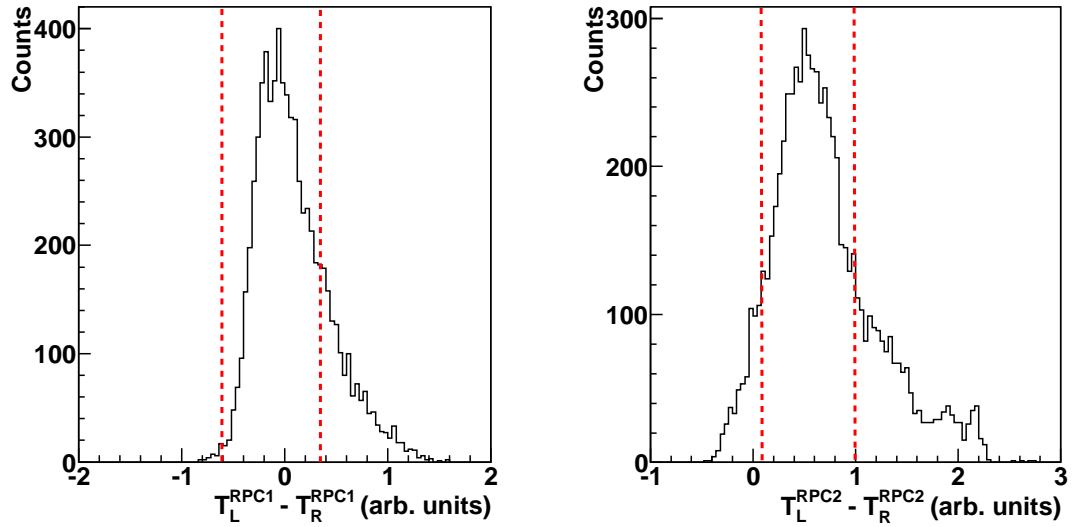


Figure 4.27: Left panel: Position of the ^{238}U beam in the first RPC. Only events between both dashed lines were considered. Right panel: Same as left panel but for the second RPC.

intensity of 20%, which is close to TACQUILA's intrinsic resolution. For the lowest beam intensity (0.5%), the time resolution is degraded above 80 ps ($1.5\text{-}\sigma$). The large number of electrons per bunch, which increases with the beam intensity, favours the formation of high amplitude pulses due to multiple avalanches created during its short length (few ps), and as a consequence the time resolution is improved. Also, it is worth pointing out that no significant difference was found in the time resolution measured at two different voltages (2800 and 3000 V). The resolution of the reference scintillator is also presented in this plot slightly better results, especially at lower beam intensities. The time resolution of the RPC-25 prototype (2800 V) as a function of the mean charge of the signal is shown in Fig. 4.30 for electron bunches (triangles) and ^{238}U (star). The time resolution of the reference scintillator is also included (squares).

If we want to compare the results obtained with these two prototypes, it has to be considered that in the electron bunches and ^{238}U experiments the signals coming from the tRPCs were divided to construct the acquisition trigger. Thus, the amplitude and charge of the signals were reduced to half of their initial value. Moreover as mentioned before, the RPC-30 prototype used to measure ^{136}Xe ions was equipped with a FEE (BFR92A+OPA657)

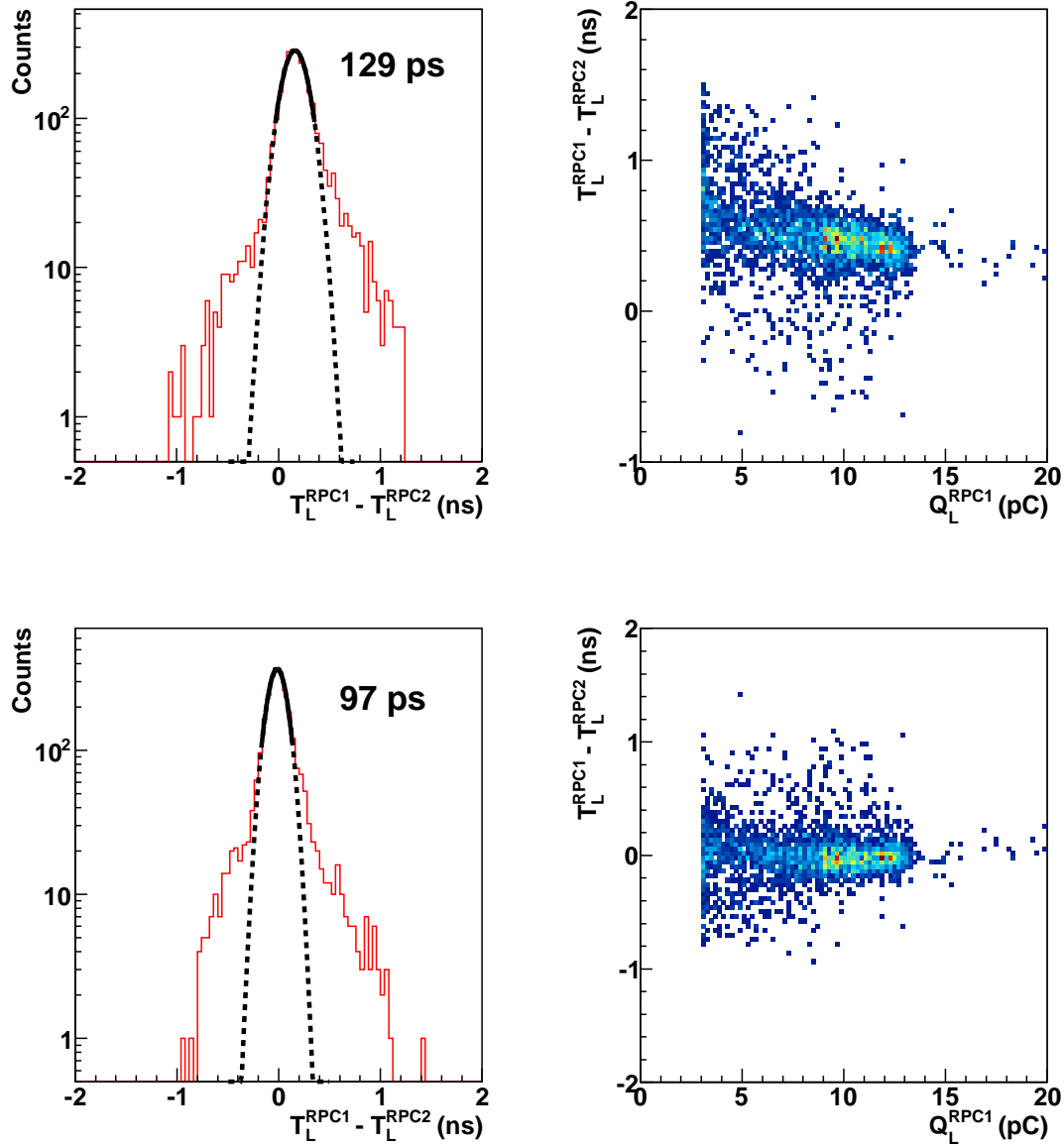


Figure 4.28: Left panels: Time of flight distribution of ^{238}U ions measured between both modules of the RPC-25 prototype operated at 2800 V and a rate of 5 Hz/cm^2 before (upper panel) and after (lower panel) the slewing correction. Right panels: Time of flight measured in the RPC-25 prototype as a function of Q_L^{RPC1} before (upper panel) and after (lower panel) slewing correction.

with a charge gain factor of 4, while the FEE equipped in the RPC-25 prototype (BFR92A+MAXIM4224) had a charge gain factor of around 22 in the range of interest. It has been taken also into account that the charge of the signal induced in the double-gap tRPC can be double with respect to the single-gap tRPC because the signal corresponds to the sum of the signals induced in each gap. This leads to a total gain factor between both FEE ranging from 2.5 up to 5. The mean value of the charge of the signals induced in RPC-30 prototype by ^{136}Xe ions at 2800 V is about 8 pC. This value can be extrapolated into the BFR92A+MAXIM4224 FEE, yielding a value that can be in a range from 20 up to 40 pC. As can be seen in Fig. 4.30, for those mean values of the extrapolated mean charge, a time resolution between 35 and 55 ps ($1.5\text{-}\sigma$) was achieved with the RPC-25 and the BFR92A+MAXIM4224 FEE measuring electron bunches, in good agreement with the value of 49 ps ($1.5\text{-}\sigma$) obtained with the RPC-30 measuring ^{136}Xe (solid circle) at 2800 V. Therefore, measurements using electron bunches represent an alternative method to investigate the behavior of the tRPC under large charge depositions. The critical influence of the rate effects on the time resolution and on the mean charge value of the pulses will be studied for the ^{136}Xe experiment in the next section.

From this comparison we can infer that the value of the time resolution obtained for the ^{136}Xe measurement is worse than the one obtained for electron bunches over the same charge range. This can be attributed to the much larger amplitudes of the signals induced by the electron bunches in the RPCs probably due to the FEE amplification and the ionization mechanism of the electron bunch. In addition, the relatively high irradiation rate of the ^{136}Xe beam also reduces the amplitude of the signals induced in the tRPC. Therefore, a proper gain of the amplification stage of the FEE would in principle improve the time resolution without an increase of the streamer production.

4.4.6.2. Effect of the rate in the time resolution

It is well-known that irradiation rate is a key parameter that can smear out the timing performances of tRPCs working with MIPs [Fon99]. Furthermore, the expected effect in the detection of heavy ions is critical because of the much larger deposited energies compared to MIPs. A local reduction of the effective gap field is produced with an increase of the rate due to the space charge effect, which could be especially important in the case of the heavy ions. We have explained in the previous section that during the ^{136}Xe experiment we were able to determine two different rate intervals of 3-10 and 15-25 Hz/cm². In Fig. 4.31 the mean charge of the signals is represented as a function of the applied voltage for the different rate intervals considered

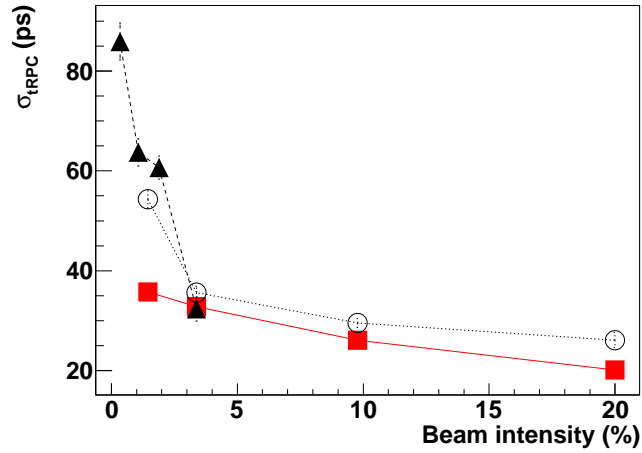


Figure 4.29: Time resolution of one of the tRPC modules of the RPC-25 prototype as a function of the electron beam intensity at 2800 V (triangles) and 3000 V (open circles). Squares refers to the time resolution of the reference scintillator.

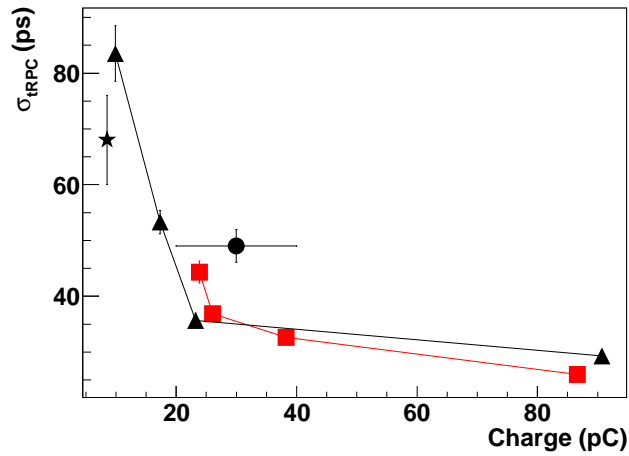


Figure 4.30: Time resolution as a function of the charge of the signal. RPC-25 with electron bunches (triangles), RPC-25 with ^{238}U (star), reference scintillator with electron bunches (squares) and RPC-30 with ^{136}Xe after extrapolation (solid circle). The values of the time resolution of the reference scintillator with electron bunches were offset by a constant value to point out its evolution with the beam intensity. See text for details.

here. We observe an effect of the charge reduction as the rate increases for each value of the voltage. Moreover, the effect seems to be constant along the entire voltage range, revealing that it does not play a role in this charge quenching.

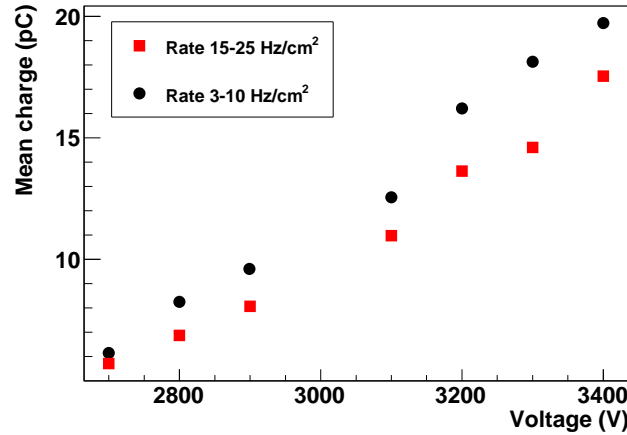


Figure 4.31: Mean value of the signal charge as a function of the applied voltage for ^{136}Xe at 560 A MeV at two different irradiation rates per surface unit.

At higher rates, an electric-field screening is clearly induced due to the large amount of charge carriers moving inside the gap. Since the tRPC does not have enough time to disperse the charge collected at the electrodes, each particle sees an average reduction of the effective gap field, the avalanche process is less intense and as a consequence the mean value of the signal charge distribution and its width are reduced, as can be seen in Fig. 4.32.

If we assume that the reduction of the charge is due to the effect of the field screening, at 2900 V the value of the charge for an irradiation rate of 3-10 Hz/cm² is around 10 pC neglecting the streamer contribution at these voltage. If the rate is increased up to 15-25 Hz/cm², the applied voltage has to be increased up to 3100 V to preserve the same equivalent field averaged over all the events. Therefore, as shown in Fig. 4.33 the time resolution is degraded when the irradiation rate is increased from 3-10 up 15-25 Hz/cm² due to the reduction of the mean charge of the pulses. This effect is dramatically enhanced for higher values of the voltage probably due to other mechanisms that play an important role in the formation of the signal under such conditions. The reduction of the mean value and width of the charge distribution due to the charge damping really makes the separation between avalanche and streamer pulses more complicate. Therefore, it is

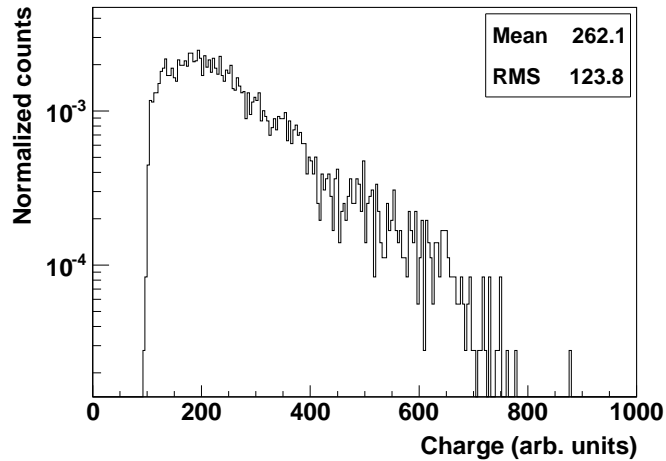
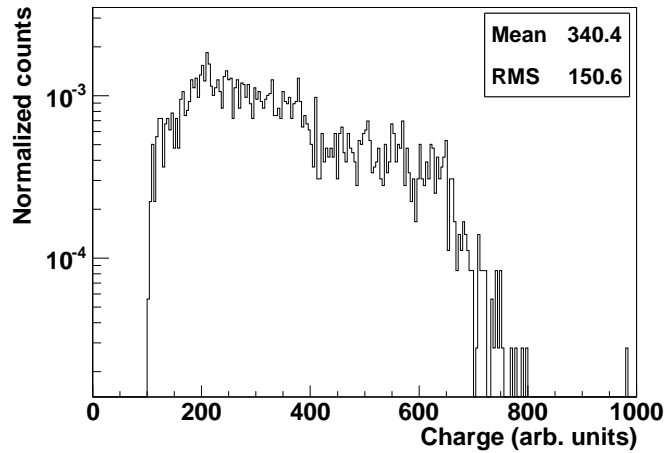


Figure 4.32: Upper panel: Normalized signal charge distribution of the RPC-30 under an irradiation rate of 3-10 Hz/cm². Lower panel: Same as the upper panel but for an irradiation rate of 15-25 Hz/cm².

very difficult to extract conclusions about the streamer production taking into account the behavior of the FEE+TACQUILA.

4.4.6.3. Efficiency and streamer production

The efficiencies of the RPC-11 (double-gap) and RPC-22 (single-gap) prototypes was measured for different ions over a wide range of nuclear charges. To do this, we performed two experiments at GSI where the prototypes were irradiated with ¹²C and ⁶⁴Ni beams at 700 and 500 A MeV of energy, respec-

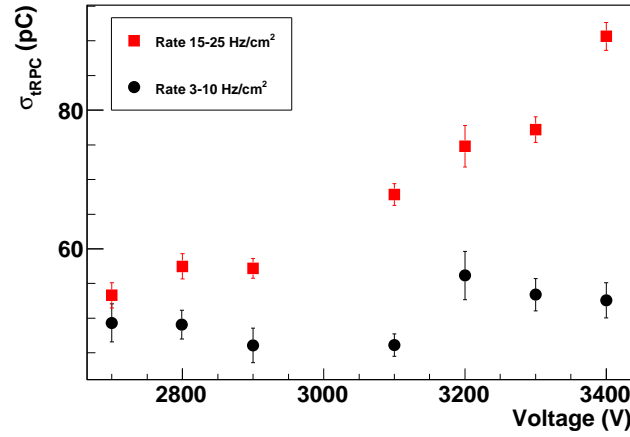


Figure 4.33: Time resolution as a function of the applied voltage for ^{136}Xe at 560 A MeV at two different irradiation rates per surface unit.

tively, at repetition rate of a few tens of Hz/cm².

The efficiency was determined from the fraction of ions detected by the scintillators, that were also detected by the RPC. The amplitude threshold from which we determined whether a particle induced a signal in the detectors was set considering the noise level of the PMTs and FEE of the RPCs.

In the experiment with ^{12}C , only the efficiency of the RPC-11 was investigated. It was possible to identify projectiles traversing the RPC with different atomic numbers by using the scintillators signals. The energy loss of the ions in the scintillators, which is proportional to the squared atomic number, was determined by integrating the signals coming from the PMTs. In the scatter plot of Fig. 4.34 the energy loss of the ^{12}C ions in both plastic scintillators is shown. Those ions produced in nuclear reactions between the primary beam ($Z=6$) and layers of matter situated upstream of our setup are located in the diagonal of this plot. These ions had almost the same energy loss in both scintillators indicating that their atomic number did not change when traversing the RPC. A calibration was done considering that each spot in this diagonal corresponds to an atomic number from $Z=1$ up to $Z=5$. On the other hand, ions located in the vertical line of the same plot reacted in any layer of matter of the setup losing protons. The projection onto the y axis displayed in Fig. 4.35 corresponds to the energy loss in the scintillator placed downstream of the RPC. The peak corresponding to $Z=1$ is cut due to the thresholds applied to the signals coming from the PMTs to construct an acquisition trigger, which ensures a negligible noise level. In the ^{65}Ni beam

test we used the primary beam ($Z=28$) only to investigate the efficiency of the RPC-11 and the RPC-22.

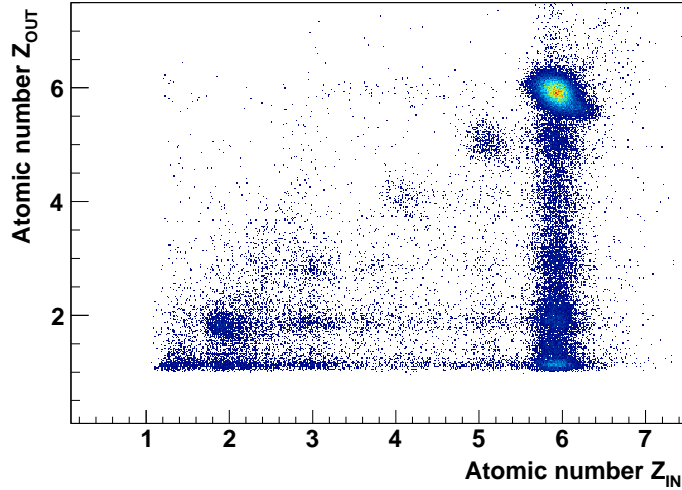


Figure 4.34: Two-dimensional plot of the energy loss of ^{12}C ions in both plastic scintillators. Z_{IN} and Z_{OUT} refers to the scintillators placed upstream and downstream of the target, respectively.

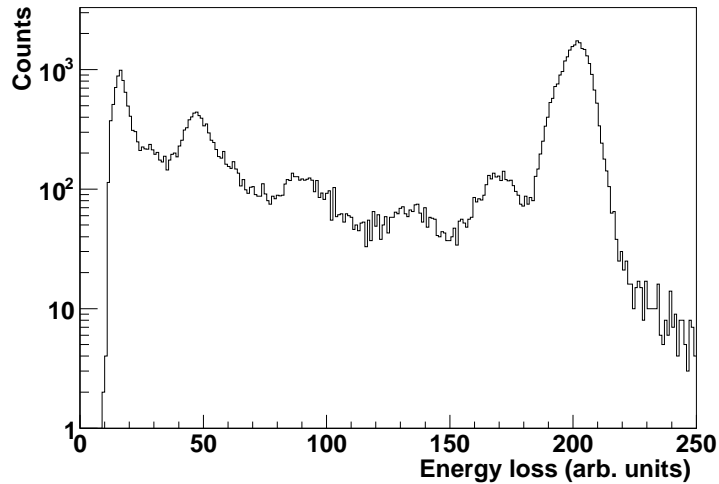


Figure 4.35: Energy loss of ^{12}C ions in the scintillator placed downstream of the RPC.

The efficiency for ions with different atomic numbers as a function of the high voltage is plotted in Fig. 4.36. Concerning ions with $Z=6$ (open squares),

we obtained an efficiency of 100% in all the high voltage range studied here. For $Z=2$ (open circles), detection efficiencies near 100% are rapidly achieved for voltages higher than 2500 V. The value of the detection efficiency for protons (open triangles) at 2500 V drops to 55% and is increased up to 90% for high voltage values higher than 3000 V. This is consistent with results for efficiency obtained with MIPs (90-94% [Fon02]). Efficiency values for $Z=2$, 3 and 4, also about 100%, are not included for the sake of simplicity. In this plot we also present the efficiency for $Z=28$ measured with the RPC-11 (stars) and RPC-22 (solid circles) prototypes. One can see that an efficiency close to 100% was reached with both single- and double-gap prototypes. To extend these results to higher atomic numbers we performed an experiment using a similar experimental scheme and working parameters where the efficiency of the RPC-11 prototype was determined under the irradiation of medium-mass nuclei produced in the ^{238}U fragmentation at 750 A MeV [Ayy12]. According to a rough calibration, in this experiment we covered an atomic range of around $Z=1$ up to $Z=38$, but with poor energy loss resolution due to the limited dynamic range of the plastic scintillators. Moreover, the efficiency was also determined for the medium-size one-gap prototype under ^{136}Xe irradiation, by using the information of the spectra digitized with TACQUILA. Here, the efficiency was defined as the ratio between the number of events detected by one of the modules of this prototype and the number of registered triggers by using the reference plastic scintillators. It has to be considered that the scintillators of the trigger were not perfectly aligned with the strip, thus, a possible geometrical factor could reduce the nominal value of the efficiency. Another issue is that of the threshold of each TACQUILA channel whose value depends on the noise/signal ratio and is normally lower than the trigger threshold. Signals with an amplitude lower than this threshold are rejected decreasing the measured efficiency.

The results of all these experiments are compiled in Fig. 4.37 where we plot the efficiency as a function of the atomic number. We can conclude that the ionization produced by ions with atomic charges higher than $Z=1$ is sufficient to start the avalanche process even at values of electric field well below the typical ones of tRPCs devoted to MIPs measurements. The large plateaus that represent the efficiency with respect to the nuclear charge and the voltage, are mandatory to define a working point with adequate parameters and gains. Moreover, we have tested that the dynamic range of the FEE accommodates the entire distribution of avalanche signals. No limitations due to the rate were observed, even at the higher values of the atomic number studied in this work. Furthermore, single-gap tRPCs (RPC-22 and the medium-size prototype) present detection efficiencies compatible with 100% which opens the possibility of a drastic reduction of matter in

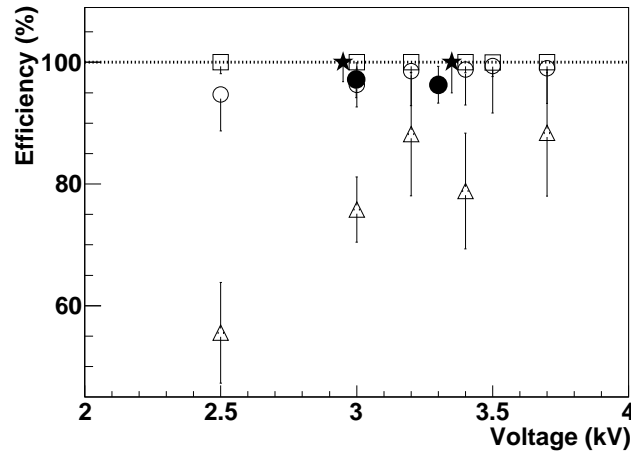


Figure 4.36: Detection efficiency of the RPC-11 as a function of the applied voltage for different atomic numbers: $Z=1$ (open triangles), $Z=2$ (open circles), $Z=6$ (open squares), $Z=28$ (stars) and $Z=28$ for the RPC-22 (solid circles).

the design of the detector in order to reduce the straggling when detecting relativistic heavy ions.

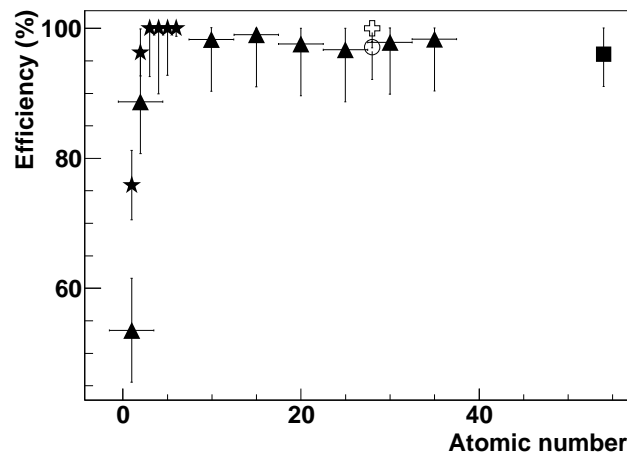


Figure 4.37: Efficiency as a function of the atomic number measured in different experiments (3000 V): ^{238}U fragments (triangles), ^{12}C (stars), ^{65}Ni for RPC-11 (cross) and RPC-22 (open circle), and ^{136}Xe (square).

In the last part of this section the streamer production is analyzed for

the experiments where the RPC-11 was irradiated with ions produced in the fragmentation of ^{12}C and ^{64}Ni ions. Owing to the large energy deposition of the ions in the active gas volume of the tRPC a relatively large fraction of streamers is expected which may induce negative effects such as dead-time increase and time resolution worsening. The FEE installed in this RPC (GALI-S66+MAXIM4223) allowed us to separate streamer from avalanche pulses due to the total gain of the amplifier stage. The ratio between the streamer signals respect to the total as a function of the applied high voltage for different ions is shown in Fig. 4.38. As can be seen, the streamer ratio strongly depends on the gap voltage and the atomic number of the ions, being below 1% and 10% for $Z=6$ at 3000 V and 3200 V, respectively. Beyond the latter value of the voltage, the streamer ratio increases rapidly for all the atomic numbers. In the case of $Z=28$, the streamer contribution amounts up to 28%, but the trends indicate that for lower values of the field the ratio drops to a value between 5 and 10%. However, in the case of the single-gap RPC (RPC-22) the streamer ratio is even lower at 3000 V (2%) showing that the amount of streamers depends on the number of gaps.

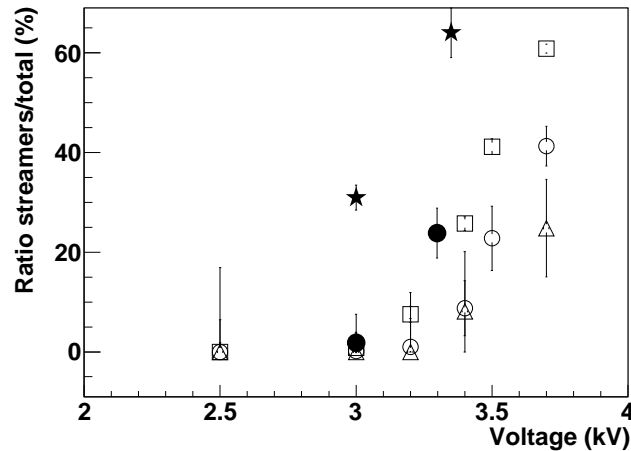


Figure 4.38: Ratio of streamer signals to total for different ions: $Z=28$ (stars), $Z=6$ (squares), $Z=5$ (circles), and $Z=2$ (triangles).

4.4.6.4. Effect of the gas mixture

To investigate the effect of the gas mixture, an experiment was performed at HZDR - Rossendorf (Germany) where the RPC-40 prototype was irradiated with a single electron beam of 40 MeV. We used three different gas

mixtures completely free of iso-butane, just varying the proportion of SF₆. The chamber was operated at 3200 V, voltage for which streamer formation is already expected. For each gas mixture we obtained a similar time resolution of around 200 ps due to the beam profile, which is far from the results obtained with heavy ions and electron bunches. Therefore, we investigated the role of the gas mixture on the streamer formation. Contrary to the case of the ¹³⁶Xe, streamer pulses can be separated from the avalanche pulses in the charge distributions, probably due to the relatively low electric-field screening effect induced by the free charge carriers liberated in the ionization of the gas by these 40 MeV electrons, almost in the range of MIPs. The results are presented in table 4.2 and the charge distributions digitized by TACQUILA are shown in Fig. 4.39. As expected, the reduction of the proportion of SF₆ in the gas mixture leads to a substantial increase of the streamer pulses (up to 24%) since the avalanche formation is less quenched. However, an adequate reduced proportion of SF₆ may favor the pulse charge amplification minimizing the walk-time effect and leading to an improvement of the time resolution while keeping the streamer production as low as possible.

Gas mixture	Streamer ratio (%)
90% C ₂ H ₂ F ₄ - 10% SF ₆	1%
95% C ₂ H ₂ F ₄ - 5% SF ₆	8%
99% C ₂ H ₂ F ₄ - 1% SF ₆	24%

Table 4.2: Ratio of streamers for different gas mixtures under 40 MeV electron irradiation.

4.5. Conceptual design of the iToF tRPC modules

Considering the working parameters previously discussed, the tRPCs for the iToF will be constituted by single-gap gas-tight modules made of two soda-lime glass plates of 1 mm thickness glued together and segmented in 16 strips of 1000 mm × 20 mm width and 2 mm of separation, covering a surface of 1 m and 2 m in the vertical and horizontal coordinates, respectively. The spatial resolution expected, according to the time-resolution, is about a few mm which is enough for correcting the flight path length of the order of 15 m.

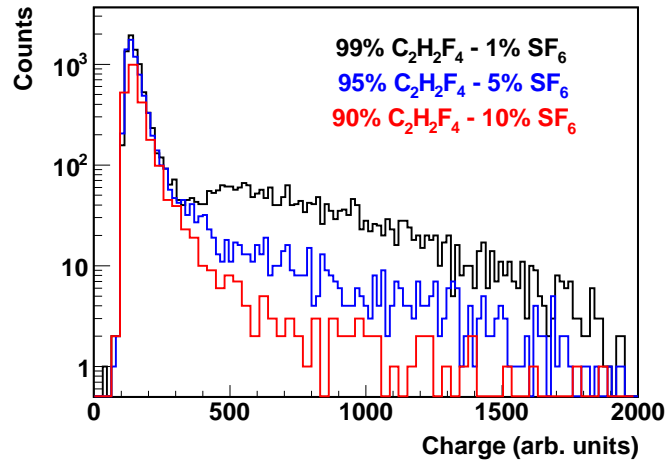


Figure 4.39: Charge distributions obtained for different gas mixtures.

With this configuration, the resolution can be improved by measuring in the consecutive detecting planes of the iToF while minimizing the amount of matter and so the energy straggling. If four detection planes are considered, the total thickness of the detector amounts to 8 mm of soda-lime glass which fits with the typical range of the heaviest ions of interest (15 mm for ²³⁸U at 400 A MeV). This improves the time resolution by a factor two. Multi-hit capabilities will be also fulfilled by crossing the strips of consecutive planes 90°. This configuration will ensure its proper performance under low rate conditions minimizing the streamer production and improving the efficiency up to around 100%.

However, the use of tRPCs for the construction of the iToF present several drawbacks. As we demonstrated in the previous sections, the irradiation rate which is critical in the RPCs does not represent a problem in other timing detectors such as scintillators. Moreover, tRPCs constructed with soda-lime glass are fragile detectors, in particular the ones studied in this work which are assembled using two plates of 1 mm thickness. Despite this amount of matter is relatively small (2 mm), only 1 mm of thickness is needed in the case of plastic scintillators. One last disadvantage is the fact that the tRPC are gaseous detectors which are always more complicated to maintain and manage. On the other hand, tRPCs can accommodate a larger dynamic range with respect to the plastic scintillators.

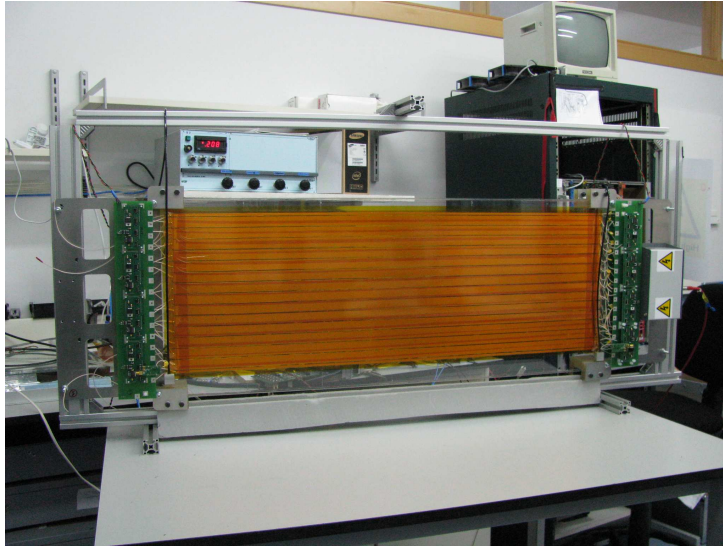


Figure 4.40: Multi-strip single-gap tRPC module for the iToF.

4.6. Conclusions

In this chapter we have investigated the performance of the tRPCs under relativistic heavy ion irradiation. Several tRPCs prototypes have been tested with ions over a wide range of atomic number such as ^{12}C , ^{64}Ni , ^{238}U and ^{136}Xe obtaining efficiency values of around 100% while maintaining a low streamer production. This defines a regime where the tRPCs can be safely operated. It is worth pointing out that these efficiency values were achieved with both double- and single-gap tRPCs prototypes which opens the possibility of a reduction of the amount of layers of the detector. Time resolutions of around 69 ps were obtained with the RPC-25 prototype when measuring ^{238}U ions at a repetition rate of around 5 Hz/cm² and values of around 46 ps were achieved with the RPC-30 prototype under ^{136}Xe at 560 A MeV irradiation with a repetition rate over the range between 3 and 10 Hz/cm². According to the results we have obtained, we can conclude that the irradiation rate is a critical parameter that must be taken into account when working with heavy ions. Resistive materials capable of dealing with higher irradiation rates are an option that can be considered for future prototypes. We also have demonstrated that a gas mixture with proper proportions of SF₆ is a critical parameter to be determined in order to control the streamer formation under such large energy deposition.

The dedicated FEE developed by our group for the prototypes was designed and adapted to the signals produced by ions, and moreover, the data

acquisition for timing measurements used in this work (TACQUILA) fulfills our needs. However, it has to be noted that the resolution of the FEE+TACQUILA system (34 ps) could be limiting the time resolution of the measurements. In addition, time resolutions obtained with prototypes equipped with different FEE boards indicate that a proper amplification of the signal is important in order to improve the time resolution while keeping a low streamer production. Therefore, a more intensive research and development on the FEE is needed in order to improve the performance of the prototypes in time resolution terms.

Despite these points, the performance of the electronic system is quite robust and works according to the requirements as stated before. In conclusion, these tRPCs provide excellent time resolutions and high efficiencies dealing with relativistic heavy ions at a low irradiation rate and their features can fulfill the requirements needed for the construction of a tRPC-based ion ToF wall.

Conclusions

In this work we have presented the results of two experiments performed to investigate the fission process at high excitation energies. We have studied the proton-induced fission of ^{181}Ta at 1000, 800, 500 and 300 A MeV, and, the proton- and deuteron-induced fission of ^{208}Pb at 500 MeV. Both experiments were performed at GSI using a dedicated setup for fission studies in inverse kinematics which allowed to unambiguously detect both fission fragments simultaneously and determine several observables.

In the ^{181}Ta experiment, two ionization chambers surrounding the target were used to select reactions produced in the liquid hydrogen cell which enhanced the selection of the fission events that were determined by measuring both fission fragments in coincidence using a double plastic scintillator covering the angular acceptance of the fragments emitted in forward direction. Total fission cross sections were determined with high accuracy and the results were compared to data measured in previous experiments. These new data complete the scarce measurements existing above 700 MeV and allowed to address the existing discrepancies. At energies below 500 MeV, where the expected low value of the cross section complicates the selection of the fission channel among other reactions mechanisms, we have demonstrated that a proper data reduction and a careful determination of the uncertainties provide precise values that enabled a clarification of previous results. Our data are consistent with the highest values of the fission cross sections determined in previous experiments for that energy range. Moreover, these results are in good agreement over the entire energy range studied in this work when compared to the systematic predictions established by Prokofiev. Thus, this experiment has proven the inverse kinematics technique to be suitable for the detection of both fission fragments in coincidence in reactions involving low fissility nuclei such as ^{181}Ta .

In addition, the results obtained from this experiment were compared with model calculations performed with an intra-nuclear cascade code (INCL and ISABEL) coupled to a code describing the evaporation process of a highly excited nucleus. For the latter stage we used ABLA statistical code includ-

ing a time-dependent fission width governed by a friction parameter β , and, GEMINI++ code based on pure statistical description of fission. It has to be taken into account that the level-density parameter in ABLA was determined following Ignatyuk's prescription, while the level-density ratio a_f/a_n is fixed to 1.036 in GEMINI++. A complete benchmark of the codes revealed that the predictions obtained with INCL+ABLA and ISABEL+ABLA considering a value of $\beta = 2 \times 10^{21} \text{ s}^{-1}$ have a rather good agreement with the experimental data, while INCL+GEMINI++ calculations underestimate the values in the entire range due to a lower level-density parameter ratio. Moreover, despite ABLA and GEMINI++ predict very similar residual nuclei, in the former the particle evaporation is made during the ground-to-saddle stage, while in the latter the evaporation happens during the saddle-to-scission evolution because of the effect of the nuclear dissipation.

In addition, we demonstrated that the fission channel opens at higher excitation energies when using GEMINI++. We also proved that dissipative effects included in ABLA are too strong at low excitation energies (300 MeV of beam energy) where the fission decay rate depends on the density of states above the fission barrier according to Bohr-Wheeler's statistical model. This fact is stressed comparing the calculations with the experimental data and the Prokofiev systematics. We also demonstrated that despite calculations made with INCL and ISABEL providing similar values of the angular momentum and total fission cross section, fissioning systems determined with ISABEL have a lower fissility, reducing the fission probability. In conclusion, the total fission cross section does not represent a robust observable in order to characterize the predictive power of such codes, although several conclusions about the effect of the dissipation strength may be inferred.

An improved version of the previous detection setup including a double ionization chamber (Twin MUSIC) and a time-of-flight wall was utilized to investigate proton- and deuteron-induced fission of ^{208}Pb . In this case, we measured both fission fragments in coincidence using the Twin MUSIC which allowed us to determine their atomic number with high resolution. Using this information, the atomic number of the fissioning system was reconstructed (Z_1+Z_2) for both reactions assuming no proton evaporation. This enabled the determination of two observables with valuable information regarding dissipative effects on the fission process, partial fission cross sections and the width of the charge distribution of the fission fragments. While partial fission cross sections as a function of Z_1+Z_2 showed that higher excitation energies are induced in the reaction with the deuteron creating fissile systems with larger charge loss, the width of the fission fragments charge distribution (σ_z) as a function of Z_1+Z_2 revealed that this signature only depends on the temperature the system has at the saddle point T_{sad} for each Z_1+Z_2 value.

These conclusions also support the fact that each one of these signatures is sensitive to one of the stages of the reaction. The partial fission cross sections are determined during the cascade stage while the width of the fission fragment charge distribution σ_z is sensitive to the evaporation phase. Moreover, we have seen that the total fission cross sections obtained in this work for $^{208}\text{Pb}+\text{p}$ and $^{208}\text{Pb}+\text{d}$ are consistent within the error bars with other works, considering a small variation over an energy range between 500 and 1000 MeV of the fission cross sections obtained in these works.

To extract conclusions about the strength of the dissipation factor and the transient delay during the pre-saddle stage we used the same codes as in the previous analysis. We validated the cascade stage performing calculations with INCL+ABLA and ISABEL+ABLA which proved that the shape of the distribution of the partial fission cross sections as a function of Z_1+Z_2 depends on the excitation energy initially induced to the system while their magnitude is given by the β value considered for the evaporation stage. For the reaction $^{208}\text{Pb}+\text{d}$ calculated with INCL+ABLA and $\beta = 4 \times 10^{21} \text{ s}^{-1}$ partial fission cross sections have a good agreement with the experimental data in almost the entire Z_1+Z_2 range while calculations made according to a purely statistical model lead to an overestimation. Predictions of INCL+ABLA and ISABEL+ABLA concerning $^{208}\text{Pb}+\text{p}$ at 500 MeV show several discrepancies with respect to the experimental data, especially for those fissioning systems with higher excitation energy. The magnitude of the transient effects was estimated using the information inferred from the comparison of the fission fragments charge distribution measured for both reactions with calculations made with INCL+ABLA proving that the data fits with predictions considering $\beta = 4 \times 10^{21} \text{ s}^{-1}$. This fact was explained as a reduction of the temperature at the saddle point, T_{sad} , due to the delay induced in the system during the early stage of the fission process. According to the results obtained in this experiment, we conclude that spallation reactions investigated using the inverse kinematics technique are a powerful and reliable reaction mechanism to investigate dynamical effects of the fission process due to the characteristics of the fissioning systems and the measured observables. The value of the dissipation strength considered in this work is consistent with other systems with different fissility and fission barriers, showing that the data can be reproduced for all these systems with a value of β between 2 and $4 \times 10^{21} \text{ s}^{-1}$. In particular, we have seen in this work that the results obtained for ^{181}Ta and ^{208}Pb are compatible considering these values of the dissipation coefficient β .

The experimental setups described in this work will be substantially improved in next-generation fission experiments using the inverse kinematics technique (SOFIA, R³B and FELISE) which will provide a most complete

reconstruction of the fission reaction measuring other important observables constrained in the present experiments due to the limited available technology. One of the main challenges will be the measurement of the masses of the fission fragments. A state-of-the-art ToF wall with a demanding time resolution will be needed for this purpose. We have undertaken a dedicated R&D program to prove the feasibility of tRPCs (timing Resistive Plate Chambers) for the construction of such time-of-flight wall for fission residues and heavy ions in the framework of the R³B experiment (iToF) for the future FAIR facility. In this work, we have demonstrated that tRPCs can be safely operated under the irradiation of relativistic heavy ions while keeping their outstanding timing properties. We have built and tested several small-size double-gap single-strip tRPC prototypes with ions with a wide range of atomic number such as ¹²C, ⁶⁴Ni and ²³⁸U giving values of efficiency of 100% and time resolutions of around 46 ps while keeping the streamer production low enough. Moreover, outstanding time resolutions of about 30 ps have been obtained when measuring electron bunches. Nevertheless, according to the iToF requirements, the best results have been obtained so far with a single-gap self-contained multi-strip tRPC prototype made with two glass plates of 40 cm×20 cm of area and 1 mm thickness achieving efficiency values of around 100% and time resolutions of 46 ps under the irradiation of a ¹³⁶Xe beam at 560 A MeV and a repetition rate of 3-10 Hz/cm². The minimization of the amount of matter contained in this prototype will enable the possibility of a ToF wall with several detection planes which in principle would improve the time resolution of the measurements. However, one has to keep in mind that the effect of the rate is critical in such detectors, and thus, this opens the possibility of the construction of prototypes based on resistive materials capable to of dealing with higher irradiation rates. In addition, the proper setup of the amplification stage of the FEE of the prototypes could led to an improvement of the time resolution of the detector.

We have demonstrated that the performance of the tRPC under relativistic heavy ion irradiation fulfills the requirements needed for the construction of the iToF detector, achieving time resolutions below 50 ps under low rate conditions. According to these results, a module of the iToF detector could consist of a single-gap multi-strip tRPC made with two soda-lime glass plates of 1000 mm× 425 mm glued together, defining a single 300 μm gap. The active detection zone will consist in 16 copper strips of 1000 mm × 20 mm, separated by 2 mm. A gas mixture consisting of 90% of C₂H₂F₄ and 10% of SF₆ will be used to control the streamer formation and will allow the correct performance of the tRPCs operated at 2900 V, at maximum.

Resumen en castellano

La fisión es un mecanismo extremadamente complejo que requiere un tratamiento dinámico para describir la evolución del proceso en términos de grados de libertad intrínsecos y colectivos. Las teorías de transporte [Wei80] basadas en cálculos realizados mediante ecuaciones de Langevin demuestran ser una herramienta potente y adecuada para describir la evolución colectiva del núcleo y constituye la base de los modelos actuales. Sin embargo, más de 70 años de intensa investigación revelan que el proceso de fisión está lejos de ser completamente entendido y nuestro conocimiento teórico es insatisfactorio. Las medidas experimentales de observables fuertemente ligados al proceso, tales como probabilidades de fisión, masas, cargas y energía cinética de los fragmentos y multiplicidades de neutrones, partículas cargadas ligeras y rayos γ , están limitadas por la tecnología disponible, de modo que resultados obtenidos con diferentes técnicas y dispositivos experimentales presentan discrepancias. Se requiere una mejora substancial para resolver las discrepancias existentes, validar modelos modernos y extender los límites actuales de nuestro conocimiento sobre el proceso de fisión.

La fisión nuclear juega un papel fundamental en la descripción de varias propiedades nucleares y provee de información valiosa en temas generales de física y astrofísica. En efecto, ciertos temas como los efectos de capa en núcleos super e hiperdeformados, el proceso r en la nucleosíntesis, la viscosidad de la materia nuclear y la transferencia de energía entre los fragmentos emergentes necesitan de una descripción correcta del proceso de fisión. También es extremadamente importante en la producción de haces de iones radioactivos (RIB) dedicados a estudiar las propiedades de núcleos exóticos ricos en neutrones lejos de la estabilidad [Lou11] y en el desarrollo de fuentes de espalación para el desarrollo de Sistemas Asistidos por Acelerador (ADS).

La primera descripción del proceso de fisión fue establecida por Bohr-Wheeler [Boh39]. En este modelo estadístico, la probabilidad de desexcitación de un núcleo pesado está gobernada por el espacio de fases disponible en el punto de silla (*saddle point*). Kramers [Kra40] propuso una descripción de la fisión como un proceso de difusión usando la ecuación de Fokker-Planck

(FPE) que describe la evolución del sistema de acuerdo a los grados de libertad intrínsecos y colectivos. La solución a esta ecuación conduce a una reducción de la anchura de fisión predicha por el modelo estadístico debida a la transferencia de energía entre los grados de libertad que se incluye como parámetro en la FPE (β). Pocos años después el concepto de tiempo de tránsito fue introducido por Grangé *et al.* [Gra83] después de resolver numéricamente la FPE asumiendo unas condiciones iniciales que coinciden con las estudiadas en este trabajo. Esta solución lleva a una descripción de la anchura de fisión dependiente del tiempo que constituye una gran diferencia con respecto al modelo de Bohr-Wheeler. La fisión está altamente inhibida al principio del proceso que necesita un cierto tiempo de tránsito para alcanzar el valor estacionario (por encima de la barrera de fisión) de la anchura de fisión predicha por Kramers. Estas ideas establecen la bases de nuestro conocimiento actual de la dinámica del proceso de fisión.

En este trabajo hemos investigado la fisión del ^{181}Ta inducida por protones y la fisión del ^{208}Pb inducida por protones y deuterones a energías relativistas. Los experimentos se realizaron en el laboratorio GSI (Darmstadt) empleando un dispositivo experimental diseñado para estudios de fisión en cinemática inversa. Este dispositivo facilita el contaje de proyectiles y la identificación de los productos de la reacción. Los resultados obtenidos en estos experimentos se emplearon para extraer resultados cuantitativos acerca de efectos de disipación y tiempos dinámicos en la etapa durante la cual el sistema alcanza el punto de silla. El uso de modelos de reacción punteros que describen el proceso de fisión es necesario para este propósito.

Los resultados obtenidos han demostrado que este dispositivo experimental, junto a la técnica utilizada, constituyen una herramienta potente para realizar experimentos dedicados a medir las propiedades del proceso de fisión. Sin embargo, la identificación isotópica de ambos fragmentos de fisión simultáneamente y con gran precisión, representa hoy en día un problema complejo presente en los más modernos sistemas de detección. El programa científico del experimento R³B en la futura instalación FAIR (Alemania) incluirá el estudio completo de reacciones de fisión espalación y multifragmentación en cinemática inversa usando un esquema de detección similar al de este trabajo, incluyendo además un dipolo magnético. La identificación isotópica de los productos de reacción requerirá detectores de tiempo de vuelo con alta eficiencia y aceptación, y una resolución temporal por debajo de 30 ps (desviación estándar). Para cumplir estos requisitos, se propone la construcción de un muro de tiempo de vuelo (ToF wall) basado en cámaras de placas resistivas (RPCs). Este tipo de detectores son a menudo usados en experimentos de física de altas energías, pero su funcionamiento en la detección de iones pesados a energías relativistas es escasamente conocidos. En este traba-

jo hemos estudiado la eficiencia de detección y la resolución de prototipos de RPC irradiados con diferentes haces de iones pesados y con electrones. Los resultados obtenidos indican la validez de estos detectores para la detección de iones pesados y la construcción de un muro de tiempo de vuelo.

Fisión inducida por protones en ^{181}Ta

En este experimento realizado en el GSI, el haz de iones de ^{181}Ta se aceleró a 300, 500, 800 and 1000 A MeV de energía con una intensidad del orden de 10^4 iones/s, incidiendo posteriormente en un blanco de hidrógeno líquido. Debido a la cinemática de la reacción, ambos fragmentos de fisión son emitidos hacia delante, permitiendo su detección con alta eficiencia. La figura 1 muestra el esquema del dispositivo experimental.

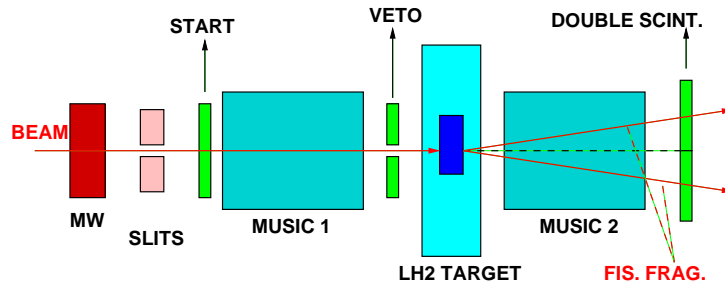


Figura 1: Esquema del montaje experimental usado en este experimento.

Dos cámaras de ionización MUSIC80 [Pfü94] colocadas a la salida y entrada del blanco de hidrógeno respectivamente, midieron la pérdida de energía de los iones de tántalo y de los productos de la reacción. Mediante un gráfico bidimensional que representa la pérdida de energía en ambas cámaras de ionización identificamos reacciones de ^{181}Ta producidas en el blanco de hidrógeno y en capas de materia presentes en la línea de haz. De esta manera, seleccionamos los sucesos de fisión producidos únicamente en el blanco. Usando un sistema de dos plásticos centelleadores, ambos fragmentos se detectan en coincidencia, permitiéndonos separar los fragmentos de fisión de otros productos de reacción con un número atómico similar que constituyen un importante fondo de contaminación debido a la baja probabilidad de fisión del ^{181}Ta . El número de eventos de fisión se extrae de esta identificación, una vez corregido y eliminado el fondo de fragmentación y evaporación.

Las secciones eficaces de fisión se determinan con el cociente entre el número de sucesos de fisión y el de proyectiles, ambos normalizados al espesor del blanco. Varios factores de corrección debidos a la eficiencia geométrica

del dispositivo experimental, la atenuación de los proyectiles en el blanco y reacciones secundarias de los fragmentos de fisión. Además las incertidumbres estadísticas y sistemáticas se determinaron cuidadosamente para obtener resultados de gran precisión.

Las secciones eficaces obtenidas en este trabajo se presentan en la figura 2, comparadas a otros resultados obtenidos en experimentos previos y con la sistemática establecida por Prokofiev. Nuestras medidas confirman las medidas realizadas por Yurevich *et al.* y las secciones eficaces predichas por la sistemática por encima de 700 MeV, resolviendo las discrepancias. A energías más bajas, los datos de este trabajo permiten clarificar los resultados previos, favoreciendo aquellos que presentan las secciones eficaces más altas. Además, en este rango también se confirman las predicciones de la sistemática.

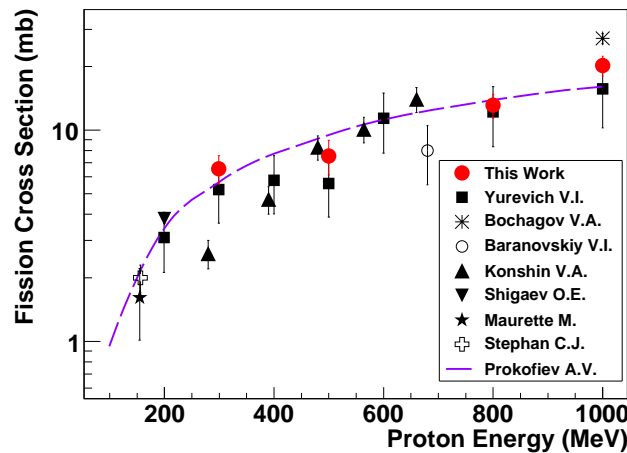


Figura 2: Secciones eficaces de fisión medidas en este trabajo (círculos) comparadas con datos medidos en experimentos anteriores y predicciones de la sistemática de Prokofiev (línea a trazos).

Los datos obtenidos también se comparan con cálculos obtenidos con códigos que describen el proceso de fisión a alta energía de excitación. En este trabajo hemos usado dos tipos de cascada intranuclear (INCL e ISABEL) que describen el proceso de interacción entre el protón y el ^{181}Ta , acoplados a un código de evaporación. Para esta segunda etapa hemos usado el código estadístico ABLA que incluye una anchura de fisión dependiente del tiempo y un tratamiento de la disipación nuclear, y el código GEMINI++ que se basa puramente en una descripción estadística del proceso de fisión. La comparación con los datos experimentales nos permite validar su poder predictivo. Como puede verse en la figura 3, los resultados obtenidos usando

INCL+ABLA e ISABEL+ABLA considerando un coeficiente de disipación $\beta = 2,0 \times 10^{21} \text{ s}^{-1}$ están en buen acuerdo con los datos experimentales, mientras que los cálculos hechos con INCL+GEMINI++ subestiman los valores de sección eficaz. Esto es debido a que durante la evaporación calculada mediante GEMINI++, el sistema fisiona con una más energía de excitación más alta.

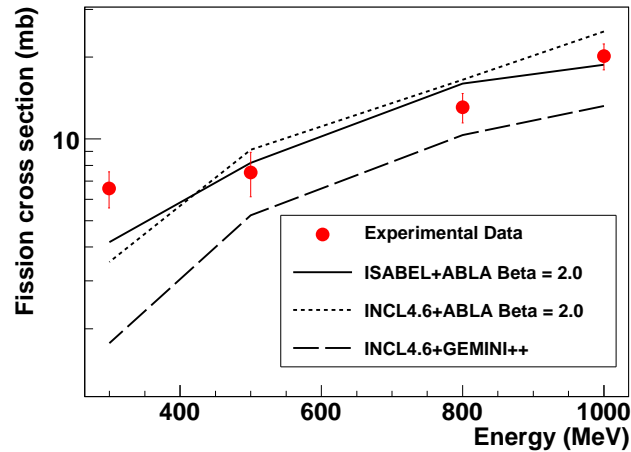


Figura 3: Secciones eficaces de fisión medidas en este trabajo (círculos) comparadas a cálculos realizados usando INCL4.6+ABLA y ISABEL+ABLA ($\beta = 2,0 \times 10^{21} \text{ s}^{-1}$), y INCL+GEMINI++.

Fisión inducida por protones y deuterones en ^{208}Pb a 500 A MeV

En este experimento se siguió un procedimiento experimental similar al anterior, pero el sistema de detección se mejoró substancialmente incluyendo una doble cámara de ionización Twin MUSIC y un muro de tiempo de vuelo, como puede verse en el esquema de la figura 4.

Usando cinemática inversa, los iones de ^{208}Pb son acelerados a 500 A MeV hasta el sistema de detección donde incide en el blanco de de hidrógeno o deuterio líquido produciéndose la reacción. Similarmente al experimento anterior, dos cámaras de ionización puestas delante y detrás del blanco en la línea de haz se utilizaron para identificar reacciones en el blanco de hidrógeno y no en otras capas de material presentes en la línea de haz. Los fragmentos de fisión se detectan simultáneamente en ambas partes de la doble cámara

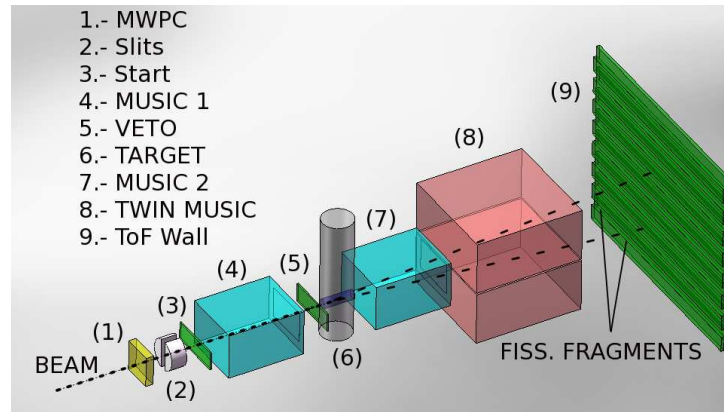


Figura 4: Sistema de detección usado en este experimento.

de ionización, y a su vez, son identificados en número atómico (Z) con una resolución del orden de $\Delta Z = 0,55$. La eficiencia de detección de la Twin MUSIC se determinó mediante la posición de los fragmentos de fisión en el muro de tiempo de vuelo. Con esta información somos capaces de reconstruir el número atómico del sistema fisionante Z_1+Z_2 .

Varios observables pueden extraerse a partir de estas medidas. La sección eficaz total de fisión para ambas reacciones se determinó con gran precisión. Para extraer conclusiones acerca del proceso, estudiamos la sección eficaz de fisión parcial y la anchura de la distribución de carga de los fragmentos de fisión (σ_z), ambas en función de Z_1+Z_2 . Estos observables son sensibles a los efectos de disipación y tiempo de tránsito y nos permiten estudiar las características derivadas de inducir la fisión con protones o con deuterones.

La sección eficaces parciales muestra una diferencia clara entre la energía de excitación inducida en ambos sistemas (ver figura 5), siendo mayor en el caso del deuterón, lo que nos permite crear sistema fisionantes con un menor número atómico. Así pues, la forma del espectro de secciones eficaces parciales está estrechamente relacionada con la distribución de energía de excitación, la cual a su vez, sólo depende de cómo el sistema fisionante se define durante la etapa de colisión.

Respecto a σ_z en función de Z_1+Z_2 , podemos observar en la figura 6, que para ambos sistemas se obtienen resultados similares, lo que indica que este proceso es independiente del canal de entrada usado para crear el sistema fisionante, y está estrechamente relacionado con la temperatura que alcanza el sistema en el punto de silla (T_{sad}) [Ben02]. Además, este observable se determina durante la etapa de evaporación, lo que significa que cada uno de los observables definidos es sensible a una de las etapas del proceso de fisión.

Estos resultados se comparan con cálculos realizados con códigos que des-

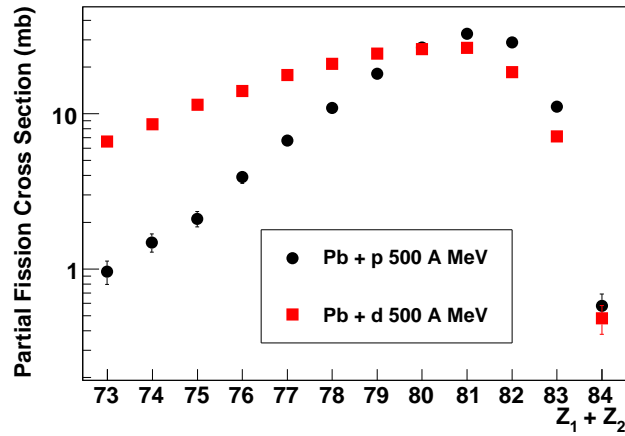


Figura 5: Secciones eficaces parciales de fisión en función de Z_1+Z_2 para las reacciones $^{208}\text{Pb}+p$ (círculos) y $^{208}\text{Pb}+d$ (cuadrados) a 500 A MeV.

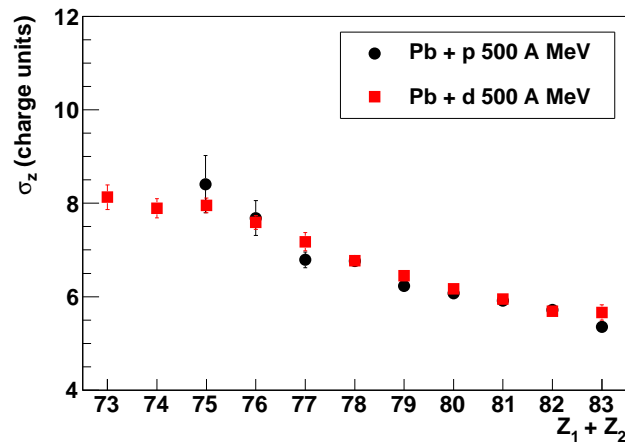


Figura 6: σ_z en función de Z_1+Z_2 .

criben la fisión, lo que nos permite determinar cual es el efecto de la disipación nuclear en el proceso de fisión. Para cálculos realizados con INCL+ABLA e ISABEL+ABLA para la reacción $^{208}\text{Pb}+p$ a 500 A MeV obtenemos una sección eficaz total de fisión similar, 96 y 114 respectivamente ($\beta = 4,0 \times 10^{21} \text{ s}^{-1}$). Sin embargo, como podemos ver en el panel superior de la figura 7, la forma de la curva calculada en ambos casos es bastante diferente debido a la energía de excitación inducida en la etapa de colisión. En el caso de la reacción $^{208}\text{Pb}+d$ a 500 A MeV (panel inferior de la figura 7), existe

un buen acuerdo entre cálculos realizados con INCL+ABLA considerando $\beta = 4,0 \times 10^{21} \text{ s}^{-1}$ y los datos experimentales.

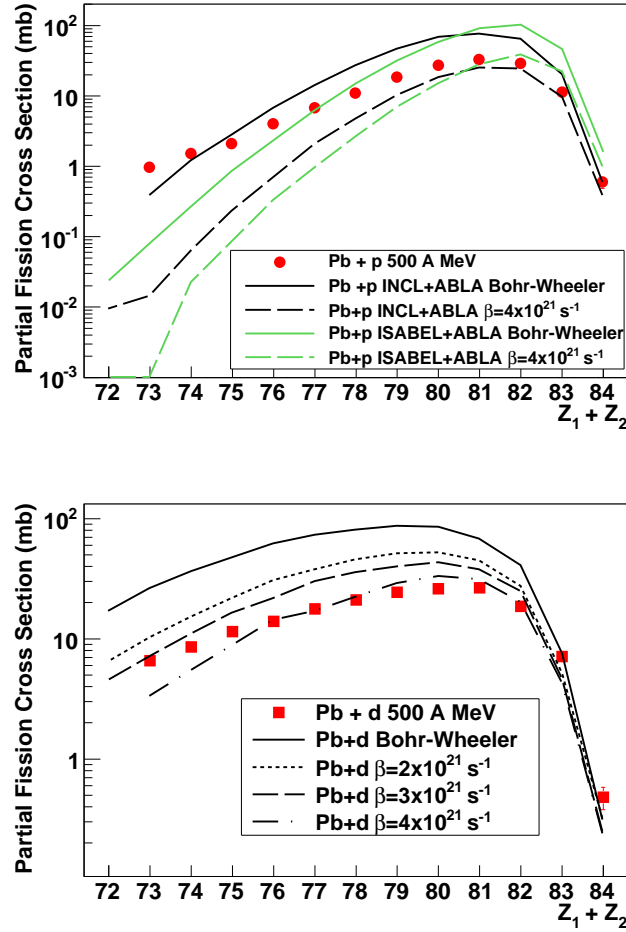


Figura 7: Panel superior: Sección eficaz parcial en función de $Z_1 + Z_2$ para la reacción $^{208}\text{Pb} + p$ a 500 A MeV en comparación con cálculos realizados con INCL+ABLA (negro) and ISABEL+ABLA (verde) con $\beta = 0$ (línea sólida) y $\beta = 4,0 \times 10^{21} \text{ s}^{-1}$ (línea a trazos), respectivamente. Panel inferior: Sección eficaz parcial en función de $Z_1 + Z_2$ para la reacción $^{208}\text{Pb} + d$ a 500 A MeV en comparación con cálculos realizados con INCL+ABLA para varios valores de β .

Sin embargo, la sección eficaz no es un buen observable para inferir efectos de tránsito en sistemas fisionantes. Para poder extraer alguna conclusión cuantitativa, comparamos σ_z en función de $Z_1 + Z_2$ con cálculos realizados con INCL+ABLA. Como se puede observar en la figura 8, los cálculos considerando $\beta = 0 \text{ s}^{-1}$ sobreestiman los valores experimentales de σ_z . Es necesario

introducir un valor de $\beta = 4,0 \times 10^{21} \text{ s}^{-1}$ en los cálculos que nos permite deducir que el tiempo de tránsito reduce σ_z , y por consiguiente, T_{sad} .

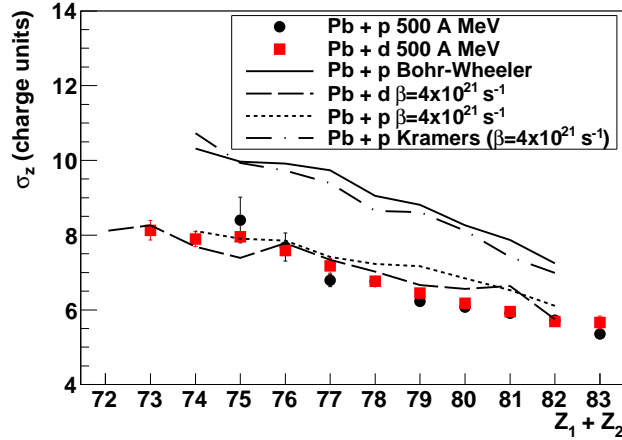


Figura 8: σ_z en función de $Z_1 + Z_2$ para las dos reacciones estudiadas en este trabajo en comparación con cálculos realizados con INCL+ABLA.

Futuros experimentos de fisión y necesidad de mejorar las medidas de tiempo de vuelo.

Los experimentos de fisión de próxima generación que utilizarán la técnica de cinemática inversa (SOFIA, R³B y FELISE), incluirán detectores modernos y punteros adecuados a los elevados requisitos necesarios para proveer medidas completas de alta precisión. Uno de los mayores retos lo constituye la identificación isotópica de ambos fragmentos de fisión simultáneamente. Hemos visto que es posible determinar con gran precisión el número atómico de los fragmentos de fisión con buena resolución, sin embargo, para separar isotópicamente los fragmentos de fisión, es necesario un muro de tiempo de vuelo con una alta resolución temporal. En este documento se describe el trabajo de investigación y desarrollo llevado a cabo para considerar la construcción de un muro de tiempo de vuelo basado en cámaras de placas resistivas (RPCs) para el experimento R³B. Estos detectores gaseosos funcionan aplicando un campo eléctrico intenso (100 kV/cm) entre dos electrodos resistivos de geometría planoparalela, de tal manera que una partícula que ioniza el gas contenido en el *gap* definido entre los dos electrodos, provoca una avalancha Townsend que induce una señal muy rápida en los electrodos.

La información acerca del funcionamiento de dichos detectores para la detección de iones pesados a energías relativistas es bastante escasa, y por lo tanto es necesaria una caracterización que pruebe su viabilidad para dicho propósito.

Para ello hemos construido varios prototipos de RPCs de diferentes tamaños junto a la electrónica desarrollada conjuntamente, con el propósito de caracterizarlos en diversos experimentos con iones pesados y electrones. Los resultados más concluyentes se obtuvieron con un prototipo (RPC-25) que consistía en dos módulos de RPC independientes con un tamaño de 15 cm \times 7 cm y con un solo *strip* o pista de cobre de 20 mm de anchura, contruídos con vidrio de 1 mm de espesor definiendo una estructura de doble *gap* de 300 μ m. Para las medidas, ambos módulos se metieron en el interior de una caja de aluminio estanca para preservar el flujo de gas. Además, obtuvimos resultados comparables con un prototipo (RPC-30) consistente en dos módulos independientes de 40 cm \times 20 cm de tamaño y con 5 *strips* de cobre de 20 cm de anchura. La mayor diferencia respecto al prototipo anterior es que cada módulo se ensambló únicamente pegando dos vidrios de 1 mm de espesor definiendo una estructura estanca de un solo *gap* de 300 μ m con la mínima cantidad posible de materia. En todas las medidas con estos prototipos hemos usado una mezcla gaseosa que contiene 90 % de C₂H₂F₄ y 10 % de SF₆,

El prototipo RPC-25 se testó con un haz que suministraba electrones en paquetes de alrededor de 10⁴ electrones, a una energía de 10 MeV y a diferentes intensidades, obteniendo valores excelentes de resolución temporal alcanzando valores de resolución temporal de alrededor de 35 ps para una intensidad del haz del 22 % y un voltaje del detector de 2800 V. La carga de la señal inducida en este caso era proporcional a la intensidad del haz. Este mismo prototipo se utilizó en un experimento donde fué irradiado con un haz de ²³⁸U a 1 A GeV de energía con una tasa de 5 Hz/cm² obteniendo un valor de la resolución temporal de 69 ps operando el detector con un voltaje de 2800 V. Por otra parte, el prototipo RPC-30 se caracterizó en un experimento para medir iones de ¹³⁶Xe a 560 A MeV de energía, con unas tasas de 3-10 Hz/cm² y 15-25 Hz/cm². A 2900 V de voltaje de operación y una tasa de irradiación de 3-10 Hz/cm², se obtuvo una resolución temporal de 46 ps y una eficiencia de detección cercana al 100 %. A tasas mayores la resolución temporal se degrada, obteniendo un valor de la resolución temporal de 56 ps para una tasa de 15-25 Hz/cm². Estos resultados se compilan en la figura 9, representando la resolución temporal en función de la carga de la señal inducida en los electrodos para poder comparar los datos obtenidos en todos los experimentos.

Teniendo en cuenta estos resultados podemos concluir que las RPCs pue-

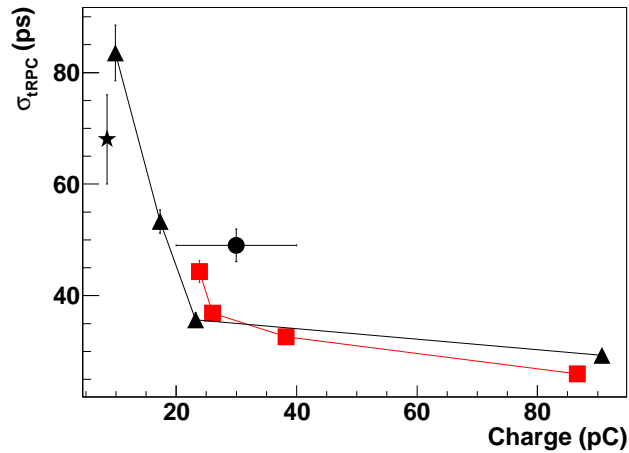


Figura 9: Resolución temporal en función de la carga. RPC-25 con paquetes de electrones (triángulos) y con ^{238}U (estrella), RPC-30 con ^{136}Xe (círculo).

den ser usadas para la detección y medida de tiempo de iones pesados relativistas cubriendo un rango amplio en número atómico, obteniendo resoluciones temporales por debajo de los 50 ps y eficiencias de detección cercanas al 100 % siempre teniendo en cuenta que la tasa de irradiación por unidad de superficie afecta drásticamente al funcionamiento del detector. Esto abre la posibilidad de construir un muro de tiempo de vuelo para el experimento de R^3B basados en RPCs teniendo en cuenta los requisitos más importantes de dicho detector.

En conclusión, en este trabajo se ha investigado el proceso de fisión a alta energía de excitación usando la técnica de cinemática inversa. En particular se han estudiado las reacciones $^{181}\text{Ta}+p$ a 300, 500, 800 y 1000 A MeV, y $^{208}\text{Pb}+p$ y $^{208}\text{Pb}+d$ a 500 MeV. Se han estudiado los efectos dinámicos en el proceso de fisión en estas reacciones con la ayuda de códigos punteros que describen este proceso en dos etapas: cascada intranuclear y evaporación. Se han validado estos códigos mediante comparación con los datos experimentales.

Por otra parte hemos demostrado la validez de las RPCs para la detección de iones pesados con energías relativistas, a través de un programa extenso de I+D donde hemos probados diversos prototipos en experimentos con diversos tipos de iones. Los resultados indican que bajo ciertas condiciones, estos detectores ofrecen excelentes resoluciones temporales por debajo de los 50 ps manteniendo una eficiencia de detección cercana al 100 %, lo que los convierte en sólidos candidatos para la construcción de un muro de tiempo de vuelo

para el futuro experimento de R^3B .

Appendix A

Calibration of the nuclear charge distributions

In this appendix we present the calibration of the nuclear charge spectra of both fission fragments obtained with the Twin MUSIC detector. The calibration was determined taking into account the value of the peaks in the charge of the fissioning nuclei distribution reconstructed from Z_1 and Z_2 (see Chap. 3). This calibration is also supported with the results obtained with calculations performed with INCL+ABLA. The height of the peaks corresponding to low energy fission events used for the calibration are properly reproduced. In addition, the calibration was compared to other works where the charge of the fissioning system of nuclei with similar fissility was also extracted [Hei03]. As can be seen in the lower panel of Fig. A.1, the distribution of Z_1+Z_2 of the reaction ^{214}Rn on plastic (CH_2) at 420A MeV is similar to the one obtained in this work for ^{208}Pb on proton and deuteron at 500A MeV. In the case of ^{214}Rn on Pb (upper panel) the electromagnetic-induced fission predominates as reflected by the high intensity of the $Z_1+Z_2=86$ peak.

However, the individual distributions of both fission fragments have to be calibrated carefully. Owing to the geometrical acceptance of the Twin MUSIC some fission events passing close to the cathode are not detected. Moreover, due to a possible misalignment of the the beam height both charge distributions are not symmetric. The condition stated before for fission events comprises the detection of both fission fragments in coincidence. A misalignment of the beam to the upper part of the chamber causes the heavier fission fragments emitted towards the lower part of the chamber to be stopped in the cathode. As consequence the lighter fragment entering the upper chamber is detected but the event is not accounted as fission. Therefore, the charge distribution of the fragments crossing the upper part of the chamber is different from the one of the fragments that are detected in the lower part

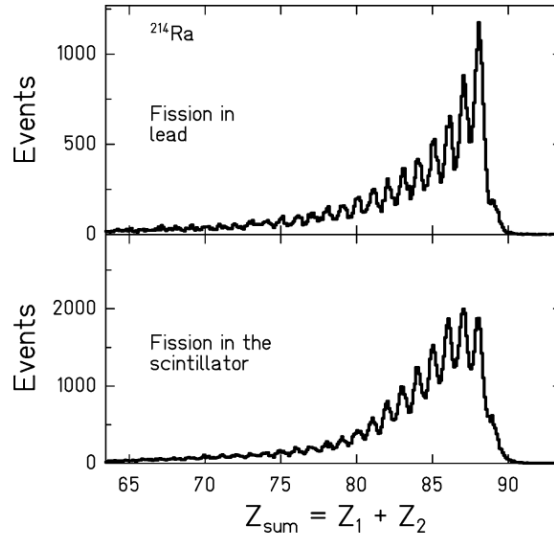


Figure A.1: Nuclear charge distribution of the fissioning nuclei in the reaction ^{214}Rn on CH_2 (lower panel) and Pb (upper panel). Figure taken from [Hei03].

(see left panel Fig. A.2). The mean value of the distribution registered in the upper part is shifted to higher values and conversely, the distribution of the lower part is shifted to lower values of the mean. Since the total charge distribution of the fission fragments is symmetric (Gaussian), the width of both distributions is reduced in the same way. A Gaussian fit was made to the experimental distributions yielding a value for the width of $\sigma_z = 6.5 \pm 0.4$ and a mean value of 40.43 and 39.32 for the upper and lower part of the Twin MUSIC, respectively.

A monte-carlo simulation based on Wilkins model [Wil76] was performed to correct the total and partial widths of the fission fragment charge distributions. The initial charge distributions were taken from INCL+ABLA taking into account a dissipation strength of $\beta = 4 \times 10^{21} \text{ s}^{-1}$. We determined the width and mean of the distributions of the fragments inside the chamber just considering different positions of the beam and different thicknesses of the cathode, as shown in the right panel of Fig. A.2. The value of the geometrical acceptance of the Twin MUSIC was determined by comparing the ratio Z_1/Z_2 of both simulated distributions with the ratio of the experimental ones. The parameters were taken to minimize the χ^2 value resulting from this comparison. A minimum value of $\chi = 7.62$ was obtained considering a displacement of the beam of +0.5 cm with respect to the Twin MUSIC cathode and a gap due to the cathode dead zone of ± 0.75 cm. Consequently,

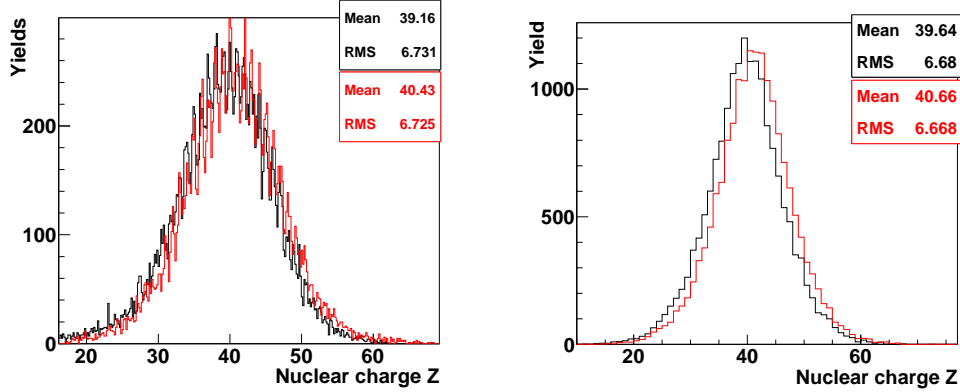


Figure A.2: Experimental (left panel) and simulated (right panel) fission fragment charge distributions for the reaction $^{208}\text{Pb}+p$ at 500A MeV.

each distribution is corrected giving a mean value of the nuclear charge of around 40 (39.97) and a standard deviation of $\sigma_z=6.7$ charge units. In the upper panel of Fig. A.3 the corrected distribution is shown while the correction factors for each nuclear charge are shown in the lower panel. The correction was applied using the same binning for both histograms.

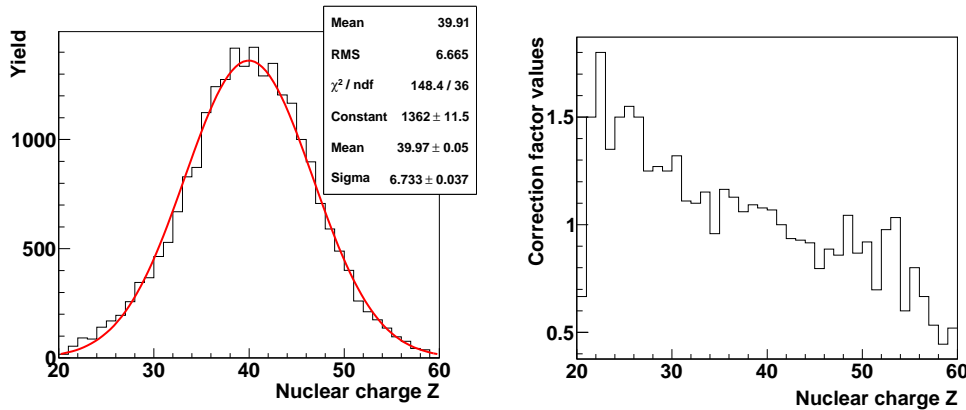


Figure A.3: Upper panel: Corrected fission fragments nuclear charge distribution. The thick solid line represents the Gaussian fit to the distribution. Lower panel: Value of the correction factors.

In addition, the experimental distributions concerning the partial width of the fission fragment distributions as a function of the charge of the fissioning nucleus were corrected also bin to bin using the Z_1/Z_2 ratio (see Fig. A.4).

This is a small correction that slightly increases the value of the width.

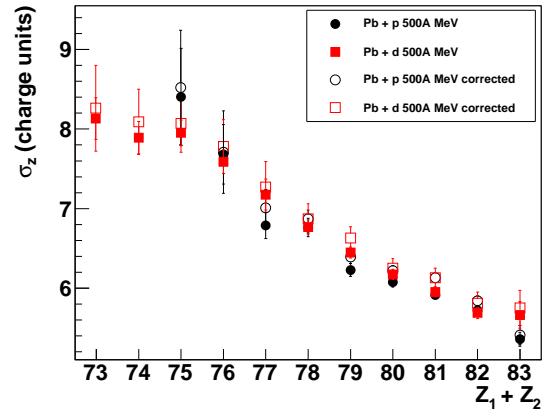


Figure A.4: Width of the fission fragment distribution as a function of the charge of the fissioning nuclei for the reactions $^{208}\text{Pb}+p$ (circles) and d (squares) at 500A MeV, before (solid symbols) and after (open symbols) the correction.

Bibliography

- [Abb98] M. Abbrescia *et al.*, *Beam test results on double-gap resistive plate chambers proposed for CMS experiment*, Nuclear Instruments and Methods in Physics Research Section A: Accelerators, Spectrometers, Detectors and Associated Equipment **414** (1998) 135 – 148, ISSN 0168-9002.
- [Abe94] S. Aberg and L.-O. Joensson, *Clustering aspects of nuclei with octupole and superdeformation*, Zeitschrift für Physik A Hadrons and Nuclei **349** (1994) 205–211.
- [Aie04] G. Aielli *et al.*, *Test and performances of the RPC trigger chambers of the ATLAS experiment at LHC*, Nuclear Instruments and Methods in Physics Research Section A: Accelerators, Spectrometers, Detectors and Associated Equipment **533** (2004) 193 – 198, ISSN 0168-9002.
- [Aki09] A. Akindinov *et al.*, *Final test of the MRPC production for the ALICE TOF detector*, Nuclear Instruments and Methods in Physics Research Section A: Accelerators, Spectrometers, Detectors and Associated Equipment **602** (2009) 709 – 712, ISSN 0168-9002.
- [Amm07] V. Ammosov *et al.*, *The HARP resistive plate chambers: Characteristics and physics performance*, Nuclear Instruments and Methods in Physics Research Section A: Accelerators, Spectrometers, Detectors and Associated Equipment **578** (2007) 119 – 138.
- [Amm10] V. Ammosov *et al.*, *Time resolution of a 6-gap resistive plate chamber with strip readout*, Instruments and Experimental Techniques **53** (2010) 175–179, 10.1134/S0020441210020041.
- [And10] A. N. Andreyev *et al.*, *New Type of Asymmetric Fission in Proton-Rich Nuclei*, Phys. Rev. Lett. **105** (2010) 252502.

- [AP06] H. Alvarez-Pol *et al.*, *Conceptual design of a large area time-of-flight wall for the R3B experiment at FAIR*, Nuclear Physics B - Proceedings Supplements **158** (2006) 186 – 189.
- [Arm70] P. Armbruster, *On the calculation of charge values of fission fragments*, Nuclear Physics A **140** (1970) 385 – 399.
- [Ayy12] Y. Ayyad *et al.*, *First results with RPC prototypes for the detection of relativistic heavy-ions at the R3B experiment*, Nuclear Instruments and Methods in Physics Research Section A: Accelerators, Spectrometers, Detectors and Associated Equipment **661**, **Supplement 1** (2012) S141 – S144.
- [Bac00] C. Bacci *et al.*, *Results from the analysis of data collected with a 50m² RPC carpet at YangBaJing*, Nuclear Instruments and Methods in Physics Research Section A: Accelerators, Spectrometers, Detectors and Associated Equipment **456** (2000) 121 – 125.
- [Bai10] A. Bail, *Workshop on Large-Area-Picosecond-Photodetectors electronics for particle physics and medical imaging, LPC, France* (2010).
- [Bar62] V. I. Baranovskiy, A. N. Murin and B. K. Preobrazhenskiy, *Radiokhimiya* **4** (1962) 470.
- [Ben98] J. Benlliure *et al.*, *Calculated nuclide production yields in relativistic collisions of fissile nuclei*, Nuclear Physics A **628** (1998) 458 – 478.
- [Ben01] J. Benlliure *et al.*, *Isotopic production cross sections of fission residues in 197Au-on-proton collisions at 800 A MeV*, Nuclear Physics A **683** (2001) 513 – 539, ISSN 0375-9474.
- [Ben02] J. Benlliure *et al.*, *Signatures of fission dynamics in highly excited nuclei produced in 197Au (800A MeV) on proton collisions*, Nuclear Physics A **700** (2002) 469 – 491.
- [Ber84] J. Berger, M. Girod and D. Gogny, *Microscopic analysis of collective dynamics in low energy fission*, Nuclear Physics A **428** (1984) 23 – 36.
- [Ber03] M. Bernas *et al.*, *Fission-residues produced in the spallation reaction 238U + p at 1 A GeV*, Nuclear Physics A **725** (2003) 213 – 253.

- [Bha86] K. H. Bhatt, P. Grangé and B. Hiller, *Nuclear friction and lifetime of induced fission*, Phys. Rev. C **33** (1986) 954–968.
- [Bla92] T. Blaich *et al.*, *A large area detector for high-energy neutrons*, Nuclear Instruments and Methods in Physics Research Section A: Accelerators, Spectrometers, Detectors and Associated Equipment **314** (1992) 136 – 154.
- [Bla09] A. Blanco *et al.*, *In-beam measurements of the HADES-TOF RPC wall*, Nuclear Instruments and Methods in Physics Research Section A: Accelerators, Spectrometers, Detectors and Associated Equipment **602** (2009) 691 – 695.
- [Blo78] J. Blocki *et al.*, *One-body dissipation and the super-viscosity of nuclei*, Annals of Physics **113** (1978) 330 – 386.
- [Boc78] B. A. Bochagov *et al.*, Sov. J. Nucl. Phys. **28** (1978) 291.
- [Boh36] N. Bohr, *Neutron Capture and Nuclear Constitution*, Nature (1936) 344–348.
- [Boh39] N. Bohr and J. A. Wheeler, *The Mechanism of Nuclear Fission*, Phys. Rev. **56** (1939) 426–450.
- [Bor28] M. Born and V. Fock, *Beweis des adiabatenatzes*, Zeitschrift für Physik A Hadrons and Nuclei **51** (1928) 165–180.
- [Bou02] A. Boudard *et al.*, *Intranuclear cascade model for a comprehensive description of spallation reaction data*, Phys. Rev. C **66** (2002) 044615.
- [Bro90] U. Brosa, S. Grossmann and A. Müller, *Nuclear scission*, Physics Reports **197** (1990) 167 – 262.
- [Bur96] R. Burman and L. Daemen, Nucl. Instr. and Meth. Phys. Res. A **370** (1996) 335–340.
- [Bus05] M. Bussa, *The PANDA experiment at FAIR*, Czechoslovak Journal of Physics **55** (2005) A279–A288.
- [Cab09] P. Cabanelas *et al.*, *Performances of 4-gap timing RPCs for relativistic ions in the range $Z = 16$* , Journal of Instrumentation **4** (2009) P11007.

- [Car88] R. Cardarelli *et al.*, *Progress in resistive plate counters*, Nuclear Instruments and Methods in Physics Research Section A: Accelerators, Spectrometers, Detectors and Associated Equipment **263** (1988) 20 – 25.
- [Cas12a] E. Casarejos *et al.*, *Design of iToF: A ToF-wall detector to identify relativistic ions in R3B-FAIR*, Nuclear Instruments and Methods in Physics Research Section A: Accelerators, Spectrometers, Detectors and Associated Equipment **661, Supplement 1** (2012) S137 – S140.
- [Cas12b] E. Casarejos *et al.*, *Detection efficiency of relativistic heavy-ions with resistive-plate chambers*, Nuclear Instruments and Methods in Physics Research Section A: Accelerators, Spectrometers, Detectors and Associated Equipment **674** (2012) 39 – 45.
- [Cha88] R. Charity *et al.*, *Systematics of complex fragment emission in niobium-induced reactions*, Nuclear Physics A **483** (1988) 371 – 405.
- [Cha01] G. Chaudhuri and S. Pal, *Fission widths of hot nuclei from Langevin dynamics*, Phys. Rev. C **63** (2001) 064603.
- [Cla03] K. N. Clausen, ESS, The European Spallation Source, ICANS XVI, 16th Meeting of the International Collaboration on Advanced Neutron Sources Düsseldorf Neuss, Germany. (2003).
- [Cug97] J. Cugnon, C. Volant and S. Vuillier, *Improved intranuclear cascade model for nucleon-nucleus interactions*, Nuclear Physics A **620** (1997) 475 – 509.
- [Dus01] S. Dusini *et al.*, *Design and prototype tests of the RPC system for the OPERA spectrometers* (2001) 117 – 120.
- [Enq01] *Isotopic yields and kinetic energies of primary residues in 1 A GeV 208Pb+p reactions*, Nuclear Physics A **686** (2001) 481 – 524.
- [Enq02] T. Enqvist *et al.*, *Primary-residue production cross sections and kinetic energies in 1AGeV 208Pb on deuteron reactions*, Nuclear Physics A **703** (2002) 435 – 465.
- [FAI] *FAIR web page*, <http://www.gsi.de/fair/>.

- [Fer05] B. Fernández *et al.*, *Nuclide cross-sections of fission fragments in the reaction $208\text{Pb} + p$ at 500 A MeV*, Nuclear Physics A (2005) 227 – 267.
- [Fon69] P. Fong, *Statistical Theory of Nuclear Fission*, Cordon and Breach, New York (1969).
- [Fon99] P. Fonte *et al.*, *A spark-protected high-rate detector*, Nuclear Instruments and Methods in Physics Research Section A: Accelerators, Spectrometers, Detectors and Associated Equipment **431** (1999) 154 – 159.
- [Fon00] P. Fonte, A. Smirnitski and M. Williams, *A new high-resolution TOF technology*, Nuclear Instruments and Methods in Physics Research Section A: Accelerators, Spectrometers, Detectors and Associated Equipment **443** (2000) 201 – 204.
- [Fon02] P. Fonte, *Applications and new developments in resistive plate chambers*, Nuclear Science, IEEE Transactions on **49** (2002) 881 – 887.
- [Frö98] P. Fröbrich and I. Gontchar, *Langevin description of fusion, deep-inelastic collisions and heavy-ion-induced fission*, Physics Reports **292** (1998) 131 – 237, ISSN 0370-1573, doi:10.1016/S0370-1573(97)00042-2.
- [Fuk90] T. Fukahori and S. Pearlstein, *Proceedings of the Advisory Group Meeting Organized by IAEA, Vienna, October (1990)* 9–12.
- [Gai91] J. J. Gaimard and K. H. Schmidt, *A reexamination of the abrasion-ablation model for the description of the nuclear fragmentation reaction*, Nuclear Physics A **531** (1991) 709 – 745.
- [Gav81] A. Gavron *et al.*, *Time Scale of Fission at High Angular Momentum*, Phys. Rev. Lett. **47** (1981) 1255–1258.
- [Gav82] A. Gavron *et al.*, *Time Scale of Fission at High Angular Momentum*, Phys. Rev. Lett. **48** (1982) 835–836.
- [Gei92] H. Geissel *et al.*, *The GSI projectile fragment separator (FRS): a versatile magnetic system for relativistic heavy ions*, Nuclear Instruments and Methods in Physics Research Section B: Beam Interactions with Materials and Atoms **70** (1992) 286 – 297.

- [Gei03] H. Geissel *et al.*, *The Super-FRS project at GSI*, Nuclear Instruments and Methods in Physics Research Section B: Beam Interactions with Materials and Atoms **204** (2003) 71 – 85, 14th International Conference on Electromagnetic Isotope Separators and Techniques Related to their Applications.
- [Gol99] F. Goldenbaum *et al.*, *Fission Time Evolution with Excitation Energy from a Crystal Blocking Experiment*, Phys. Rev. Lett. **82** (1999) 5012–5015.
- [Gou05] H. Goutte *et al.*, *Microscopic approach of fission dynamics applied to fragment kinetic energy and mass distributions in ^{238}U* , Phys. Rev. C **71** (2005) 024316.
- [Gra83] P. Grangé, L. Jun-Qing and H. A. Weidenmüller, *Induced nuclear fission viewed as a diffusion process: Transients*, Phys. Rev. C **27** (1983) 2063–2077.
- [Gro75] D. Gross, *Theory of nuclear friction*, Nuclear Physics A **240** (1975) 472 – 484.
- [Hah39] O. Hahn and F. Strassmann, *Über den Nachweis und das Verhalten der bei der Bestrahlung des Urans mittels Neutronen entstehenden Erdalkalimetalle*, Naturwissenschaften **27** (1939) 89.
- [Hau52] W. Hauser and H. Feshbach, *The Inelastic Scattering of Neutrons*, Phys. Rev. **87** (1952) 366–373.
- [Hei03] A. Heinz *et al.*, *Electromagnetic-induced fission of ^{238}U projectile fragments, a test case for the production of spherical super-heavy nuclei*, Nuclear Physics A **713** (2003) 3 – 23, ISSN 0375-9474.
- [Hil92] D. Hilscher and H. Rossner, *Dynamics of nuclear fission*, Ann. Phys. Fr. **17** (1992) 471.
- [Hin92] D. J. Hinde *et al.*, *Neutron emission as a probe of fusion-fission and quasifission dynamics*, Phys. Rev. C **45** (1992) 1229–1259.
- [Hof97] H. Hofmann, *A quantal transport theory for nuclear collective motion: The merits of a locally harmonic approximation*, Physics Reports **284** (1997) 137 – 380.
- [Hof01] H. Hofmann *et al.*, *Nuclear fission: The “onset of dissipation” from a microscopic point of view*, Phys. Rev. C **64** (2001) 054316.

- [Ign75] A. V. Ignatyuk *et al.*, Sov. J. Nucl. Phys. **21** (1975) 612.
- [ISO] *ISOLDE web page*, <http://isolde.web.cern.ch/isolde/>.
- [Jac09] D. Jacquet and M. Morjean, *Fission times of excited nuclei: An experimental overview*, Progress in Particle and Nuclear Physics **63** (2009) 155 – 185.
- [Jon97] M. de Jong, A. Ignatyuk and K.-H. Schmidt, *Angular momentum in peripheral fragmentation reactions*, Nuclear Physics A **613** (1997) 435 – 444.
- [Jur02] B. Jurado, *New signatures on dissipation at small deformations from studies of fission induced by peripheral heavy-ion collisions at relativistic energies*, Ph.D. thesis, Universidad de Santiago de Compostela (2002).
- [Jur03] B. Jurado, K.-H. Schmidt and J. Benlliure, *Time evolution of the fission-decay width under the influence of dissipation*, Physics Letters B **553** (2003) 186 – 190.
- [Jur04] B. Jurado *et al.*, *Transient Effects in Fission from New Experimental Signatures*, Phys. Rev. Lett. **93** (2004) 072501.
- [Jur05a] B. Jurado *et al.*, *Conditions for the manifestation of transient effects in fission*, Nuclear Physics A **757** (2005) 329 – 348.
- [Jur05b] B. Jurado *et al.*, *A critical analysis of the modelling of dissipation in fission*, Nuclear Physics A **747** (2005) 14 – 43.
- [Kar75] P. J. Karol, *Nucleus-nucleus reaction cross sections at high energies: Soft-spheres model*, Phys. Rev. C **11** (1975) 1203–1209.
- [Kel04] A. Kelić *et al.*, *Isotopic and velocity distributions of $_{83}\text{Bi}$ produced in charge-pickup reactions of ^{208}Pb at 1A GeV*, Phys. Rev. C **70** (2004) 064608, doi:10.1103/PhysRevC.70.064608.
- [Kel09] A. Kelić, M. V. Ricciardi and K.-H. Schmidt, ArXiv:0906.4193.v1. (2009).
- [Kiš11] M. Kiš *et al.*, *A Multi-strip Multi-gap RPC Barrel for Time-of-Flight Measurements*, Nuclear Instruments and Methods in Physics Research Section A: Accelerators, Spectrometers, Detectors and Associated Equipment **646** (2011) 27 – 34.

- [Koc05] K. Koch *et al.*, *A new TAC-based multichannel front-end electronics for TOF experiments with very high time resolution*, Nuclear Science, IEEE Transactions on **52** (2005) 745 – 747.
- [Kon66] V. A. Konshin, *Sov. J. Nucl. Phys.* **2** (1966) 489.
- [Kra40] H. A. Kramers, *Physika VII* (1940) 284.
- [Kra04] A. Krasznahorkay *et al.*, *Neutron-skin thickness in neutron-rich isotopes*, Nuclear Physics A **731** (2004) 224 – 234.
- [LAN] *LAND web page*, http://www.gsi.de/forschung/kp/kp2/collaborations/land/index_e.html.
- [Lip03] C. Lippmann, *Detector Physics of Resistive Plate Chambers*, Ph.D. thesis, European Organization for Nuclear Research (CERN) (2003).
- [Lou11] D. P. Loureiro *et al.*, *Production of neutron-rich nuclei in fragmentation reactions of projectiles at relativistic energies*, Physics Letters B **703** (2011) 552 – 556.
- [M2J] *M2J Company, France, MATAQ32 chip based VME boards.*
- [Man10] D. Mancusi, R. J. Charity and J. Cugnon, *Unified description of fission in fusion and spallation reactions*, Phys. Rev. C **82** (2010) 044610.
- [Mau65] M. Maurette and C. Stephan, *Proc. Int. Conf. Physics and Chemistry of Fission, Salzburg, Austria, March 22-26 (1965)*.
- [MBS] *MBS web page*; <http://www-win.gsi.de/daq/>.
- [Möl86] P. Möller, *Macroscopic model of rotating nuclei*, At. Nucl. Data Tables **59** (1986) 185.
- [Mol93] J. D. Molitoris *et al.*, *Molecular-orbital study of late-fission times in deep-inelastic $^{238}\text{U}+^{238}\text{U}$ collisions*, Phys. Rev. Lett. **70** (1993) 537–540.
- [Möl01] P. Möller *et al.*, *Nuclear fission modes and fragment mass asymmetries in a five-dimensional deformation space*, Nature **409** (2001) 785.
- [Mor75] L. G. Moretto, *Statistical emission of large fragments: A general theoretical approach*, Nuclear Physics A **247** (1975) 211 – 230.

- [Mor95] L. G. Moretto *et al.*, Phys. Rev. Lett. **75** (1995) 4186.
- [Nif01] H. Nifenecker *et al.*, Nucl. Instr. and Meth. A **463** (2001) 428.
- [Nis03] S. Nishimura *et al.*, *Systematic studies of scintillation detector with timing resolution of 10 ps for heavy ion beam*, Nuclear Instruments and Methods in Physics Research Section A: Accelerators, Spectrometers, Detectors and Associated Equipment **510** (2003) 377 – 388.
- [Nör83] W. Nörenberg, *Dissipative diabatic dynamics: A shell-model approach to large-amplitude collective nuclear motion*, Nuclear Physics A **409** (1983) 191 – 211.
- [Pí0] D. Pérez, *Investigating the production of medium-mass neutron-rich nuclei*, Ph.D. thesis, Universidad de Santiago de Compostela (2010).
- [Par] C. Paradela *et al.*, *In preparation* .
- [Pau94] P. Paul and M. Thoennessen, Phys. Rev. C **44** (1994) 65.
- [Per07] J. Pereira *et al.*, *Isotopic production cross sections and recoil velocities of spallation-fission fragments in the reaction $^{238}\text{U}(1\text{A GeV}) + d$* , Physical Review C (Nuclear Physics) **75** (2007) 014602.
- [Pfü94] M. Pfützner *et al.*, *Energy deposition by relativistic heavy ions in thin argon absorbers*, Nuclear Instruments and Methods in Physics Research Section B: Beam Interactions with Materials and Atoms **86** (1994) 213 – 218.
- [Pro01] A. V. Prokofiev, Nucl. Instr. and Meth. Phys. A **463** (2001) 557.
- [R3B] *R3B web page*, [http://http://www.gsi.de/R3B](http://www.gsi.de/R3B).
- [Rau] T. Rauscher *et al.*, *Production of heavy elements in inhomogeneous cosmologies*, The Astrophysical Journal .
- [Ris89] H. Risken, *The Fokker-Planck Equation*, Springer, Berlin (1989).
- [Rus97] A. Y. Rusanov, M. G. Itkis and V. N. Okolovic, Phys. At. Nucl. **60** (1997) 683.
- [San81] R. Santonico and R. Cardarelli, *Development of resistive plate counters*, Nuclear Instruments and Methods in Physics Research **187** (1981) 377 – 380.

- [Sax94] A. Saxena *et al.*, *Entrance channel effects in the fusion-fission time scales from studies of prescission neutron multiplicities*, Phys. Rev. C **49** (1994) 932–940.
- [Sch00] K.-H. Schmidt *et al.*, *Relativistic radioactive beams: A new access to nuclear-fission studies*, Nuclear Physics A **665** (2000) 221 – 267, ISSN 0375-9474.
- [Sch04] A. Schüttauf, *Timing RPCs in FOPI*, Nuclear Instruments and Methods in Physics Research Section A: Accelerators, Spectrometers, Detectors and Associated Equipment **533** (2004) 65–68.
- [Sch10] C. Schmitt *et al.*, *Fragmentation of spherical radioactive heavy nuclei as a novel probe of transient effects in fission*, Phys. Rev. C **81** (2010) 064602.
- [Ser47] R. Serber, *Nuclear Reactions at High Energies*, Phys. Rev. **72** (1947) 1114–1115.
- [Shi73] O. E. Shigaev *et al.*, Rept. Khlopin Radiev. Inst., Leningrad Reports **17** (1973).
- [Sie86] A. J. Sierk, *Macroscopic model of rotating nuclei*, Phys. Rev. C **33** (1986) 2039–2053.
- [Ste67] C. Stephan and M. L. Perlman, Phys. Rev. **164** (1967) 1528.
- [Ste91] H. Stelzer, *Multiwire chambers with a two-stage gas amplification*, Nuclear Instruments and Methods in Physics Research Section A: Accelerators, Spectrometers, Detectors and Associated Equipment **310** (1991) 103 – 106.
- [Str67] V. Strutinsky, *Shell effects in nuclear masses and deformation energies*, Nuclear Physics A **95** (1967) 420 – 442.
- [Tar11] D. Tarrío *et al.*, *Neutron-induced fission cross section of ^{nat}Pb and ^{209}Bi from threshold to 1 GeV: An improved parametrization*, Phys. Rev. C **83** (2011) 044620.
- [Tho93] M. Thoennessen and G. F. Berstch, Phys. Rev. Lett. **71** (1993) 4303.
- [Vai10] L. A. Vaishnene *et al.*, *Isotopic effect in the energy dependence of the total fission cross section of lead and ^{209}Bi nuclei for protons with energies up to 1 GeV*, Bulletin of the Russian Academy of Sciences: Physics **74** (2010) 496–499.

- [Wan10] Y. Wang *et al.*, *Production and quality control of STAR-TOF MRPC*, Nuclear Instruments and Methods in Physics Research Section A: Accelerators, Spectrometers, Detectors and Associated Equipment **613** (2010) 200 – 206.
- [Wei37] V. Weisskopf, *Statistics and Nuclear Reactions*, Phys. Rev. **52** (1937) 295–303.
- [Wei40] V. F. Weisskopf and D. H. Ewing, *On the Yield of Nuclear Reactions with Heavy Elements*, Phys. Rev. **57** (1940) 472–485.
- [Wei80] H. A. Weidenmüller, Prog. Part. Nucl. Phys. **3** (1980) 49.
- [Wil76] B. D. Wilkins, E. P. Steinberg and R. R. Chasman, *Scission-point model of nuclear fission based on deformed-shell effects*, Phys. Rev. C **14** (1976) 1832–1863.
- [Wil04] H. Wilschut and V. Kravchuk, *Developing an atomic clock for fission lifetime measurements*, Nuclear Physics A **734** (2004) 156 – 163.
- [Yar79] Y. Yariv and Z. Fraenkel, *Intranuclear cascade calculation of high-energy heavy-ion interactions*, Phys. Rev. C **20** (1979) 2227–2243.
- [Ye12] W. Ye, *Spallation reactions induced by high energy protons: A possible way to probe dissipation in nuclear fission with excitation energy at scission*, Phys. Rev. C **85** (2012) 011601.
- [Yur05] V. I. Yurevich *et al.*, Jour. Fiz. Elementarnykh Chastich i Atomn. Yadra, Letters **2** (2005) 49.
- [Zal00] A. Zallo, *The BaBar RPC system*, Nuclear Instruments and Methods in Physics Research Section A: Accelerators, Spectrometers, Detectors and Associated Equipment **456** (2000) 117 – 120.
- [Zeb96] E. C. Zeballos *et al.*, *A new type of resistive plate chamber: The multigap RPC*, Nuclear Instruments and Methods in Physics Research Section A: Accelerators, Spectrometers, Detectors and Associated Equipment **374** (1996) 132 – 135.